MONTE-CARLO SIMULATIONS OF THE BACKGROUND NOISE IN GAMMA-RAY SATELLITES

By
Charlotte Lucy Perfect
B.Sc.(Hons) M.Sc.

A thesis submitted for the degree of
Doctor of Philosophy

Department of Electronics and Computer Science,
University of Southampton,
United Kingdom.

July 2002

UNIVERSITY OF SOUTHAMPTON

ABSTRACT

FACULTY OF ENGINEERING

ELECTRONICS AND COMPUTER SCIENCE DEPARTMENT

Doctor of Philosophy

Monte-Carlo simulations of the background noise in gamma-ray satellites

by Charlotte Lucy Perfect

Monte Carlo simulations are used in γ-ray astronomy to estimate the effects of the space radiation environment to which the detectors onboard satellites are exposed. A study of a sample of Classical Novae using the BATSE (Burst and Transient Source Experiment) Earth Occultation Technique shows the sensitivity to be degraded by systematic effects. By modelling the instrument background, however, the sensitivity could be improved significantly. Simulations of the background noise in the LEGRI detectors are able to predict the observed effects of geomagnetic cut-off on the cosmic ray and atmospheric background components. The background spectra are dominated by fluorescence from the tantalum collimator. The effects of a passage through the South Atlantic Anomaly are modelled and compared to observations. Activation of spacecraft components causes a decay of the background count rate with time. The main contributions to the induced background noise are shown to be the collimator, cadmium telluride and shielding. No single isotope explains the observed decay time of the background. Similar methods have been used to model the effect of a solar flare on the instruments onboard the INTEGRAL satellite. The count rates in the detectors are found to increase significantly for periods of up to 96 hours after the flare. Many line features can be seen in the spectra and these are found to be mainly due to electron capture processes within the detectors.

Contents

List of Figures

List of Tables

Acknowledgements

I am greatly indebted to my supervisors Professor Tony Dean and Dr Jeff Reeve who have provided much advice and encouragement throughout.

Many thanks to Dr Tony Bird (aka Ralph) for guidance in the art of doing a PhD, for putting up with the bombardment of questions thrown his way and for not injuring me too greatly with the paper bombs thrown my way! In particular I would like to thank Ralph for his help and support with the LEGRI work.

I would also like to thank Dr Colin Ferguson for advice on TIMM and the solar flare modelling, Dr Jon Lockley for guidance both with Cataclysmic Variable stars and the delights of Linux and Matthew Westmore for help with BATSE.

This thesis would also not have been possible without the help of all of the members of the Astronomy group at Southampton who have provided much support and amusement throughout. In particular I would like to thank (in no order) Rachel, James, Chris, Nick H, Matt, Jeno, Dave and Simon. Members from the ECS group, in particular Ben and Duan, also deserve a mention for providing much needed entertainment during the writing up phase.

Last but by no means least I would like to thank Mum, Dad, Russell and Melanie for supporting, understanding and showing interest throughout my studies. My thanks also go to Harriet (born May 2000) for providing much fun in the final stages of this thesis. I look forward to teaching you more Astronomy in the years to come!

Chapter 1

Introduction

Over the past 40 years γ-ray astronomy has unveiled intricate details on some of the universe's most mysterious objects and phenomena including black hole systems, supernovae and γ-ray bursts. The highly penetrative nature of γ-rays enables astronomers to probe deep into sources that may not even be visible at other wavelengths. Gamma-rays act as a signature through which nuclear reactions and other high energy processes can be identified.

Since γ-rays cannot penetrate the earth's atmosphere, however, the detectors used in this field are often onboard satellites. Unfortunately at such altitudes the detectors are exposed to radiation other than that from the sources they are observing. This background radiation may increase the count rate in the detectors and consequently provide misleading information on the sources being observed. A variety of detector system designs including the use of shielding and collimation may help to eliminate some of this background noise but the removal of its entirety is virtually impossible. Modelling the background noise has therefore become an invaluable tool to enable a more accurate analysis of the astronomical data.

The use of Monte Carlo simulations to model the background noise in γ-ray satellites is the basis for this thesis. Chapters 2 to 4 provide a review of γ-ray astronomy, detector system techniques and the background noise experienced by γ-ray satellites.

Chapter 5 uses earth occultation data from BATSE (Burst and Transient Source Experiment) to search for evidence of hard x-ray emission from the outbursts of classical novae. The sample chosen consists of all novae, both fast and slow, from the "Catalogue and Atlas of Cataclysmic Variables - 2nd edition" [15]. The data analysis concentrates mainly on the time before the visual outburst since this is when hard x-ray/γ-ray emission is most likely to occur. BATSE data is also used to search for hard x-ray emission from the nova remnant as well as from other types of cataclysmic variable stars including Polars and Intermediate Polars. The BATSE background model is currently being developed at Southampton University and it

is intended that the work here demonstrates why an improvement in instrument sensitivity through subtraction of the background model (called flat fielding) could be needed.

Chapters 6 and 7 are based on Monte-Carlo simulations of the background noise in LEGRI (Low Energy Gamma Ray Imager) onboard the Minisat-01 satellite. In Chapter 6 an orbit history for the spacecraft is used to select an interval of data including both a pass through the South Atlantic Anomaly (SAA) and the extremes of latitude but excluding periods of source observation time. This data is deconvolved into background count rate profiles versus latitude to show the effects of geomagnetic cutoff. An equivalent orbit is then simulated using Monte-Carlo techniques and the resulting count rates compared to those observed. Analysis of the simulated spectra can then be used to indicate the constituents and shape of the actual spectra. The effects of geomagnetic cutoff on each type of background noise are illustrated and spectral peaks identified.

Chapter 7 uses a similar approach to investigate the effects of a passage through the SAA on LEGRI. Observed data illustrates how single and consecutive passages affect the count rates in the detectors. A variable flux model is used to simulate the SAA passage, the count rates are compared to those observed and new spectral peaks are identified in the raw simulated spectra. A "blurring" algorithm is applied to the raw spectra to simulate the energy resolution of the detectors and the effects of charge trapping. The "blurred" spectra are then compared to observed spectra. Further analysis of the simulated raw spectra reveals which components of the detector system become activated and how much each contributes to the increase in background noise.

The INTEGRAL (INTErnational Gamma-Ray Astrophysics Laboratory) satellite is due to be launched in 2002 at a time of high solar activity and is therefore likely to experience periods of extreme radiation due to solar flares. Chapter 8 uses Monte-Carlo simulations to investigate the effects of a solar flare on the instruments onboard INTEGRAL. The solar flare of March 1991 is chosen as a basis for the study because its flux intensity and duration have been well documented. The event is first simulated using a constant flux model which spreads the radiation emitted by the flare evenly over a period of 5 days. Subsequently the variable flux model takes a more sophisticated approach and varies the flux according to time intensity profiles taken from Ulysses data. The resulting spectra and decay profiles for each model are then analysed to demonstrate how a solar flare of this size and magnitude could affect the instruments onboard INTEGRAL.

Chapter 2

Gamma-ray astronomy

2.1 Introduction

Since γ-rays cannot penetrate the earth's atmosphere they would have been difficult to detect until the 1960s when rockets became sophisticated enough to carry detectors and their payloads. Before this time γ-ray detection from extraterrestrial sources was restricted mainly to balloon-borne experiments such as those conducted by Dean et al [13]. The first significant observations came from the OSO-3 satellite when an all sky survey revealed γ-ray emission of energies exceeding 50 MeV from the galactic disk with a broad peak around the galactic centre [36]. Since then γ-ray satellites have provided an ever deeper understanding of a variety of astronomical sources including binary star systems, γ-ray bursts, supernovae and active galactic nuclei.

Gamma-ray astronomy encompasses a broad range of energies, the lower limit of which may in fact be classed as hard x-rays. Each of the detectors discussed in this thesis have different energy ranges but all operate in the γ-ray region (ie above several keV). It is useful therefore to describe the mechanisms by which astronomical sources emit γ-rays before turning to a discussion of the sources themselves.

2.2 Emission Mechanisms

The following is a brief summary of the emission mechanisms through which γ-rays are produced.

- Thermal radiation. Thermal Bremsstrahlung arises through interactions of electrons with an ionised gas whose temperature exceeds $\sim 10^6$K. Since the electrons are free both before and after interaction this type of radiation is sometimes called *free-free* emission. Black Body radiation, the second type of Thermal radiation, arises through emissions from a Black Body but for this to occur the object has to be up to 10^9K hot. In both cases the resulting spectrum is a continuous exponential.

- Inverse Compton Scattering. Low energy photons are scattered up to higher energies by relativistic electrons. The Compton interaction ultimately leads to photons gaining energy and electrons losing energy hence the name *Inverse* Compton scattering. If the electron distribution is a power law then a power-law photon spectrum results.
- Bremsstrahlung Radiation. The rapid deceleration of electrons in the vicinity of an atom or ion leads to Bremsstrahlung ("Braking") radiation. The resulting spectrum is continuous with spectral shape $\sim 1/E_\gamma$.
- Synchrotron Emission. High energy electrons in a magnetic field lose energy by synchrotron emission. If the initial distribution of electrons is a power law then the resulting emission will also be in the form of a power law.

2.3 High/Low Mass X-ray Binary Stars

X-ray binary stars are the most common type of strong x/γ-ray sources. The compact source is either a neutron star or a black hole which is accreting material from the companion. Binary star systems containing a white dwarf are called Cataclysmic Variables and are discussed separately in the section below and in Chapter 5.

If the orbital period and distance between the two stars is known Keplers Third Law can be used to calculate the sum of the masses. The mass of the companion is inferred from its luminosity and thus the mass of the compact source can be estimated.

Many factors affect where the strongest source of x-rays are found in a binary star system. If the compact source is a black hole an accretion disk develops and this becomes the dominant source of x-rays. Where the compact source is a neutron star the magnetic field may disrupt the accretion flow so that matter is funneled directly onto the poles of the neutron star. If the magnetic field of the neutron star is weak the accreting matter takes the form of an accretion disk as in the black hole situation. If the magnetic field is weaker still then the accretion disk may come into contact with the neutron star creating a boundary layer which dominates the x-ray emission. This picture is further complicated by wind accretion. In some binary star systems the matter has less angular momentum and is accreted through stellar wind rather than by an accretion disk.

X-ray binary stars can be split into High and Low mass x-ray binaries according to the mass of the *companion* to the compact object. HMXBs (High Mass X-Ray Binaries) contain early type giant or supergiant stars and have orbital periods of a few days to several hundreds of days. The x-ray sources are likely to be neutron stars of mass near the Chandrasekhar limit ($1.4M_\odot$). LMXBs (Low Mass X-Ray Binaries) contain late type stars whose optical luminosity is far lower than that

of the x-ray luminosity. Their orbital periods range from a few hours to a few days implying that the x-ray source is $\sim 1 M_{\odot}$. X-ray pulsators are either HMXB or LMXB whose x-ray luminosity varies due to the channelling of accreting matter onto the poles of a magnetic neutron star. Since the x-ray variability is ultimately due to the rotation of a neutron star these x-ray binary systems are regarded as a kind of pulsar.

Cygnus X-1 is the most well known and probably well documented x-ray binary system. It is a HMXB with an O-type supergiant and a compact source which is almost certainly a black hole. Figure 2.1 shows the COMPTEL spectrum of Cygnus X-1 at energies exceeding 500 keV [49]. The figure shows strong evidence for emission up to 2 MeV and even 5 MeV. Thus although HMXB and LMXB are well known for their x-ray emission they have now been shown to emit at higher energies. A study of the γ-ray emission from an x-ray binary would not only allow a greater understanding of the processes occurring within the individual system but may also have important implications for x-ray binary systems on the whole. A γ-ray study of Cygnus X-1, for example, would increase our knowledge not only on Cygnus X-1 but also on any black hole binary star system and even on other black hole systems such as Active Galactic Nuclei.

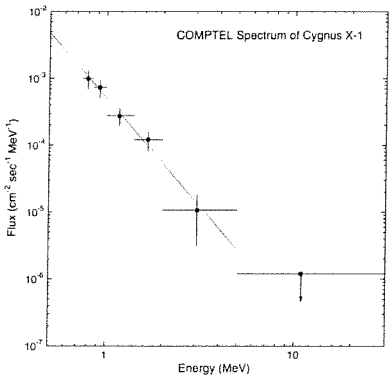

Figure 2.1: Spectrum of Cygnus X-1 derived from COMPTEL data with a best-fit power law of spectral index -3.3 [49].

2.4 Cataclysmic Variables

Cataclysmic Variables are binary star systems where the compact object is a white dwarf and the companion is a main sequence star. Mass transfer onto the compact object occurs through an accretion disk as in figure 2.2 but this may be disrupted if the white dwarf has a strong enough magnetic field. Cataclysmic Variables fall into several categories: Classical Novae, Dwarf Novae, Recurrent Novae and Nova-likes (including Polars and Intermediate Polars). All at some point during their lifecycle

undergo at least one eruption when there is a sudden and unpredictable increase in their brightness. Since Classical Novae are the subject of Chapter 5 of this thesis a more detailed review is provided there.

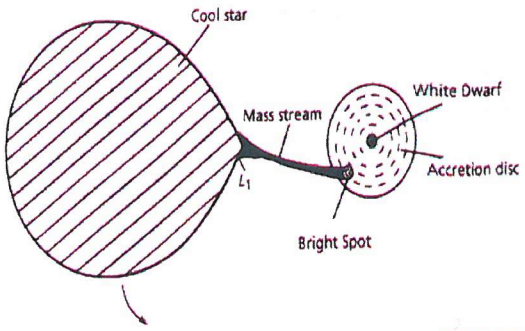

Figure 2.2: Schematic diagram of a cataclysmic variable system as viewed from the pole of the orbit. The "Bright spot" is the point at which the mass stream hits the accretion disk and is a strong source of x and γ-rays. L_1 denotes the inner Lagrangian point where mass leaves the companion and joins the mass stream [70].

2.5 Gamma-ray bursts

Gamma-ray bursts occur approximately once per day and emit almost solely hard x-rays and γ-rays. It is not known how these bursts arise and what the underlying astronomical sources are. Until recently very little was understood even about the distribution of γ-ray bursts. The launch of the Compton Gamma Ray Observatory (CGRO) in 1991 has increased our understanding in this area dramatically. Notably one of the primary objectives of the Burst and Transient Source Experiment (BATSE) was the detection and observation of unknown γ-ray bursts (more information on BATSE and CGRO is provided in Chapter 5).

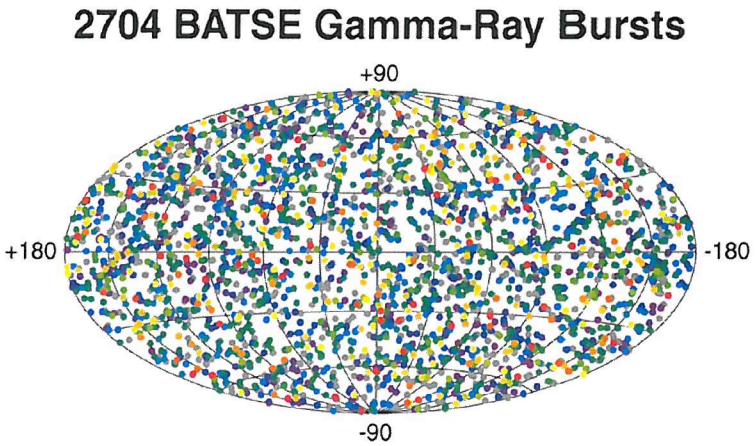

Figure 2.3: The distribution of 2704 γ-ray bursts detected by BATSE. Figure taken from [8] - black and white version obtainable from [50].

Figure 2.3 shows the distribution of 2704 γ-ray bursts which have been detected by BATSE. The distribution is isotropic but inhomogeneous which rules out any theories suggesting that γ-ray bursts are galactic [50]. It is currently believed that these sources lie at cosmological distances with the faintest bursts observed by BATSE lying at redshifts of order 1 [50]. Expansion of the Universe causes the inhomogeneity but the isotropy of the bursts arises naturally.

The duration of γ-ray bursts is difficult to define. Some last 0.1 seconds and some over 1000 seconds. The temporal distribution is, however, bimodal with peaks at $\sim$0.1s and $\sim$10s. The significance of this bimodality is currently a mystery but hopefully future x-ray and γ-ray satellites will advance our understanding.

CGRO has also measured the spectra of γ-ray bursts. The emission is non-thermal and extends up to GeV energies [7]. The spectra of most bursts can be described as a combination of 2 power law spectra joined by an exponential. The spectral index of the lower energy power law is 0 to -1.5 whilst the spectral index of the higher energy power law is -2 to -2.5. The exponential is believed to occur at energies ranging from 100keV to 1MeV [50]. EGRET has detected emission >100MeV from 6 bursts and emission from one particular burst at 18GeV one and a half hours after the onset of the BATSE burst.

At the other extreme optical and x-ray afterglows have also been detected following a number of γ-ray bursts. BeppoSAX was the first to detect afterglow from GRB 970228 just hours after the γ-ray trigger in 1997 ([12, 23, 69]). Since then optical and x-ray afterglow has been associated with many γ-ray bursts and these emissions are now well understood, perhaps even more so than the γ-ray bursts themselves. The afterglow decay obeys a power law: $F_{X-ray} \propto t^{-\alpha}$ where $\alpha = 1.1$ to 1.6 or $F_{optical} \propto t^{-\alpha}$ where $\alpha = 1.1$ to 2.1 [9]. X-ray afterglows last of the order of days whilst optical afterglows often last months.

Until the launch of CGRO γ-ray bursts were believed to be neutron stars. Their isotropic distribution however does not match the distribution of neutron stars. The exact nature of γ-ray bursts is therefore still a mystery. The unprecedented combination of high energy and spatial resolution and large detection volume of INTEGRAL (INTErnational Gamma Ray Astrophysics Laboratory) will hopefully allow us to discover further information on the nature and origin of this class of objects.

2.6 Supernovae

A supernova explosion is one of the most energetic events known. There are two types of supernovae:

Type I Supernovae

Type I Supernovae occur in binary star systems where one of the stars is a white dwarf. Within the class Type I supernovae there are two subclasses. Most type I supernovae are Ib or c. These differ from type Ia in both origin and composition. Type Ia show broad absorption lines, for example from silicon and originate from a white dwarf star that has either merged with a companion or accreted matter from it thereby pushing it over the Chandrasekhar limit and leading to a thermonuclear explosion. Type Ib/c however show no evidence of silicon and are less luminous than type Ia indicating that they produce less radioactive material. Ib/c progenitors are massive stars that have lost their hydrogen rich envelopes through stellar wind or mass transfer onto a companion. Core collapse (rather than a thermonuclear explosion) is likely in type Ib/c supernovae leaving behind a neutron star or black hole with the remnant shell.

Type II Supernovae

The Onion Skin Model shown in figure 2.4a shows the structure of a massive star. The sequence of events leading to the supernova explosion is as follows: hydrogen fuses into helium giving off energy, compression of the accumulated helium increases the temperature leading to the fusion of helium into carbon/oxygen, similarly carbon and oxygen fuse into neon, magnesium and oxygen, which go on to fuse into silicon and sulphur. Silicon and sulphur fuse into iron without producing energy. The iron core collapses and its temperature increases. The outer layers of the star move in to replace the iron core which is now beginning to expand. Shock waves are produced by the colliding core and outer layers resulting in the explosion. A gas shell is ejected with velocities of $\sim$ 10 000 km/s. This gas shell becomes the supernova remnant visible for thousands of years. The original star becomes either a neutron star or a black hole.

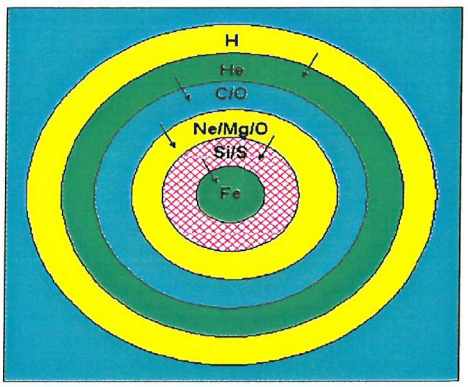

Figure 2.4: The Onion Skin Model for type II supernovae.

A supernova explosion and its decline may last several years but the supernova remnant (the expanding gas shell consisting of supernova ejecta mixed with interstella gas) is visible for thousands of years. Consequently whilst very few supernovae explosions have been observed up to ~120 supernova remnants have been discovered in the Milky Way. These include the Crab Nebula in Taurus and the Veil Nebula in Cygnus. The Crab Nebula is powered by a rapidly rotating neutron star (a pulsar) at its centre corresponding to the collapsed core of the supernova. The appearance of the remnant is therefore bright at the centre but irregular elsewhere. The Veil Nebula however is powered by the supernova explosion itself and has a ringlike structure. The two types of supernova remnants may be correlated to the two types of supernovae.

2.6.1 SN 1987A

Observations indicate that there have been at least 6 supernova explosions in the Milky Way. The explosion of SN 1987A, a type II supernova in the Large Magellanic Cloud, is the most recent and was first observed on 23 February 1987. Subsequently many satellites have been used to analyse the explosion and its remnant across a broad range of wavelengths. Figure 2.5a shows a photo of the remnant of SN 1987A taken with the Hubble Space Telescope. The remnant at the centre is surrounded by inner and outer ring structures. These rings are due to an intermediate wind of velocity ~100 km/s and duration several tens of years [67].

Gamma-ray astronomy relies on the emission of signature γ-ray line photons as a key to unveiling the processes occurring in supernovae. The exponential decay of ^{56}Co has been found to match perfectly the decline of the bolometric light curve of SN1987A. The Gamma-Ray Spectrometer (GRS) on board the Solar Maximum Mission (SMM) was the first to detect the 847 and 1238 keV lines from ^{56}Co. The GRS data thus indicated the existence of explosive nucleosynthesis during the supernova explosion. The thickness of the envelope and distribution of ^{56}Co were also inferred [43].

Gamma-ray spectroscopy has provided a good analysis of SN1987A but the massive ejecta from type II supernovae often obstructs the gamma-ray line fluxes. Type I supernovae are therefore often the target for gamma-ray satellites. It is hoped that the INTErnational Gamma-Ray Astrophysics Laboratory (INTEGRAL - see chapter 8) will unveil previously unknown galactic supernovae through the detection of γ-rays from ^{44}Ti. Extragalactic supernovae may also be detected and analysed through the emission of lines from ^{56}Co.

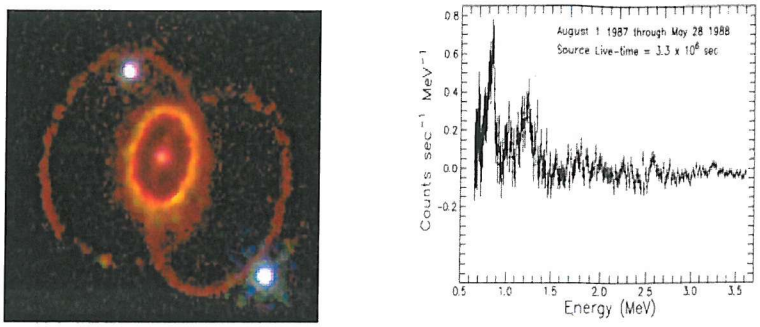

Figure 2.5: a) HST photo of SN 1987A and b) Mean spectrum from 01/08/1987 to 28/05/1988 showing the γ-ray lines from ^{56}Co [42].

2.7 Galactic Centre

The centre of our galaxy is host to a myriad of activity. Unfortunately the galactic centre is obscured in the visible part of the spectrum by dust in the galactic plane. It is therefore crucial to be able to study this region at γ-ray wavelengths.

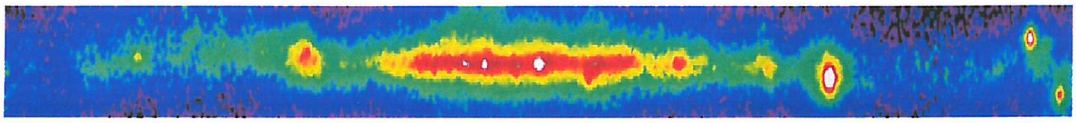

Figure 2.6: EGRET (Energetic Gamma-Ray Experiment Telescope) image of the Galactic plane at energies >100MeV

Figure 2.6 shows a γ-ray image of the galactic plane from EGRET (Energetic Gamma-Ray Experiment Telescope). The direction to the Galactic Centre is represented by the central region of the figure.

Continuum Emission

One of the most controversial aspects of the Galactic Centre is whether the γ-ray emission detected is due to diffuse radiation from the inner Galaxy or whether there is a significant contribution from a selection of point sources. Certainly the centre of our own galaxy has been likened to the nuclei of Active Galaxies albeit on a much smaller scale. This idea was first sporned after the detection of hard x-rays from Sgr A* [65] but since then several other prominant sources have been detected.

In the soft x-ray waveband the source 1E1740.7-2942 is comparable in strength to several other sources. At harder wavelengths (>20-30keV) however this source by far dominates the Galactic Centre region. Its spectrum extends up to several hundred keV and its shape and luminosity (assuming its distance is approximately that of the Galactic Centre) is similar to Cygnus X-1, a black-hole binary star system.

Other hard x-ray sources have also been detected. SIGMA has detected GRS1758-258 in this waveband and at times its hard x-ray emission is comparable to that from 1E1740.7-2942. Until the SIGMA detection this source had gone completely unnoticed due to its proximity to GX5-1. This demonstrates the importance of imaging with fine angular resolution.

The extent of the contribution of these and other unresolved point sources to the γ-ray emission from the Galactic Centre is still uncertain. The broad energy coverage and imaging capabilities of INTEGRAL will allow us to resolve more point sources and possibly distinguish them from the galactic diffuse emission. It is known that Active Galactic Nuclei (see section 2.8) emit γ-rays above and beyond several MeV and it will be interesting therefore to study the centre of our own Galaxy at these energies.

2.7.1 Gamma-ray Line Emission

The detection of a line at 511 keV provides evidence that there is at least one source of narrow 511 keV positron annihilation radiation at the Galactic Centre. Until recently 1E1740.7-2942 was the most likely candidate for this emission. A 2σ upper limit of $2.3\times10^{-4}\gamma\mathrm{cm}^{-2}\mathrm{s}^{-1}$ has been derived for the narrow 511keV line emission from 1E1740.7-2942 [46]. This lead Malet et al [46] to believe in the possibility of a diffuse source of 511keV radiation without the necessity of a central point source. The exact origin of this line remains controversial however and one of the objectives of INTEGRAL will be to study its origin further.

2.8 Active Galactic Nuclei

An active galactic nucleus is the extremely compact central source of a galaxy that emits unusually large amounts of energy. Since it is unlikely that the emission of so much energy could be sustained for a long period of time it is believed that AGN are not a class of galaxy on their own but form a phase in the lifecycle of "normal" galaxies. The most plausible source of energy for AGNs comes from accretion onto the compact source (a supermassive black hole - mass $> 10^8_\odot$).

AGNs do not all show the same characteristics but they do all show at least some of the following:

- Very small angular size. The brightness of the nucleus often dominates any flux emitted by the host galaxy and so the visual effect is that of a point source. This is more noticeable at energies greater than x-rays whilst radio images of AGN often extend over a large area including the jets and lobes.
- High luminosity. AGN have been known to have luminosities exceeding $\sim10^{48}$ ergs^{-1}. This is 10^4 times greater than the power output from a normal galaxy

and may even be an underestimate due to obscuration by extremely thick dust.

- Broad-band continuum emission. Unlike for most galaxies the spectra of AGN are virtually flat from the infra-red region up to the low energy gamma-ray region. Their spectra generally extend to far higher energies than any normal galaxy making them ideal candidates to study with γ-ray satellites.
- Emission lines. Emission lines from AGN are very prominent and can indicate some of the features and processes occuring within the compact source.
- Variability. Variability is often perceived as the trademark of AGNs. Over optical wavelengths only $\sim$10% variation in amplitude can be seen over a few years. At shorter wavelengths however, such as in the x-ray and γ-ray regions the variability can be more than a factor of 10. Furthermore there is a distinct correlation between variability and strength of high energy γ-ray emission.
- Polarisation. The light we receive from most galaxies is $\sim$0.5% linearly polarised due to interstellar dust. The light from AGNs is slightly more polarised ($\sim$0.5-2%) so that the polarisation distribution distinguishes AGNs from normal galaxies. The extent of polarisation does however depend on the wavelengths being detected. There is currently no evidence of polarisation at γ-ray energies and more sensitive instruments than those currently available are required.
- Radio emission. Radio maps of AGN show very clearly the extent of the radio lobes positioned at the end of the jets. The radio emission from AGN is very well studied yet it accounts for no more than $\sim$1% of the bolometric luminosity. It is therefore important that our knowledge from the radio emission is applied to the study of AGN in other wavebands.

The classification of AGN arose unsystematically. The two main classes are Seyfert galaxies (spirals) and radio galaxies (ellipticals). Approximately 150 Seyferts have been identified and they can be split into subclasses according to their spectra. Type 1 Seyferts have broader allowed lines than forbidden lines whereas in Type 2 Seyferts all lines are narrow. The difference arises since the broad allowed lines are thought to be produced in dense gas near the nucleus and this is either missing or obscured in Type 2 Seyferts. Type 2 Seyferts are associated with slightly stronger radio emission than those of Type 1 but neither are strong at radio wavelengths. Hence the second class of AGN is appropriately named radio galaxies. These are characterised by two large radio emitting lobes either side of the nucleus. Blandford and Rees [3] first proposed that the radio lobes may arise through a continuous supply of energy from the nucleus through jets. This fact is in no doubt but there is still a huge lack of knowledge about the content and mechanisms in the jets and lobes. Figure 2.7 shows a schematic diagram of an AGN showing the jets streaming

out of the centrally located black hole and an accretion disk which has developed from matter accreting onto the black hole. The diagram also shows a torus which may develop and consists of gas and dust from the host galaxy.

Figure 2.7: Schematic diagram of an AGN (from NASA Goddard Space Flight Center

2.9 Conclusion

Advances in γ-ray astronomy are essential for a fuller understanding of these sources. The design of a γ-ray detector depends not only on what type of source is to be analysed but also on whether any particular characteristic of those sources is of interest. If a detailed spectral analysis of the source is required, for example to determine its composition, then spectral resolution should be as fine as possible. Angular resolution becomes important when two sources are close together and need to be separately identified. Other characteristics to consider are temporal resolution when the timing of events is required, spatial resolution for position sensitivity, detection efficiency which is particularly important for faint sources and last but not least the practicalities of constructing and launching the detectors and payload. The next chapter therefore discusses the techniques used in γ-ray astronomy and the various designs of detectors and satellites that may be built to achieve the optimum results given the predetermined objectives of the study.

Chapter 3

Techniques in γ-ray astronomy

3.1 Introduction

The search for γ-ray sources such as those discussed in Chapter 2 is vital to our understanding of our universe. Not only is it important to locate these sources but also to extract as much information as possible about how they came about, their physical processes, their size and mass and ultimately their fate.

The detection of γ-ray photons, emitted by these sources, has therefore been the subject of much research over the years. Here the principles behind the detection of γ-ray photons are discussed together with an analysis of how a basic γ-ray detector may be designed. The design of a γ-ray detector must also encompass techniques for the reduction of background noise and these are discussed in the next chapter together with a review of the different types of background noise.

Much of the material for this chapter has been taken from [34], [35] and [44] unless otherwise stated.

3.2 Gamma ray interactions

The three principal ways in which a γ-ray photon can interact in matter are: photoelectric absorption, compton scattering and pair production. Whether one interaction is dominant over another depends on the energy of the initial photon and on the Z number of the absorbing material. This is illustrated in figure 3.1. Each of these processes is discussed in detail in the following sections.

3.2.1 Photoelectric absorption

Photoelectric absorption occurs between a photon and an electron which is bound to an atom. The process is shown in figure 3.2 and is described below:

- Incident photon is absorbed by an atom in the absorber material
- A bound electron gains enough energy to break free from the atom
- The photoelectron (the electron which breaks free) has the energy of the incident photon minus its original binding energy: $E_\beta = h\nu - E_{binding}$

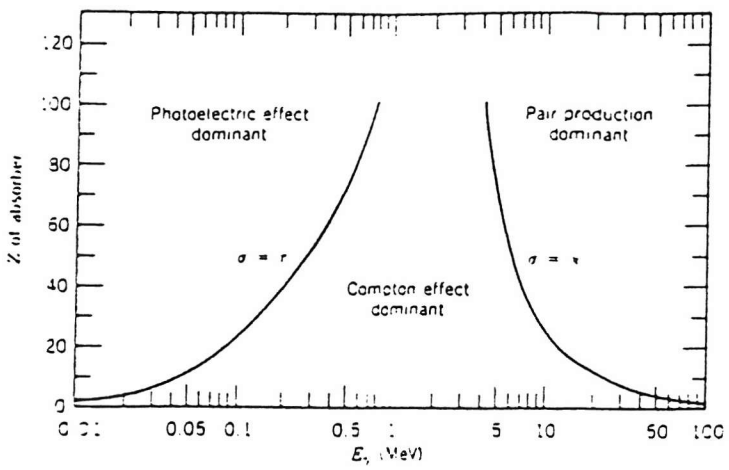

Figure 3.1: The regions of dominance of the three γ-ray interactions, [35]

- The electron deposits all of its energy in the surrounding material through Coulomb scattering
- The shell vacancy left by the photoelectron is quickly refilled by either a free electron or an electron from another shell
- The binding energy is released through a characteristic x-ray or, in some cases, by the emission of another electron (an Auger electron)
- The Auger electron has a very short range (because of its low energy) and is absorbed nearby in the material
- If an x-ray is emitted it may travel further but it is often absorbed nearby and does not escape from the detector
- Thus all of the incident photon energy is absorbed by the material

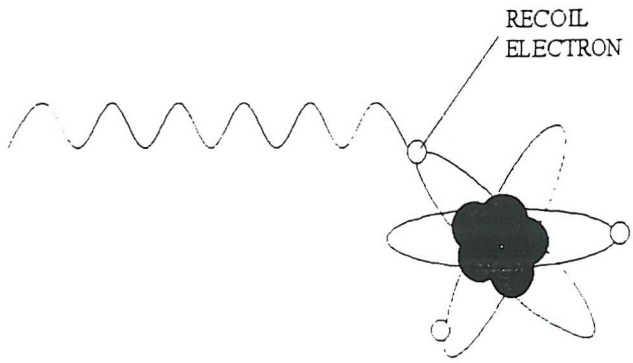

Figure 3.2: Schematic diagram of photoelectric absorption

The probability of photoelectric absorption increases with increasing Z number of the absorber and decreases with increasing energy of the incident photon. The probability can be approximated by:

$$p = c \times \frac{Z^n}{E_\gamma^{3.5}} \tag{3.1}$$

where n is a constant between 4 and 5.

Photoelectric absorption is desirable in γ-ray detectors since all of the incident photon energy is absorbed and therefore detected. Thus to increase the probability of photoelectric absorption it is wise to use high Z materials such as cadmium telluride or mercuric iodide. The advantages and disadvantages of various detectors will be discussed in the following section on "Detector Techniques". It should also be noted that photoelectric absorption drops sharply with increasing energy and it is only dominant below energies of $\sim$ several hundred keV (see figure 3.1). At higher energies the incident photons hopefully scatter to bring their energies down to those favourable for photoelectric absorption.

For a monoenergetic beam of incident photons therefore the spectrum in detector with 100% detection efficiency would be a simple delta function as shown in figure 3.3. The single peak appears at the energy of the incident gamma rays.

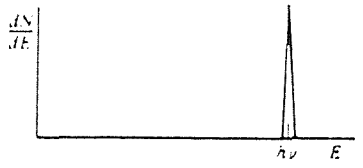

Figure 3.3: The perfect detector response to photoelectric absorption [34].

3.2.2 Compton scattering

As the energy of the incident photon increases (above several hundred keV) the binding energies of the electrons become insignificant and the electrons themselves appear to be "free". This is when Compton scattering begins to dominate over photoelectric absorption. Figure 3.4 illustrates Compton scattering and the process is described below:

- Incident photon scatters from free electron
- A fraction of the photon's energy is transferred to the electron. This energy is absorbed in the nearby material

- The remainder of the energy is carried off by the original photon
- The division of energy between the photon and electron is determined by the scattering angle (θ in figure 3.4)

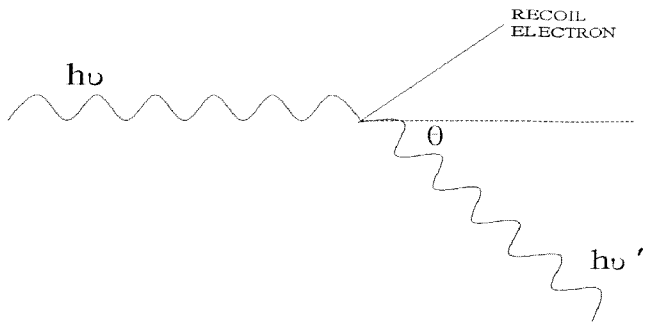

Figure 3.4: Schematic diagram of compton scattering

The energy of the scattered photon is given by:

$$h\nu' = \frac{h\nu}{1 + \alpha(1 - \cos\theta)} \tag{3.2}$$

where

$$\alpha = \frac{h\nu}{m_0 c^2} \tag{3.3}$$

and m_0c^2 is the rest mass energy of the electron (0.511 MeV).
The energy of the recoil electron is therefore

$$E_{e^-} = h\nu - h\nu' \tag{3.4}$$

The two extremes occur when θ=0° and θ=180°. In the former there is no scattering, $h\nu' \cong h\nu$ and $E_{e^-} \cong 0$. Thus the recoil electron has very little energy and the scattered photon has nearly the same energy as the incident photon.

In the other extreme (θ=180°) the photon is backscattered toward its direction of origin and the recoil electron continues along the line of incidence. The maximum energy is transferred to the electron and the energy of the scattered photon is reduced to

$$h\nu' = \frac{h\nu}{1 + 2\frac{h\nu}{m_0 c^2}} \tag{3.5}$$

whilst the energy of the recoil electron is

$$E_{e^-} = h\nu \left(\frac{\frac{2h\nu}{m_0 c^2}}{1 + \frac{2h\nu}{m_0 c^2}} \right) \tag{3.6}$$

The angle of scattering depends on the incident photon energy. At low energies as many photons are scattered back as forward and the final distribution is therefore isotropic. At high energies however (MeV) the photons are nearly all scattered forward.

Compton scattering leads to a continuum spectrum with energy deposits ranging from zero up to the maximum predicted in equation 3.6. Thus the resulting spectrum is not a single peak as in photoelectric absorption but a continuum as shown in figure 3.5.

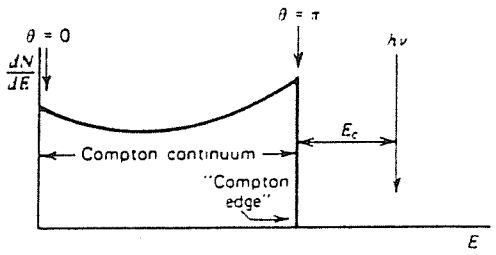

Figure 3.5: The Compton continuum [34]

3.2.3 Pair production

At incident photon energies exceeding several MeV a third γ-ray interaction process begins to dominate. Pair production occurs in the field of a nucleus of an atom and is illustrated in figure 3.6.

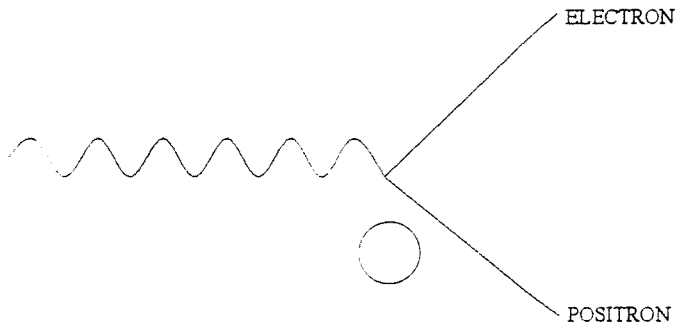

Figure 3.6: Schematic diagram of pair production

- A photon with energy $> 2m_0c^2$ is converted into an electron-positron pair
- Conservation of momentum implies this can only happen in the presence of a third body - usually the nucleus of an atom

- Excess energy of the original photon ($h\nu$-$2m_0c^2$) is converted to kinetic energy of the electron-positron pair
- The pair annihilate with neighbouring charged particles and give rise to two 511keV photons
- Both of these may be absorbed in the material or one or both of the 511 keV photons may escape from the absorber. This gives rise to escape peaks at ($h\nu$-511) keV and ($h\nu$-1022) keV in the resulting spectrum.

Although in theory pair production can occur at energies exceeding 1.022 MeV in practice it is not a dominant process until above several MeV.

The overall resulting spectrum in the detector therefore depends on the energy of the incident photons and the thickness of the material used as the detector. Figure 3.7 shows two possible spectra depending on the processes which dominate. At high energies in thin ($< \sim$1cm) detectors pair production will be a dominant process and escape peaks will appear strongly in the spectrum. At the other extreme with low energy photons ($<$ 1 MeV) there will be no escape peaks as photoelectric absorption and compton scattering will dominate. The resulting spectrum in this case would therefore be a compton continuum with a photopeak at the energy of the incident photons.

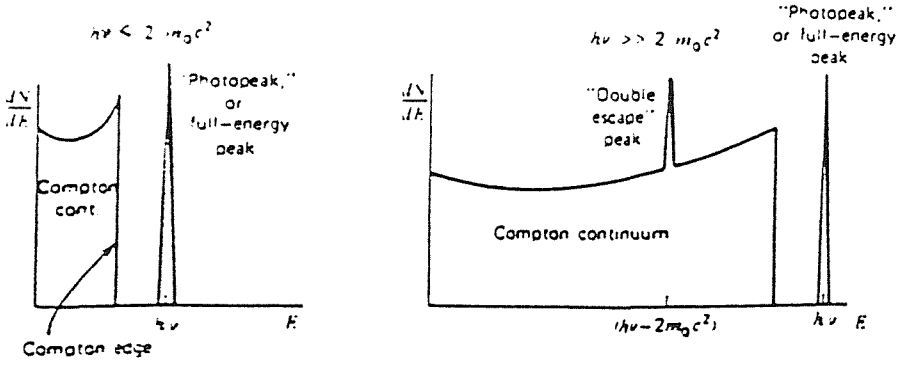

Figure 3.7: The diagram on the left shows a typical spectrum for low energy incident photons ($<$ 1.022 MeV) with a Compton continuum arising from compton scattering and a photopeak resulting from photoelectric absorption (or compton scattering where the scattered photons do not escape). The diagram on the right shows a spectrum typical at higher energies where pair production gives rise to escape peaks [34].

3.3 Detector techniques

A detector system consists of an imaging system and shielding system as well as the detector itself. In the next two sections detector and imaging techniques are explained respectively. A discussion of shielding systems is deferred until the next chapter on background noise and its reduction. The design of a γ-ray detector system depends on a variety of factors and these include:

- Energy range to be detected. This will influence mainly the detector material but also the degree and type of shielding required
- Spectral resolution. Some materials provide much better spectral resolution than others but may themselves have other disadvantages.
- Detection efficiency. How many of the incoming photons will be detected by the detector material?
- Field of view. How wide does the field of view have to be?

There are a variety of detectors that can be used. Gas-filled counters operate below $\sim$150keV and are therefore only discussed very briefly below. Semiconductor diode detectors and scintillation detectors, however, are used in the γ-ray satellites studied here and a fuller discussion of these is provided.

3.3.1 Gas Counters

As already mentioned gas counters can be used to detect radiation below $\sim$150 keV. Figure 3.8 shows how the pulse height varies with applied voltage for ionisation chambers, proportional counters and Geiger-Muller tubes.

Ionisation chambers are the simplest type of gas counter. They operate using two parallel plates, the volume between which is filled with gas, often air. The radiation ionises the gas and the resulting ions are accelerated towards the plates creating a pulse. The pulse height is directly proportional to the energy of the ionising radiation and not to the applied voltage. The applied voltage does, however, affect the speed at which the ions move and therefore how quickly the incident radiation is detected. Thus ionisation chambers, which allow the ions to drift slowly to their respective plates, cannot detect individual pulses. If the applied voltage is increased the original electrons move faster and ionise the gas further (a Townsend Avalanche). This creates a number of secondary electrons proportional to the number of primary electrons. The resulting detector gives an output pulse proportional to the incident radiation and is called a Proportional Counter. These counters can distinguish individual pulses up to $\sim 10^6$ per second. If the applied voltage is increased even further then each avalanche itself creates further avalanches and the output pulse is no longer proportional to the original number of electrons created. This type of detector is called a Geiger-Muller tube whereby all types of incident radiation produce identical output pulses.

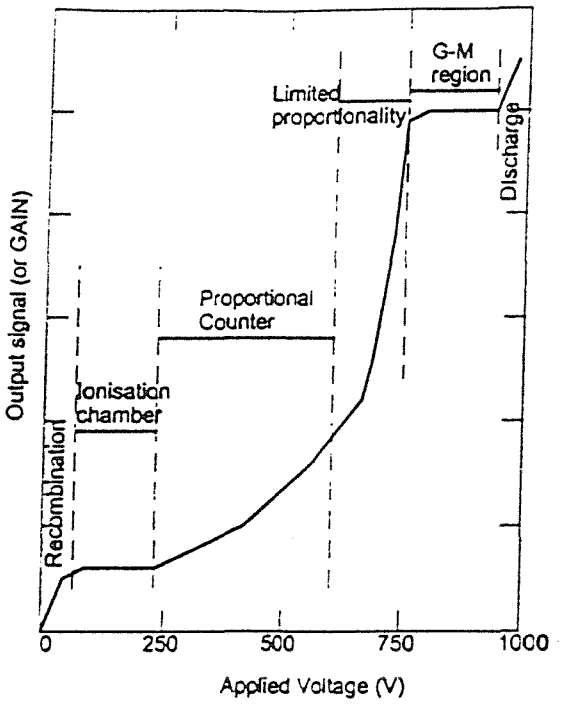

Figure 3.8: The variation of pulse height with voltage for gas-filled counters.

3.3.2 Semiconductor diode detectors

A semiconductor is a crystalline solid in which the electrical conductivity is intermediate between that of a conductor and an insulator. At room temperature, electrons can migrate from the top of the valence band to the conduction band.

To control conduction in semiconductors dopants are added. If for example the semiconductor has valence 4 (as in germanium) then a dopant of either valence 3 or 5 is added. When an atom of a dopant of valence 5 replaces an atom of the germanium there is an extra electron per atom available for conduction. Thus electrons are the primary charge carriers and the material is said to be an n-type semiconductor. Conversely when an atom of a dopant of valence 3 replaces an atom of the germanium there is an excess of holes which can accept electrons from the valence band. The holes are the primary charge carriers and the material is said to be a p-type semiconductor.

When a p-type material comes into contact with an n-type material then electrons migrate from the n-type to the p-type and combine with the excess holes. Around the junction of the two materials a depletion region forms in which the charge carriers have been neutralized. A large reverse bias voltage (100-3000V) applied across the detector increases the size of the depletion region (by encouraging charge carriers to drift from one type of material to the other).

Figure 3.9 shows the principle behind a semiconductor diode detector. A γ-ray photon passing through the depletion region of the material creates electron-hole pairs along its path. The energy required to produce an electron-hole pair is called

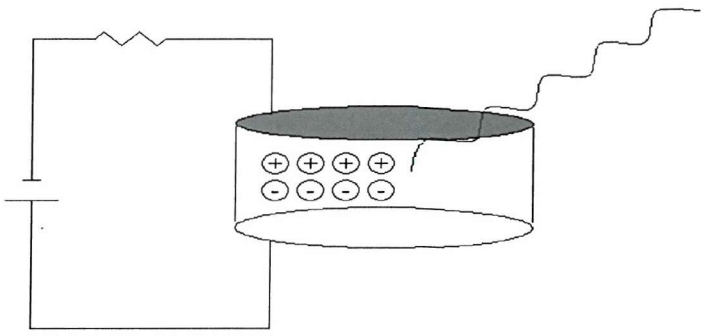

Figure 3.9: A semiconductor diode detector

Property	Ge	CdTe	HgI_2
Band gap (eV)	0.73	1.47	2.13
Ionisation energy (eV)	2.98	4.43	4.22
Operating temperature (K)	77	300	300
Density (g/cc)	5.36	6.06	6.40
Highest Z	32	52	80
Spectral resolution	0.5% @ 100keV	3% @ 60keV	20% @ 30keV

Table 3.1: Properties of semiconductor detector materials

the ionisation energy (~3 times the band gap in table 3.1). The electrons and holes drift towards their respective plates creating a detectable drop in voltage across the detector. This drop in voltage is the output pulse and is directly proportional to the energy deposited in the detector material.

Table 3.1 shows the main properties of some common semiconductor diode detector materials. The ionisation energy is proportional to the band gap so the lower the band gap the more electron-hole pairs are created in the material for a given photon. This improves the energy resolution of the detector for two reasons. Firstly the statistical fluctuation in the number of charge carriers becomes a lower percentage of the actual number of charge carriers. Secondly a greater charge per pulse increases the signal and improves the signal to noise ratio.

Thus a material with a low band gap will provide good energy resolution. From table 3.1 germanium has the lowest band gap and therefore has the best energy resolution. Other factors, however, have to be taken into consideration. Equation 3.7 shows that the band gap also determines the probability of thermal generation

of electron-hole pairs. Thus to reduce thermally generated noise the ratio of the band gap to the temperature needs to be kept low. For this reason germanium and other low band gap materials have low operating temperatures as shown in table 3.1. This implies expensive and bulky cooling devices which can restrict the lifetimes of the their host satellites.

$$p(T) = CT^{\frac{1}{2}}e^{-\frac{E_g}{2kT}} \tag{3.7}$$

Each of the materials detailed in table 3.1 will now be described in more detail.

Germanium

Early germanium detectors were made by fusing lithium (Li) onto the surface of p-type germanium. When reverse-biased the n-type Li drifts into the p-type region creating a depletion region. These detectors were known as Ge(Li) detectors. In order to prevent the Li from migrating out of its lattice sites (thereby ruining the depletion region) the detectors had to be cooled constantly to 77K. By the early 1980s therefore High Purity Germanium had been developed which needs cooling only during operation (to reduce the thermal noise) and not constantly.

Germanium detectors provide excellent spectral resolution (Full Width Half Maximum resolution of $\sim$ 1 keV at 1 MeV [19]) due to the small band gap energy and thus low ionisation energy. Unfortunately, as discussed earlier, this does mean they have to be cooled to 77K during operation. Coolers have been developed specifically to allow germanium to be used on-board satellite missions but the lifetime of the satellite is restricted to approximately 5 years due to the amount of coolant that can be carried.

There are two main configurations of germanium detectors: planar and coaxial. Both are shown in figure 3.10. The maximum active volume for the planar configuration is only $\sim$30 cm^3 since the crystals can only be made a few centimetres in diameter and $\sim$2cm thick. The coaxial configuration however can provide a much larger active volume since the crystal can be made larger in the axial direction. Coaxial configurations are therefore often favoured since they provide much better detection efficiencies.

Much research has been invested into materials that have good spectral resolution but do not require cooling. Cadmium telluride and mercuric iodide both fall into this category and are discussed below.

Cadmium Telluride

Cadmium telluride has a larger band gap than germanium and thus poorer energy resolution. As a result of its larger band gap however cadmium telluride can be operated at 300K and does not require cooling. Thus in designing a γ-ray system there is a trade off between spectral resolution and cooling. If slightly worse spectral

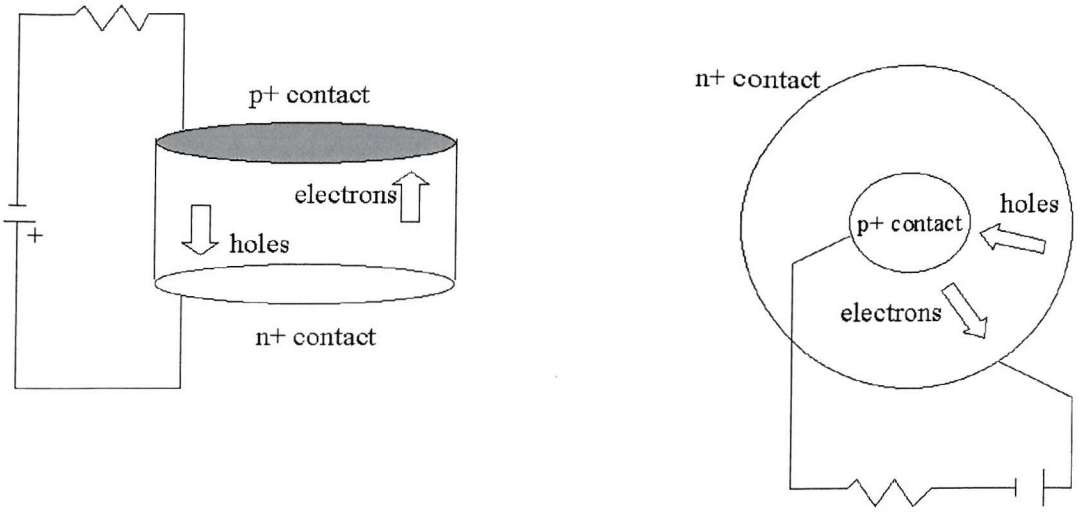

Figure 3.10: Planar and coaxial germanium detector configurations

resolution can be tolerated then cadmium telluride or mercuric iodide (discussed next) are more suitable choices of material.

Cadmium telluride also has a high Z (favouring photoelectric absorption) and high density which increases the γ-ray stopping power. The main disadvantage of this material is that it suffers from a problem known as "charge trapping". The electrons and holes in the material have a low mobility and do not always reach their respective electrodes but get trapped along the way. This effect shows up as a tail on the peak of the spectrum where the full signal has not been collected (see figure 7.9). The rise-time of the signal will depend on the amount of trapping present and its measurement will allow the true pulse height to be reconstructed (though there will always be some uncorrectable events). Thus, even after correction of charge trapping, the energy resolution of the detector is $\sim$1.7 keV at 60 keV or $\sim$3.5 keV at 122 keV (FWHM).

Another problem of cadmium telluride is that of growing large enough crystals. At present the largest pixels that can be grown are $\sim 10 \times 10 \times 2$mm which will only stop photons up to $\sim$250 keV. For higher energy γ-rays a matchstick configuration must be used where the pixels are $\sim 2 \times 2 \times 10$mm and the γ-rays fall incident along the 10mm axis. To achieve a reasonably sized detector plane in this way would require thousands of pixels.

Thus although cadmium telluride has the advantage of a reasonable operating temperature it does not offer the spectral resolution that germanium can and suffers from charge trapping. Cadmium telluride forms part of the detector plane of LEGRI (Low Energy Gamma Ray Imager) onboard the Minisat-01 satellite and ISGRI onboard INTEGRAL.

Mercuric Iodide

Mercuric iodide is also a room temperature semi-conductor diode detector. The spectral resolution should be better than that of cadmium telluride since it has a lower band gap energy. The charge trapping effects, however, are far greater and mercuric iodide offers much poorer resolution.

Mercuric iodide is discussed in detail in Chapter 6 (section 6.1) since its feasibility was one of the objectives for the γ-ray detector LEGRI (Low Energy Gamma Ray Imager).

3.3.3 Scintillation detectors

Scintillation detectors work in two stages: the scintillation event itself followed by the detection of the scintillation photons. The whole process occurs as follows:

- Gamma ray photons enter the scintillator material and excite the atoms
- The excited atoms emit visible or near-visible light
- Photoelectrons are produced when this light strikes a photosensitive surface
- These electrons are then multiplied, accelerated and formed into an output pulse.

The first two stages occur in the scintillator material and the last two in a photomultiplier tube. An alternative to the photomultiplier tube is a photodiode. A photodiode does not introduce internal gain but is less bulky than a PMT and may therefore be more suitable for use with large numbers of small pixels (now very common in γ-ray astronomy). There are many different types of scintillator material. Inorganic scintillators provide the best light output and linearity but often have slow response times. Organic scintillators however have faster response times but lower light yields. Organic scintillators are often made from plastic and are used in γ-ray detectors as active shielding. They are therefore discussed in the next chapter as a technique for background noise reduction. Inorganic scintillators, however, are often used as the detector material as their higher density provides better stopping power for the incident radiation. Table 3.2 shows the wavelength of the maximum emission, the refractive index, the density and the light yield for several common inorganic scintillators. The (Tl) and (Na) in the table refer to small amounts of activators that are added to the scintillators to increase the probability for photon emission and reduce self-absorption of the light. Thallium and sodium are the most commonly used.

The wavelength of the maximum emission determines the nature of the device which will convert the photons into an electronic pulse. Photodiodes work better with longer wavelengths whilst photomultiplier tubes work better at shorter wavelengths.

Property	Maximum emission (nm)	Refractive Index	Density (g/cc)	Light yield (Photons/MeV)
NaI (Tl)	415	1.85	3.67	38000
CsI (Tl)	540	1.80	4.51	52000
CsI(Na)	420	1.84	4.51	39000
BGO	505	2.15	7.13	8200

Table 3.2: Common properties of some inorganic scintillators

A high refractive index would be unfavourable since total internal reflection could prevent some of the light from leaving the material and thus from being detected in the photodiode or photomultiplier tube.

The density, together with the Z number, determines the stopping power of the material. Bismuth Germanate (BGO) has the highest density and is therefore often used in active shielding. The applications of BGO are discussed in the next chapter with other techniques for the reduction of background noise.

A high light yield is favourable since it improves the spectral resolution of the detector and determines the minimum energy which can be detected. The best light yield is achieved by CsI (Tl).

Each of the inorganic scintillators shown in table 3.2 will now be discussed in turn.

Sodium Iodide

In 1948 Hofstadter discovered that sodium iodide (NaI) mixed with thallium iodide produced a scintillator material with an unprecedented light yield. In spite of rigorous research into other scintillators NaI(Tl) is still used as a detector material today (though its high light yield has now been superceded by, for example, CsI(Tl)).

Although crystals of NaI are fragile, detectors of a variety of shapes and sizes can be produced. The crystals are hygroscopic and must be kept in an airtight container to prevent exposure to moisture in the atmosphere. Another drawback is that the decay time of each scintillation pulse is slow (230ns) and approximately 9% of the overall light yield results from phosphorescence with a decay time of 0.15s. Thus when the count rate is high there is not enough time for recovery in between pulses. NaI(Tl) is not, therefore, suitable for applications where the count rate is expected to be very high but is fine for γ-ray astronomy where the count rate is relatively low.

In spite of this, the high light yield and linear response of NaI provide a good basis for γ-ray spectroscopy.

BATSE (Burst and Transient Source Experiment) uses 8 detector modules each containing two NaI scintillation detectors used in conjuction with photomultiplier tubes (see Chapter 5). The Large Area Detector (LAD) is optimised for sensitivity

and directional response whilst the Spectroscopy Detector (SD) is optimised for spectral coverage and resolution.

Caesium Iodide

Caesium iodide produces longer wavelength light than NaI and is more suited to a photodiode readout device. Silicon photodiodes are often used since they provide excellent long term stability [4]. CsI can either be used with thallium or sodium as the activator and there are therefore two different types of CsI used in γ-ray detectors (as shown in table 3.2). The main advantages of CsI are that it

- has good spectral resolution as it has a high photon yield
- it is malleable and can therefore be bent into various shapes and sizes without fracturing
- has a variable decay time which allows different types of radiation to be distinguished using pulse shape discrimination.

CsI is however slightly hygroscopic and will deteriorate if exposed to water or conditions of high humidity. It also emits light at long wavelengths and does not work well with a photomultiplier tube. A photodiode with extended response into the red region is often, therefore, used in conjunction with CsI.

The Imager on board INTEGRAL (INTErnational Gamma Ray Laboratory) contains a detector plane of 4096 CsI pixels (PICsIT) which sits behind a detector plane of 16384 CdTe pixels (see Chapter 8). The CdTe serves to bridge the energy gap between the CsI and JEM-X (the X-ray monitor).

3.4 Imaging techniques

Table 3.3 details some of the common imaging techniques used in γ-ray astronomy. Each of these are listed below with brief details on their principle of operation:

- Grazing Incidence Optics. X-rays strike a reflecting surface at very small angles and are focused on the detector plane. This type of system is used mainly for low energy imaging since the angle of incidence required becomes extremely small (and hence the telescope increasingly long) for energies much greater than $\sim$15keV. The ROSAT observatory, which operates in the energy range 0.1-2.4keV, contains four nested mirrors with a gold coating to ensure good reflectivity. The reflecting surfaces of Grazing Incidence Optics can be coated with graded multilayer structures. This has the effect of increasing the grazing angle for which significant reflectivity can be obtained and as such the energy range of operation can be extended up to higher energies ($\sim$60keV). Constellation-X (still under design/construction) is an example of such a system.

- Bragg Crystals. Bragg crystals work up to several hundred keV and are based on diffraction crystals that "focus" γ-rays from a large collecting area onto a small detector volume. The inclination angle of the crystals and the distance to the detector plane determine the energy band of detection. As a result of the small detector volume required the background noise is extremely low which allows unprecedented sensivities. A crystal diffraction lens containing 600 single crystals of germanium has been constructed at the Argonne National Laboratory [66].
- Rotation Modulation Collimators. As the collimator and detector rotate the source comes into and out of the field of view. Every position on the sky gives a unique lightcurve and backprojection therefore allows the position of the source to be determined. Four RMCs, each pointing in different directions, are used on the GRANAT satellite as γ-ray burst detectors [6].
- Earth Occultation. This technique, where the earth is used as a modulator, is the basis for BATSE and is therefore discussed in more detail below.
- Coded Aperture. Coded mask imaging is based on the simple pinhole camera principle and is used in both LEGRI and INTEGRAL. Again this is discussed in more detail below.
- Compton Telescopes. Between approximately 0.8 and 30 MeV the dominant γ-ray interaction mechanism is compton scattering. If the positions of at least two interactions are known then a Compton event circle can be used to build up a probability distribution of the astronomical source on the sky. This type of imaging is used in the COMPTEL instrument onboard the CGRO [57].
- Spark Chambers. The direction of incoming photons is determined by studying the tracks of electron-positron pairs created by pair production (pair production is described in section 3.2). Since spark chambers are reliant on pair production they are used for very high energy imaging. EGRET (The Energetic Gamma Ray Experiment Telescope onboard the CGRO [33].) operates at energies above 30MeV and uses a spark chamber imaging system.

3.4.1 Earth Occultation Imaging

Earth occultation imaging is the technique behind BATSE (Burst and Transient Source Experiment - see Chapter 5). It is a form of modulation imaging where an object is used to block the field of view thereby exposing the position of the source as a function of time. In Earth occultation imaging the Earth is used as the modulator as shown in figure 3.11. Known source locations can be checked for discontinuities in the background noise at the time of rise or set of the source at the earths limb. Previously unknown sources may also be detected by searching for

Imaging technique	Energy range	Angular Resolution	Used on
Grazing Incidence Optics	< 15keV	5 arc sec	BeppoSAX [11]
Spark Chambers	10MeV-20GeV	~1°	EGRET [33]
Compton Telescopes	0.8-30MeV	~2°	COMPTEL [57]
Rotation Modulation Collimators	10-200keV	~1-10arcmin	HESSI [59]
Earth Occultation	any	1°	BATSE [16]
Coded Apertures	10keV-10MeV	1-10 arcmin	LEGRI & INTEGRAL (chapters 6-8)

Table 3.3: Details of the most common imaging techniques

occultation steps. More information on this technique can be found in Chapter 5 or [24].

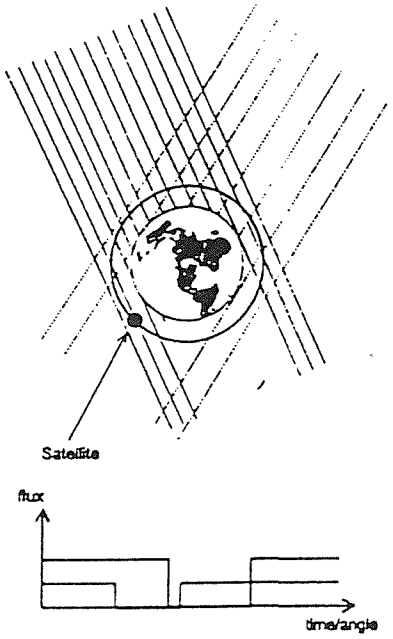

Figure 3.11: Schematic diagram of Earth Occultation Imaging

3.4.2 Coded mask imaging

The main imaging technique used by the satellites modelled in this thesis is coded mask imaging. This technique works on the same principle as a pin-hole camera. One small pinhole provides good resolution but the sensitivity is limited by the size of the pinhole. Making the pinhole larger increases the sensitivity, ie the number of photons reaching the detector plane (in the case of a pinhole camera a piece of paper!), but decreases the angular resolution. To overcome this many pinholes can

be used simultaneously to increase the number of photons whilst maintaining the resolution of the picture. A coded mask operates on the same principle. The mask contains opaque elements of, for example, tungsten and transparent elements which act as the pinholes.

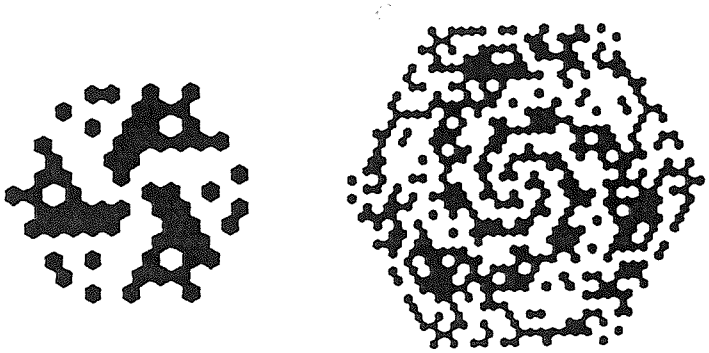

Figure 3.12: Unit patterns for two HURAs (Hexagonal Uniformly Redundant Arrays) of order 127 and 919 respectively

Photons coming from a source project an image of the mask pattern on the detector plane but shifted if off-axis. The detector accumulates a number of shifted images with each shift indicating the position from which the photons originated and the intensity of the shifted image gives the intensity of the source at that position. The image can therefore be deconvolved to determine the exact position and intensity of the source.

There are several methods of deconvolution and these include:

- Back projection. Each photon is projected onto every possible position on the sky from where it may have come. With more and more photons an image of the source can be built up.
- Cross correlation. Very similar to back projection. A shadowgram is recorded and correlated with a deconvolution array for all possible sky positions. Analogous to searching for the mask pattern in the recorded shadowgram.
- Maximum likelihood. A number of different sky distributions are folded through the telescope response and a shadowgram is obtained for each. The one with the best fit, generally using χ^2, is used as the image of the sky.
- Maximum entropy. Similar to maximum likelihood but the lowest χ^2 model is not necessarily chosen as the image. Rather a range of acceptable χ^2 models are selected and other knowledge, such as the field contains only point sources, is used to determine the most probable sky distribution.

Coded masks fall into two main categories: Non uniformly redundant arrays (NRAs) and Uniformly redundant arrays (URAs). Put simply NRAs are those masks where every spatial frequency is sampled only once whilst URAs are those where every spatial frequency is sampled the same amount of times. Hexagonal Uniformly Redundant Arrays (HURAs), examples of which are shown in figure 3.12, form a subset of URAs where the URA itself is mapped onto a hexagonal grid. This allows, for certain orders, antisymmetry through 60^0 and therefore greater imaging capabilities.

Coded mask imaging also provides excellent background subtraction since the opaque mask elements allow the detector to measure the background noise whilst the clear elements view the source.

3.5 Conclusion

Gamma-rays can interact in matter by photoelectic absorption, compton scattering or pair production. Photoelectric absorption is often preferable in detecting γ-rays since the photoelectron deposits all of its energy in the surrounding material and the resulting spectrum is a peak at the energy of the incident photons. Compton scattering however produces a Compton continuum since, depending on the angle of scattering, some of the energy may be carried off by the original photon. Pair production gives rise to escape peaks where either or both of the electron-positron pair escape from the detecting material.

The spectrum of an interacting photon will not only depend on the type of interaction dominating but also on the detector material used. High density materials provide good stopping power and high Z materials increase the probability of photoelectric absorption. There are several types of detector material used in γ-ray astronomy including gas, semiconductor diodes and scintillators. There are advantages and disadvantages of each and there is no single obvious choice for use in a γ-ray telescope. The objectives of each mission must be used to define the criteria for the detectors used.

As mentioned before a detector system not only includes the detector itself but also an imaging system and shielding. There are many different imaging techniques and some of these have been discussed above. The most relevant techniques for the purpose of this thesis are Earth Occulation imaging, where the Earth is used as a modulator, and Coded Mask imaging, where a mask acts as a series of pinholes. The next chapter provides an overview of the different types of background noise together with a summary of techniques often used to either reduce or estimate its effects. Shielding, a common background reduction technique, will therefore be discussed in the next chapter.

Chapter 4

Background Noise

4.1 Introduction

The previous chapter discusses the design of a γ-ray telescope with respect to the detector material and imaging techniques. Unfortunately γ-ray satellites are exposed to radiation other than that from the sources which they are observing. This background radiation increases the count rate in the detectors which may then provide misleading data. Furthermore since, $F_{min} \propto \sqrt{B(E_\gamma)}$ (where F_{min} is the instrument's minimum detectable flux and B is the background noise in the detector system at energy E_γ) then as the background noise increases the minimum flux detectable also increases according to its square root. Thus reducing the background noise improves the sensitivity of the instrument enabling lower fluxes, for example from fainter sources, to be detected.

Techniques for the reduction of the background noise count rate include shielding and collimation. Alternatively if the background noise can be measured accurately, for example through the use of a coded mask, then it does not necessarily need to be blocked, just subtracted from the source data during analysis. Even if the detector system has been designed to block or measure the background noise, Monte-Carlo simulation techniques can be used to estimate its effects on the detector system and thus improve its sensitivity. This technique is now so sophisticated that some satellites rely almost entirely on the simulation and subsequent subtraction of the background noise rather than on the detector system design.

Here the different types of background noise are discussed together with some techniques currently used to minimise the effects of this noise on γ-ray instruments. An introduction is provided on Monte-Carlo simulations and the software used to estimate the processes occurring in γ-ray detectors after background noise irradiation.

4.2 Sources of background noise

Gamma-ray telescopes, which often operate at the top of the Earth's atmosphere or on a space platform, are subjected to an intense radiation environment. In order to determine a source's true emission intensity, therefore, it is crucial to be able to estimate the effects of this radiation environment.

The background noise in a γ-ray telescope can either be induced by γ-ray photons (cosmic diffuse γ-rays, atmospheric γ-rays and locally produced γ-rays) or hadrons (cosmic ray protons, neutrons and trapped protons due to radiation belts).

The geomagnetic field prevents cosmic rays below a certain cut-off rigidity from reaching the earth [14]. This effects all types of background noise dependant on cosmic rays (atmospheric γ-rays, cosmic ray protons and neutrons) and alters their spectral shape and intensity near the poles compared to at the equator.

Each of the different types of background noise will now be discussed in turn.

4.2.1 Cosmic diffuse γ-rays

The origin of cosmic diffuse γ-rays has been the subject of much controversy over the years. Only a quarter of the γ-ray flux can be accounted for by emissions from Active Galactic Nuclei and other discrete sources [10], [51]. Several theories have been proposed on the origin of the remaining diffuse γ-ray background. Watanabe et al suggested that γ-ray production in supernovae may be partly or even completely responsible [71]. More recently Loeb et al showed that highly relativistic electrons, produced during the formation of large-scale structure, may scatter some of the photons of the Cosmic Microwave Background Radiation up to γ-ray energies thereby producing the cosmic diffuse γ-rays [45].

The origin of the cosmic diffuse background γ-rays is of less importance here, however, than the intensity and energy range of the flux itself. The late 1970s and early 1980s saw much research into defining the spectral shape and intensity of the cosmic diffuse flux. Figure 4.1 shows the spectrum obtained by Schoenfelder et al in 1980 [60] compared with others. All measurements, in the energy range considered, tend to converge and support the existence of a "bump", above a straight line extrapolation, at energies of several MeV [60]. This "bump" has recently been shown to be an artefact and the spectrum is in fact smooth with a transition from a softer to harder component around several MeV [73]. Mandrou et al [47] produced a very similar spectrum to Schoenfelder but more accurately determined the spectral index of the Cosmic Diffuse flux to be $\sim$ -2.3.

The isotropy of the Cosmic Diffuse flux was tested by Schwartz (for energies $<$ 100 keV) [62], Mandrou (for energies $>$300 keV and $<$ 2 MeV) [48] and Schonfelder (for energies $>$ 1 MeV) [61]. All are consistent with the flux being isotropic.

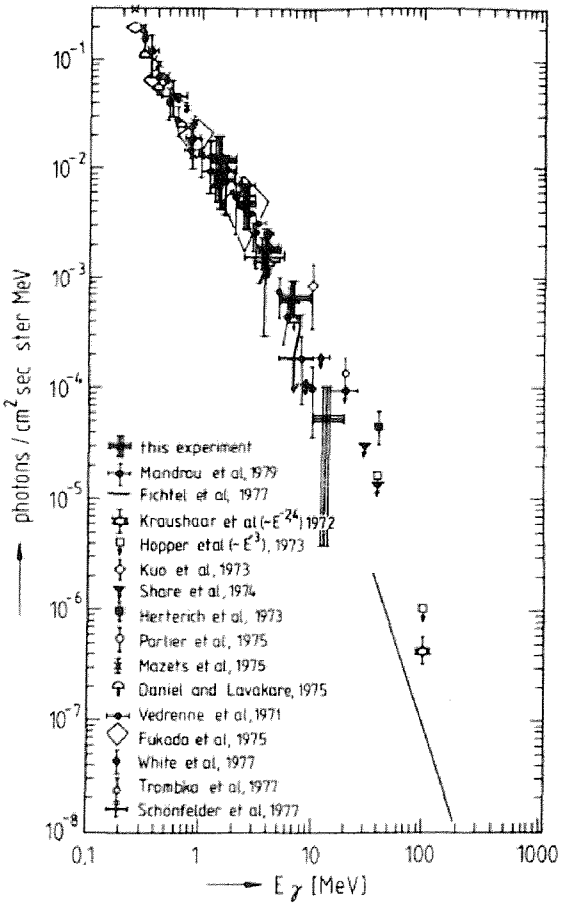

Figure 4.1: Comparison of the Cosmic Diffuse spectrum of Schoenfelder et al and others [60]

Thus although the Cosmic Diffuse background flux may have interesting cosmological implications it creates a background which must be taken into account in γ-ray observations. The spectrum steepens at around a few MeV but otherwise follows a smooth power law with spectral index of $\sim$ -2.3. Its isotropic nature enables Monte-Carlo simulations to easily and accurately predict the effects of the Cosmic Diffuse flux on γ-ray detectors.

4.2.2 Atmospheric γ-rays

Although of less cosmological significance than the Cosmic Diffuse γ-rays, atmospheric γ-rays have also been studied quite heavily. Figure 4.2 shows a comparison of the spectrum obtained by Schoenfelder et al [60] with others. As for the Cosmic Diffuse flux the different results are in good agreement and the spectrum of the Atmospheric flux is a power law [60]. The Atmospheric flux is also isotropic [14].

Atmospheric γ-rays are derived from cosmic ray interactions in the atmosphere. Thus since they are dependent on cosmic rays they are also rigidity dependent ie the atmospheric flux intensity and spectral shape is different at the poles compared to at the equator. The spectral index of the atmospheric flux is -1.34 at the polar

cap and -1.39 in equatorial regions [29]. The intensity of the flux at the poles is also greater (by approximately a factor of 2) than at the equator.

At low altitudes (typically for balloon experiments) the atmospheric γ-ray flux is more intense than the cosmic diffuse flux. In such cases, however, the atmospheric and cosmic diffuse fluxes are indistinguishable and often only the combined flux is quoted. At higher altitudes however the atmospheric flux becomes almost negligible and the cosmic diffuse flux dominates over the two.

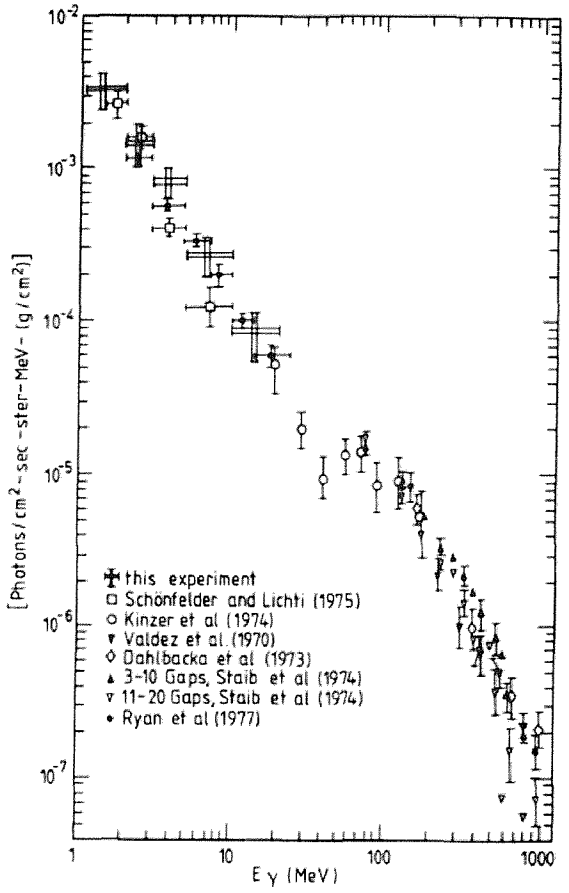

Figure 4.2: Comparison of the Atmospheric spectrum of Schoenfelder et al and others taken above Palestine, Texas. [60]

Thus although the atmospheric flux is isotropic and has a constant spectral shape it can be complicated and CPU intensive to simulate. Due to rigidity dependance the flux at the poles is different to at the equator and the two must be dealt with separately. This could require either separate Monte-Carlo simulations or one Monte-Carlo simulation with a scaling factor for the flux at the poles.

4.2.3 Cosmic ray protons

Cosmic ray particles are produced by, for example, binary star systems, supernova remnants and Active Galactic Nuclei. Primary cosmic rays are collectively the original particles which have been emitted by the sources and are mainly composed

of protons but also include, for example, electrons and positrons. Secondary cosmic rays are those which reach the earth's atmosphere and interact to give an "air shower" of elementary particles. These secondary cosmic rays include neutrons (see next section).

Cosmic ray protons can interact with a spacecraft and its materials and create a background noise count rate in the detectors. There are two components to the background noise count rate created - the instant γ-rays and electrons created from excited nuclei (the prompt component) and the γ-rays due to the decay of long-lived excited nuclei (the delayed component). The prompt component can be eliminated by the veto counter but due to the finite length of the veto pulse (see section 4.3) the delayed component cannot.

Various estimates of the incident cosmic ray proton flux on a satellite and its detectors have been made. In the Earth's atmosphere the proton flux of Hayakawa can be used [25] where the flux is heavily dependent on the atmospheric depth. For satellites which are further out, however, the atmospheric depth is less important and the flux of Webber & Lezniak [72] can be used (see equations 4.4 and 4.5). The cosmic ray proton flux is rigidity dependent and the flux at the poles is therefore different to at the equator.

4.2.4 Cosmic ray neutrons

As discussed above cosmic rays which are made up of a range of particles are emitted by galactic and extra-galactic sources. Neutrons are secondary cosmic ray particles because they are generated by interactions of the primary cosmic rays in the atmosphere and possibly the spacecraft. The effects of the primary and secondary cosmic ray protons far exceeds the effect due to secondary neutrons. For this reason most modelling of the background noise in detectors, including that in this thesis, does not include modelling the effects of neutrons.

4.2.5 Radiation belts

The Van Allen radiation belts are two regions within the Earth's magnetosphere in which particles become trapped and oscillate back and forth between the magnetic poles. The South Atlantic Anomaly (SAA) is the region where the Inner Van Allen belt dips closest to the earth. It is a region of intense radiation through which Low Earth Orbit (where the approx altitude = 500 km) satellites must pass. The satellite's detectors are often turned off during the SAA and turned on again afterwards. The protons in the SAA, however, can activate the spacecraft and detector materials thereby creating a background noise count rate which remains even after the passage is complete. The SAA electrons only induce a background noise count rate actually during the SAA. Since the detectors are turned off during

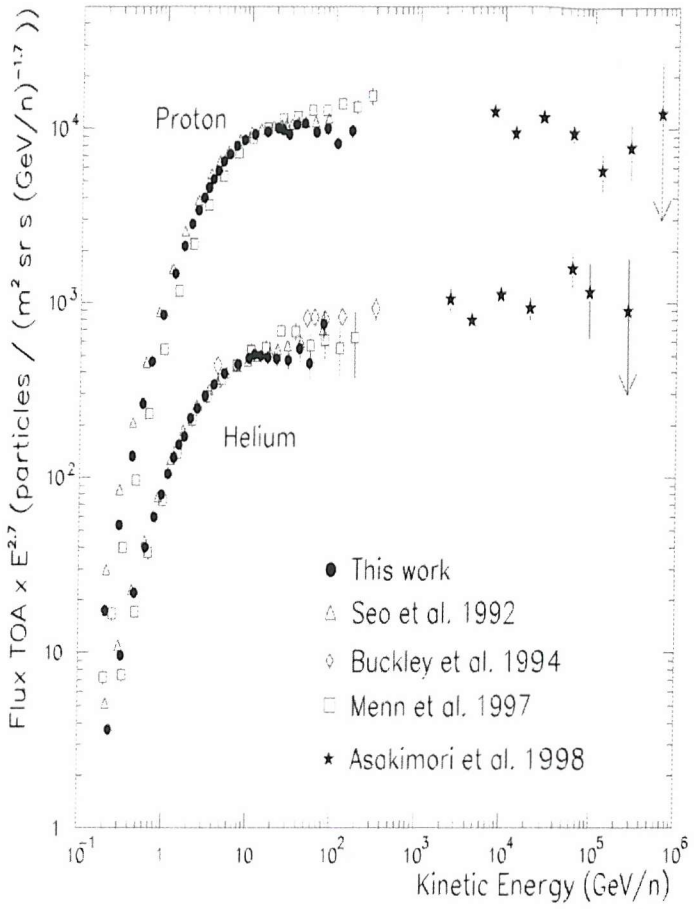

Figure 4.3: Cosmic ray proton spectrum [5] and references therein.

this time only the effects of the protons need to considered when modelling the SAA.

Figure 4.4 shows the proton flux contours of the SAA at an altitude of 500 km. At this altitude the duration of the satellite's orbit is ~90 minutes and the passage through the SAA is ~20 minutes. Thus for nearly 20% of the orbit the detectors are turned off. For the remainder of the time the orbit history must be used to estimate the background noise count rate due to recent passages through the SAA.

4.2.6 Locally produced γ-rays

Locally produced γ-rays are those which are produced in the spacecraft and detectors themselves. They arise through interactions of, for example, cosmic ray protons which "activate" the spacecraft/detector materials. The activated isotopes then decay by the emission of γ-rays. The flux of these γ-rays therefore depends on the size and mass of the spacecraft and detectors as well as from which materials they are made. There are several ways in which the γ-rays can be produced.

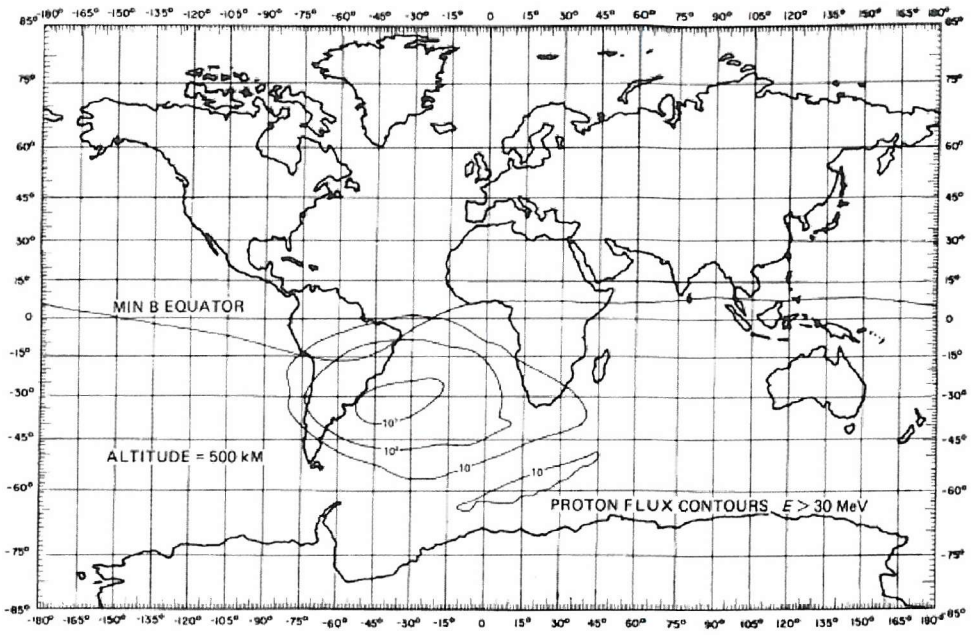

Figure 4.4: SAA proton flux contours [76]

Electron Capture

Electron capture occurs when an electron from one of the atomic shells is captured by the nucleus. A proton is tranformed to a neutron and the atomic number decreases by one but the atomic mass remains the same. A neutrino is emitted together with characteristic X-rays. The decay process is:

$$ {}^{A}_{Z}X + e^{-} \rightarrow {}^{A}_{Z-1}X' + \nu \tag{4.1} $$

where A is the atomic mass and Z is the atomic number. An example of electron capture and the γ-ray lines produced is shown on page 117.

Beta Decay

The nucleus can correct for an overabundance of either protons or neutrons by a simple conversion of a proton into a neutron or a neutron into a proton respectively. Negative β decay occurs when a neutron is converted into a proton with the emission of an electron and antineutrino. The decay process is

$$ {}^{A}_{Z}X \rightarrow {}^{A}_{Z+1}X' + e^{-} + \bar{\nu} \tag{4.2} $$

Positive β decay occurs when a proton is converted into a neutron with the emission of a positron and neutrino. The decay process is

$$ {}^{A}_{Z}X \rightarrow {}^{A}_{Z-1}X' + e^{+} + \nu \tag{4.3} $$

An example of β decay and the γ-ray lines produced is shown on page 117.

Isomeric Transition

An excited nucleus can decay to a lower excited state or ground state through the emission of a γ-ray photon. The emission of *gamma*-rays often follows α or β decay, as discussed above, and occurs extremely quickly ($\sim 10^{-9}$s). When an unstable nucleus emits γ-ray photons over a longer period of time, not subsequent to α or β decay, this is said to be an isomeric transition. The excited states are often called isomers or are said to be metastable. The isomer's atomic number and mass are unchanged by the isomeric transition.

Alpha Decay

Alpha particles (essentially helium nuclei) are tightly bound systems and can be emitted by unstable nuclei in order to lose energy. The decay process is

$$ {}^{A}_{Z}X \rightarrow {}^{A-4}_{Z-2}X' + {}^{4}_{2}He \tag{4.4} $$

The number of protons and the number of neutrons must be independently conserved. An example of α decay is

$$ {}^{226}_{88}Ra \rightarrow {}^{222}_{86}Ra + \alpha \tag{4.5} $$

where the half-life of ${}^{226}_{88}$Ra is 1600 years [35].

4.3 Techniques for the reduction of background noise

The background noise, although sometimes of astrophysical importance itself, can interfere with the actual data from the observed source. Thus it is common practice to guard against this background noise radiation using a variety of techniques. The most common of these is shielding which, in its simplest form, absorbs unwanted γ-rays (passive shielding). Active shielding not only absorbs unwanted γ-rays but also triggers background noise events such that background photons or charged particles which penetrate the shield are also discarded. A collimator works by restricting the field of view and therefore the number of unwanted off-axis γ-rays reaching the detector. Other techniques include detector segmentation and isotope enrichment.

4.3.1 Passive shielding

Passive shielding involves the use of a material to simply block unwanted γ-ray photons from entering the detector plane. High density materials, which are good at stopping γ-ray photons, are used to surround the detector for this purpose. The problem with this technique is that of fluorescence. Each material, when bombarded

by high energy photons, will emit characteristic x-rays. For low energy γ-ray detectors these photons are within the energy range of detection and they will therefore create additional background noise.

Graded shielding is often used to overcome the problems of fluorescence. Several materials are layered in descending order of Z, with the highest Z material on the outside. The energy of the fluorescent photons produced is dependent on the Z of the material. The higher the Z the higher the energy of the photons emitted. Thus the fluorescent photons produced by the outermost layer are absorbed by the next layer of material. The fluorescent photons subsequently produced by this layer are absorbed by its next layer. Usually 3 or 4 layers are used such that the innermost layer produces fluorescent photons of a low enough energy not to be detected by the detector material. Thus the background noise created by the shielding is reduced and the shielding becomes very effective at blocking unwanted γ-ray photons.

An example of graded shielding is used in the LEGRI (Low Energy Gamma Ray Imager) detector (see Chapters 6 and 7) where successive layers of lead, tantalum, tin and iron are used. The fluorescent photons produced by the iron are outside of the energy range of the detector plane and do not therefore create background noise counts. If lead were the sole shielding material, photons of $\sim$80 keV would be produced. These photons would be within the energy range of the detector plane and would therefore create a background noise count rate.

4.3.2 Active shielding

Passive shielding is very effective at blocking low energy γ-rays. At higher energies, however, the bulk of material required to completely stop the photons becomes excessive. In this case active shielding is required where it is not necessary to stop the photons but only for them to scatter within the shielding and deposit a detectable amount of energy. This acts as a trigger for the detector to reject subsequent events. Thus background γ-rays do reach the detector material but do not create a background noise count rate. This form of shielding is much more effective at higher energies when scattering is more likely (see figure 3.1).

Thus the shielding itself can be used to detect photons as well as to block them. The most commonly used material for active shielding is BGO - a scintillator with a high density.

Bismuth Germanate

The properties of bismuth germanate (BGO) compared to other inorganic scintillators are shown in table 3.2. It is not suitable as an actual detector since it has a low light yield (8200 photons / MeV compared to 52000 photons / MeV for CsI(Tl)) and would provide very poor energy resolution. Its high density (7.3 g/cm^3), however, is ideal for active shielding. In 1990 the GRAD (Gamma-Ray Advanced Detector)

Scintillator	Density g/cm^3	Refractive Index	Light Output % Anthracene[1]
Plastic (NE102)	1.032	1.581	65
Liquid (NE213)	0.874	1.508	78
Loaded Liquid (NE311)	0.91	1.411	65
[1] NaI(Tl) is 230% on this scale			

Table 4.1: Properties of some organic scintillator materials [34]

gamma-ray spectrometer was used to test the performance of BGO. The results indicated that BGO is at least as effective as CsI when used in active shielding [55].

The BGO is used in conjunction with a photomultiplier tube which detects the scintillation events of the background photons and sends a signal for the primary detector to reject any simulataneous events.

Organic scintillators

There are several different types of organic scintillators and these are summarised in table 4.1. Plastic scintillators are relatively inexpensive and easy to shape and mould. For this reason they are useful for large-volume solid scintillators. Liquid scintillators can provide almost 100% efficiency in counting low-level β activity, for example from ^{14}C. Liquid scintillation counting is a common technique whereby the sample to be counted is placed directly into the liquid scintillator. Loaded liquid scintillators are liquid scintillators with a high Z material added in order to increase their photopeak efficiency.

Figure 4.5 shows how active shielding may be used. The BGO on the sides and back of the detector, in conjunction with the photomultiplier tubes, block and detect unwanted background photons. The plastic scintillator is thin enough to allow γ-ray photons from the source to enter the detector plane but thick enough to detect unwanted charged particles.

4.3.3 Collimation

Collimation and shielding are closely related since they both act to reduce background noise in the γ-ray detectors. The collimator itself restricts the field of view of the detector such that off-axis rays are blocked. Thus only photons from the restricted field of view, ie those from the source, are detected.

A common configuration of a detector with shielding and collimation is shown in figure 4.6. The collimator is made of a passive material, for example tantalum, such that it absorbs the off-axis rays. As with passive shielding fluorescence from the collimator can cause a background noise count rate in the detectors. To overcome this some collimators are coated in a lower Z material, such as copper, to lower the energy of the fluorescence photons reaching the detector plane. Since the collimator

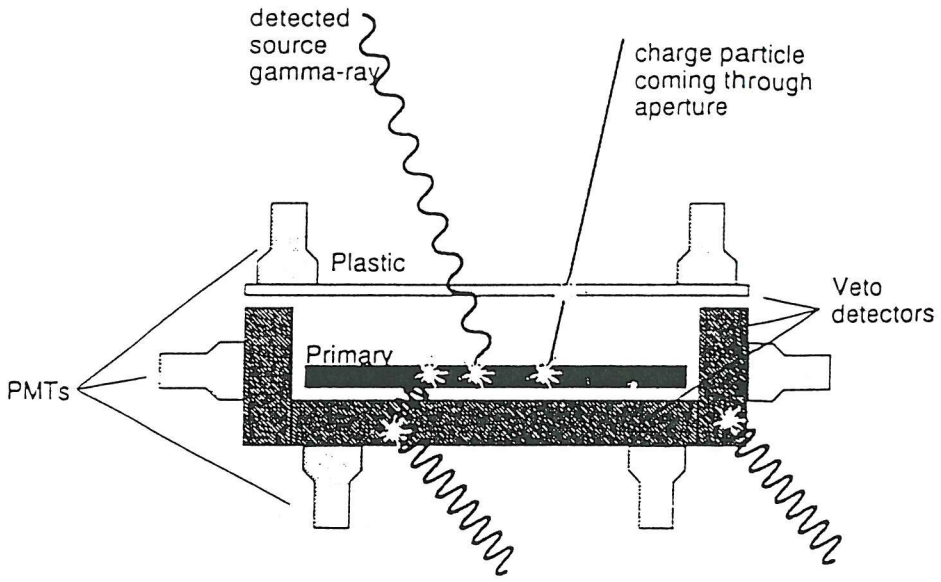

Figure 4.5: An illustration of active shielding. BGO surrounds the sides and back of the detector plane to block and detect unwanted γ-ray photons. A plastic scintillator is used in front of the detector plane to detect unwanted charged particles.

also restricts the field of view of the sky it can also be used as a basic imager which can detect the position of the source. Collimators can be used in conjunction with coded mask imaging systems (see section 3.4).

4.3.4 Further techniques

In addition to the usual shielding and collimation background reduction methods there are some additional techniques that can also be used. An example of this is detector segmentation. Germanium detectors are often segmented but the segmentation of other materials, for example CsI [56], has also been investigated.

The principle behind segmentation is that a γ-ray will invariably scatter in the detector whilst a background β-decay will deposit all of its energy locally. Much of the background noise at higher energies (150keV-1MeV) is due to localized β^- decays. Thus if several layers of, for example, germanium are used then a background event can be flagged as one which occurs in a single layer. Figure 4.7 shows a comparison of a true event and background event in a segmented detector.

At lower energies (<150 keV) only the top segment is effectively used ie only events which signal in the top segment and not in lower segments are "true".

The spectral line sensitivity of segmented n-type germanium detectors is improved by up to a factor of 2 in the energy range 40keV-1MeV compared to an unsegmented detector [18]. Thus in addition to shielding and/or collimation this is a very effective technique of reducing the background noise in a detector.

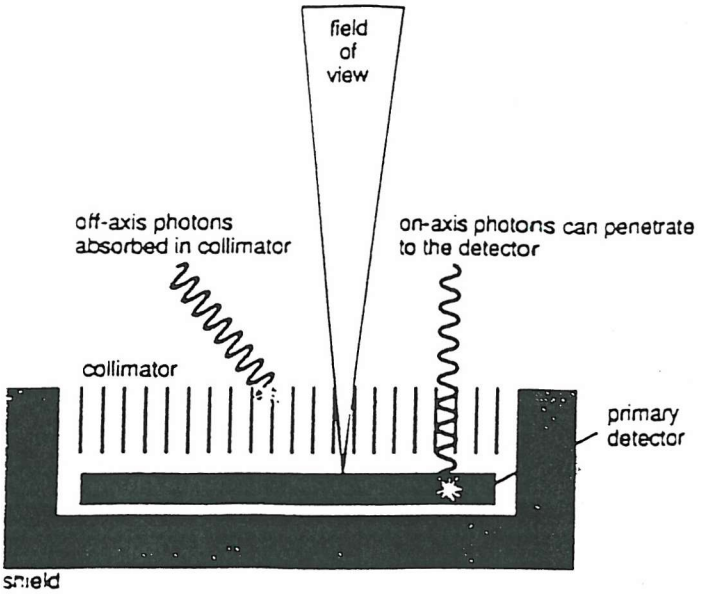

Figure 4.6: A detector system with shielding and collimation.

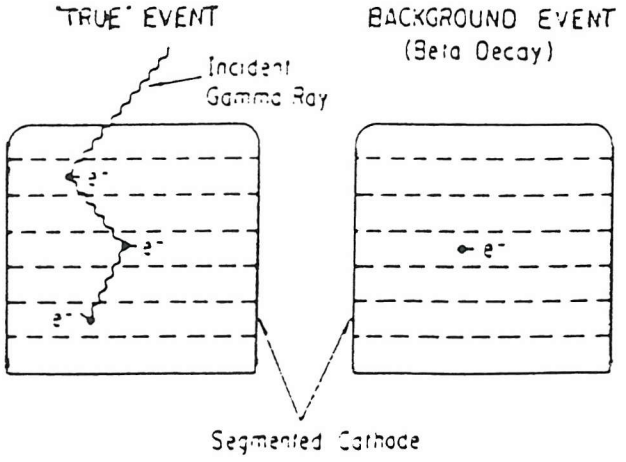

Figure 4.7: The interaction of a γ-ray in a multi-segment detector compared to a background event. The requirement of events in more than one layer eliminates the β decay but not the signal from the incident γ-ray [17].

Isotopic enrichment is also commonly used to reduce the background noise in germanium detectors. The ^{74}Ge isotope in a germanium detector could contribute up to half of the background noise continuum [2]. Thus reducing the amount of this isotope and replacing it with, for example, ^{70}Ge would improve the continuum sensitivity of the detector by up to a factor of 2 over the energy range 200-1000keV (the line sensitivity is improved by a factor of $\sim$1.4 [2]).

4.4 Background noise simulation software

Thus there are several different types of background noise which can affect the detectors onboard a γ-ray satellite. Shielding and collimation, discussed earlier, can help to reduce the background noise count rate but it would be an impossible task to design a satellite which guards against all background noise radiation. For this reason simulating the background noise has become an important process in designing, building and operating a γ-ray satellite. Not only are these simulations used to aid the analysis of data obtained by the detectors but also for pre-flight troubleshooting and future satellite design.

The background noise experienced by a γ-ray detector can be simulated using a specially designed particle physics simulation software suite called GGOD (Geant GCalor Orihet and Decay). The flow of information through the software suite is shown in figure 4.8.

Before the first Monte-Carlo simulation can be run, the radiation environment of the satellite and the satellite's detailed geometry must be known. The different types of background noise must each be simulated separately. Background noise induced by γ-ray photons require only one Monte-Carlo simulation. Hadronic background noise, however, requires two Monte-Carlo simulations in order to simulate the activation of the spacecraft and detectors themselves.

Thus for the Cosmic Diffuse and Atmospheric fluxes only the first stage of figure 4.8 (the GEANT software) is required. The radiation environment and detailed geometry are the input for the Monte-Carlo simulation and the output obtained is the hbook which includes the spectra induced in the detectors. From this the count rate can also be obtained.

The Cosmic Ray and SAA fluxes however require a more detailed process. The radiation environment and detailed geometry are again the input for the first Monte-Carlo. The output, however, includes not only a file containing the "prompt" spectra (that induced in the detectors immediately by the background radiation) but also information on the activated isotopes. This information is initially in the form of a set of files each containing isotope production rates. The satellite's exposure time to the radiation together with the "cooling" time (how long after the exposure time the spectra are to be obtained) are then used for the ORIHET

software (detailed as the prodrate and intorid programs in figure 4.9). This produces a set of files containing the isotope decay rates which act as the input for the second Monte-Carlo. Thus the spectra for a particular exposure time and cooling time are produced. In order to build up a profile of how the count rate decays with time after, for example a passage through the SAA, several cooling times are required. The ORIHET software and second Monte-Carlo must be run separately for each cooling time required.

This process is the basis of the work in Chapters 5-7. Within these chapters each stage of the process is tailored to the satellite and radiation environment being investigated.

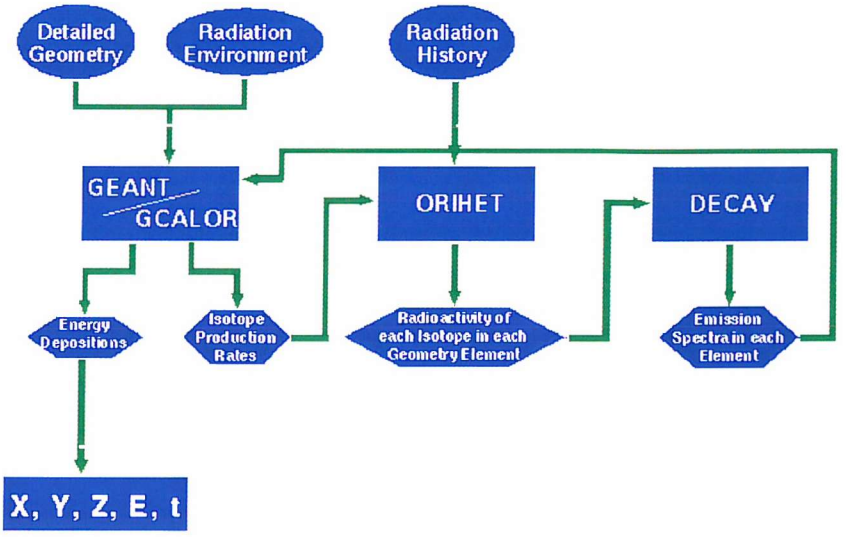

Figure 4.8: Flow diagram showing the flow of information through the GGOD software suite

4.5 Conclusion

A γ-ray satellite and its detectors may experience several different types of background noise. The background noise count rate can be lowered, through the use of shielding and collimation, or measured for example by using a coded mask. Simulating the background noise experienced by the detectors onboard satellites, however, is invaluable in ensuring the accuracy of the data and results produced. These simulations have become so useful that they can help in the design of future satellites by detailing which detector system designs perform better under certain conditions.

The next chapter illustrates the type of study which would be greatly enhanced by the use of background modelling to improve the sensitivity of the instruments. Chapters 6 and 7 discuss a model for the Low Energy Gamma Ray Imager (LEGRI) onboard the Minisat-01 satellite. These post-launch simulations are used to explore

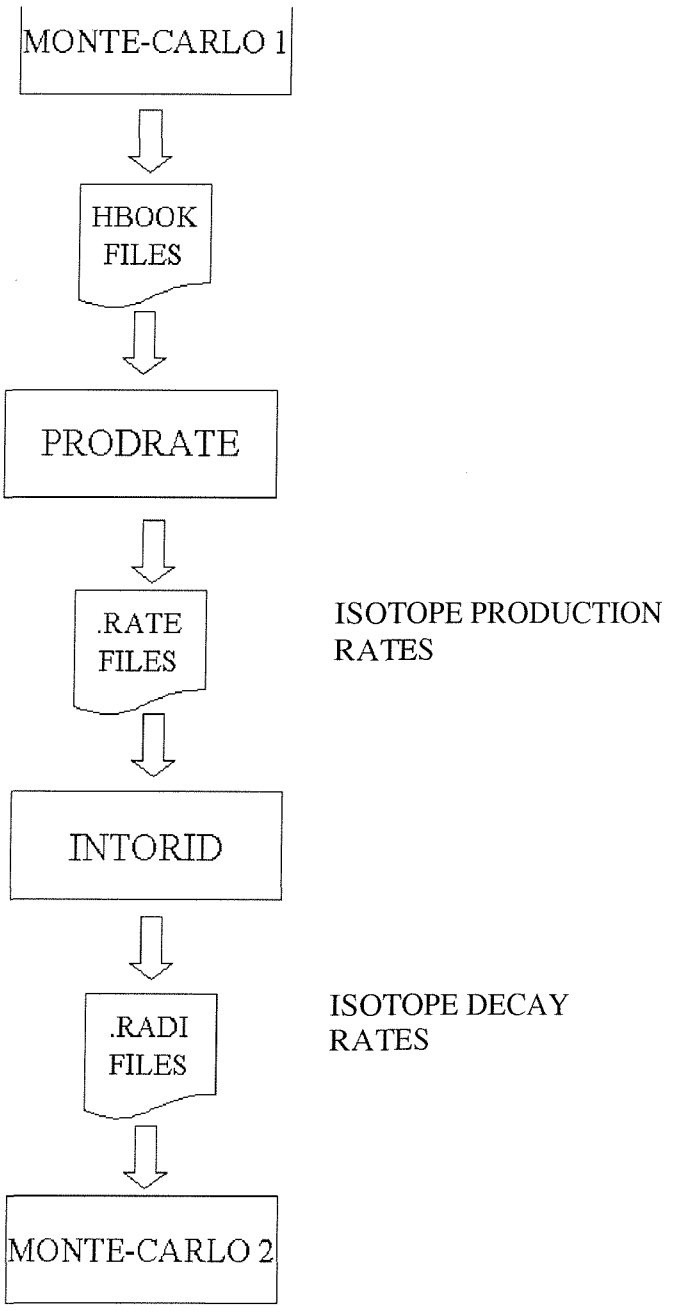

Figure 4.9: Flow diagram showing each Monte-Carlo simulation and the information produced at each stage

the background noise further by comparison to observations. The subsequent chapter is a pre-launch analysis of the background noise suffered during a solar flare by the instruments of the future INTEGRAL mission.

Chapter 5

The Analysis of Cataclysmic Variable stars using BATSE

5.1 Introduction

Monte Carlo simulations of the background noise in γ-ray satellites are used to improve sensitivity and allow fainter sources to be observed than would otherwise be achievable. This thesis focuses on the actual modelling of background noise in γ-ray satellites but it is also useful to illustrate why this modelling could be so important.

The basis of this chapter is the detection of x-rays in the energy range 20-100 keV from cataclysmic variable stars using the Burst and Transient Source Experiment (BATSE). Whilst these sources have been detected in the soft x-ray region they are believed to be only very faint emitters of hard x-rays as most have not been detected at energies above several keV. They form therefore an ideal sample to illustrate why improvements in sensitivity could be invaluable in hard x-ray / γ-ray astronomy.

5.2 Burst and Transient Source Experiment (BATSE)

BATSE was one of the four instruments on the Compton Gamma Ray Observatory (CGRO) as shown in figure 5.1. Also onboard were OSSE (Oriented Scintillation Spectrometer Experiment), EGRET (Energetic Gamma Ray Experiment Telescope) and COMPTEL (imaging Compton telescope). Further information on these instruments, which are not studied here, is given in [32], [33] and [57].

CGRO was launched in April 1991 on the Space Shuttle Atlantis STS-37 [21] and was designed to cover the hard x-ray and γ-ray regions from 15 keV to 30 GeV [20], [38] and [64]. The overall mission objectives are shown in table 5.1. The primary objective for BATSE was the detection, location and study of γ-ray bursts and for the duration of the mission BATSE detected these at a rate of $\sim$0.85 per

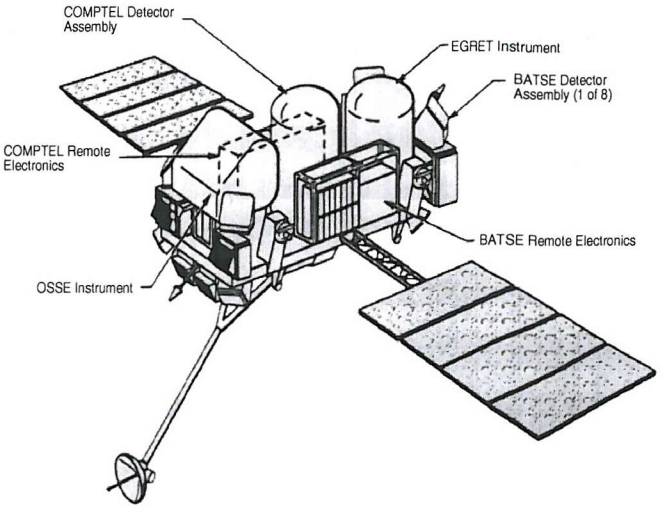

Figure 5.1: The CGRO satellite with its four instruments: BATSE, OSSE, EGRET and COMPTEL.

Source Type	Original Scientific Objectives
Gamma-Ray Bursts	Observation of gamma-ray bursts, their luminosity distribution, their spectral and temporal characteristics and their spatial distribution.
Discrete Objects	A study of discrete objects such as black holes, neutron stars and objects emitting only at gamma-ray energies.
Nucleosynthesis	A search for sites of nucleosynthesis - the fundamental process for building the heavy elements in nature - and other gamma-ray emitting lines in astrophysical processes.
Diffuse Lines	Map the distribution of diffuse 0.511 MeV and ^{26}Al gamma-ray line emission and determine its origin.
Galactic Emission	Exploration of the Galaxy in gamma rays in order to study the origin and dynamic pressure effects of the cosmic-ray gas and the structural features revealed through the interaction of the cosmic rays with the interstellar medium.
Extragalactic	A study of the nature of other galaxies as seen at gamma-ray wavelengths, with special emphasis on radio galaxies, Seyfert galaxies and QSOs.
Cosmology	A search for cosmological effects through observations of the diffuse gamma radiation and for possible primordial black hole emission.

Table 5.1: Summary of the CGRO objectives [21]

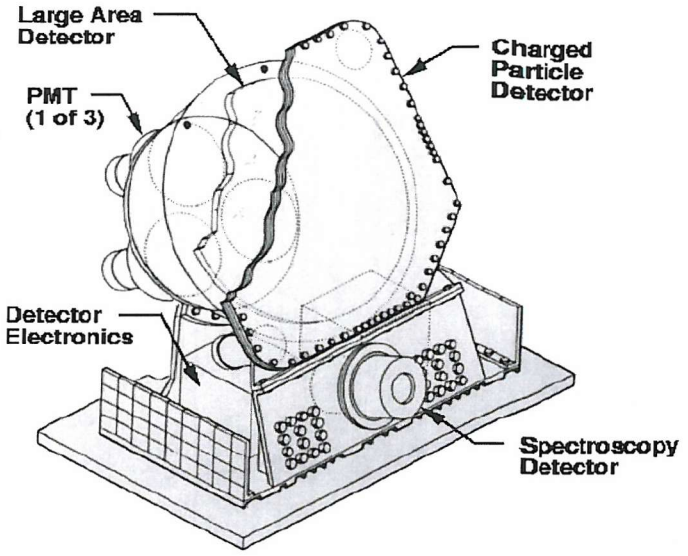

Figure 5.2: One module of BATSE

	Large Area	Spectroscopy
Material	NaI(Tl)	NaI(Tl)
Frontal Area	2025 cm^2	127 cm^2
Thickness	1.27 cm	7.62 cm
Energy Range	30-1900 keV	15keV-110 MeV
Energy Resol.	27% @ 88 keV	7.2% @ 662 keV

Table 5.2: Technical details of the BATSE detectors [16]

day. Furthermore BATSE's discovery that gamma-ray bursts are isotropic but non-homogeneous ruled out previous theories of a galactic disk distribution. Individual γ-ray bursts have also been shown to vastly differ in pulse structure and duration.

BATSE has a large field of view, enabling it to view all of the sky, together with high sensitivity in the low energy range. The instrument consists of 8 separate detector modules (shown in figure 5.2) positioned on the corners of the CGRO spacecraft. The Large Area Detectors (LAD), each containing a NaI crystal 50.8cm in diameter and 1.27cm thick, are optimised for sensitivity and directional response whilst the Spectroscopy Detectors (SD) contain NaI detectors 12.7cm in diameter and 7.62cm thick and are optimised for spectral coverage and resolution.

5.3 Cataclysmic Variable Stars

Cataclysmic variable stars (CVs) are binary star systems where the primary star is a white dwarf and the secondary star is a main sequence star expanding to fill its Roche Lobe. Mass transfer onto the white dwarf causes sudden, unpredictable eruptions. Figure 5.3 shows an artist's impression of a typical CV with the primary white dwarf star surrounded by an accretion disc of mass from the secondary. In this section each subtype of CV (Classical Novae, Dwarf Novae, Recurrent Novae and Nova-likes) is reviewed before turning to the BATSE Earth Occultation Analysis. Most of the material for the review of CVs comes from [70] unless otherwise stated.

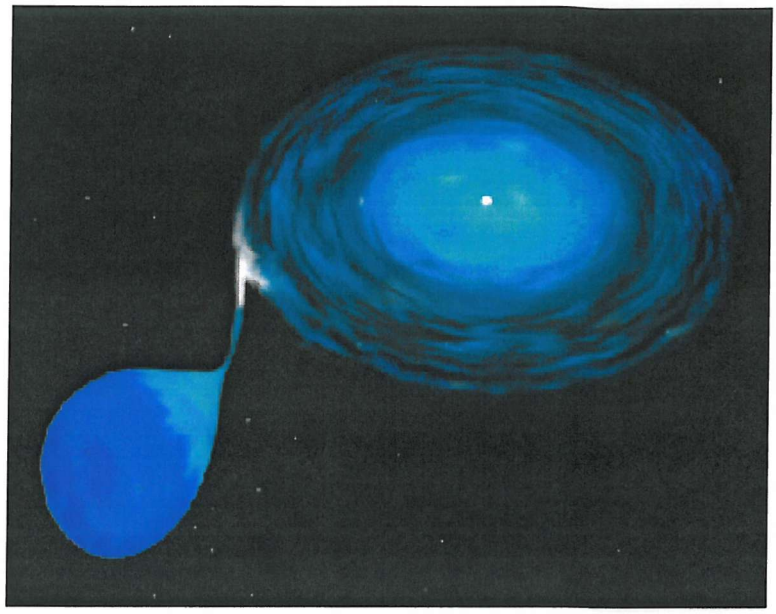

Figure 5.3: An artist's impression of a Cataclysmic Variable showing the primary white dwarf star surrounded by an accretion disc of mass from the secondary

5.3.1 Classical Novae

Classical novae have only one observed eruption but the range from prenova brightness to maximum brightness can be as high as 19 magnitudes. Fast novae, where the outburst and subsequent decline all occur in a period of days, show the greatest increase whereas slow novae have much smaller eruptions occuring on longer timescales.

A review of classical novae eruptions is given in [63] and [70]. At first the proton-proton chain (shown in equation 5.1-5.3) generates energy. The temperature at the base of the envelope around the white dwarf reaches $\sim 2 \times 10^7$K and the CNO cycle (shown in figure 5.4) begins to dominate. Convection takes fresh CNO to the core and β^+ decay nuclei to the surface where they deposit energy. This causes the expansion of the envelope and the luminosity of the eruption. An increase in temperature will lead to enhanced energy generation but not to an increase in pressure (since for degenerate matter, P $\propto \rho^\gamma$, which is independant of T) and the result is, therefore, an exponential runaway. Once the temperature reaches $\sim 8 \times 10^7$K (the Fermi temperature) the equation of state becomes that of a perfect gas and expansion occurs to reduce the temperature and prevent further nuclear burning.

$$p + p \rightarrow d + e^+ + \nu_e \tag{5.1}$$

$$d + p \rightarrow \gamma + {}^3He \tag{5.2}$$

$$^3He +^3 He \rightarrow p + p +^4 He \tag{5.3}$$

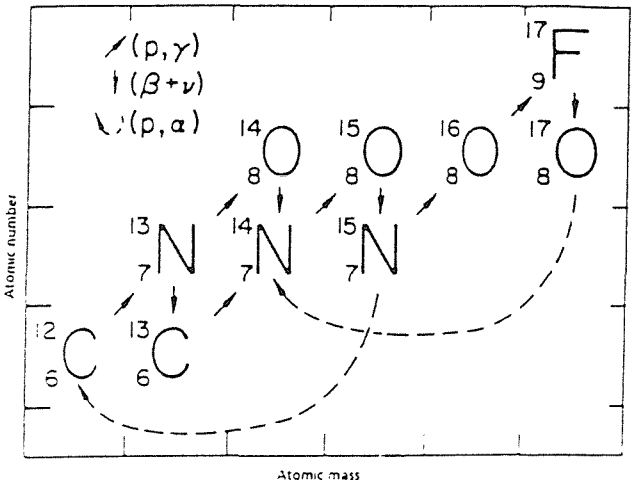

Figure 5.4: The CNO cycle begins once the temperature at the base of the envelope reaches $\sim 2\times10^7$K [70]

Novae emit soft x-rays when there is an abundance of CNO and consequently all of the proton captures of the CNO cycle occur before the envelope has chance to expand. This terminates the runaway and the β^+ unstable nuclei deposit $>10^{46}$erg in the envelope which is radiated away while the envelope is still only slowly expanding. Thus $\sim10^5 L_\odot$ is radiated through a small surface area and an effective temperature of $\sim10^6$K is generated leading to emission of approximately 0.5 keV ie soft x-rays. Harder x-rays and γ-rays are thought to come from positron-electron pair annihilation radiation during the early part of the outburst [41] though these fluxes have yet to be observed.

Fast novae produce the brightest eruptions which decay quickly over a period of days. The speed class of a nova was originally thought to be correlated to the enrichment of CNO but M_{WD} (mass of the white dwarf), L_{WD} (luminosity of the white dwarf) and $\dot{M}$ (rate of mass accretion onto white dwarf) are now believed to be the most important parameters [63]. The speed of a nova is often characterised by the time taken for the brightness to fall either 2 or 3 magnitudes below maximum (t_2 or t_3 respectively). Vel99 is an example of a fast nova ($t_2 = 6$ days) and Sco92 of a slow nova ($t_2 = 73$ days).

Novae oscillate between two quasi-equilibrium states. At high luminosity the envelope has a large radius containing a nuclear shell source which powers the luminosity. This state requires a minimum envelope mass below which nuclear

reactions cease. In the low luminosity state the envelope has a small radius and compressional heating replaces energy loss. This state can only exist below a maximum envelope mass above which nuclear reactions begin. Thus the nova changes from low to high luminosity due to an increase in the mass of the envelope and from high to low due to consumption of nuclear fuel and a decrease in the mass of the envelope. Stability can occur in the high state if the temperature of the white dwarf or the mass accretion rate are very high and steady nuclear burning occurs.

Figure 5.5 shows how the luminosity and visual magnitude of a nova progress over a complete cycle and figure 5.6 shows the corresponding changes in the structure of the envelope. The beginning of the cycle is arbitrarily set at the onset of the thermonuclear runaway and the whole cycle can be summarised in six stages [54]:

- Outburst: This represents the onset of the thermonuclear runaway. A shock wave carries energy to the edge of the envelope, bolometric and nuclear luminosities rapidly increase and the envelope expands.
- Expansion: The visual magnitude rises to a maximum whilst bolometric and nuclear luminosities decline. The radius increases to $\sim 100 R_{\odot}$, the outer shell containing $\sim \frac{1}{6}$th of the envelope mass expands as its velocity reaches 3800Km/s.
- Mass loss: Mass loss occurs by shock-ejection, continuous mass loss (optically thick wind) or nebular mass loss.
- Decline: The star has lost all of its accreted mass and the core is surrounded by the remnant envelope. The nuclear luminosity declines more rapidly than the bolometric luminosity as the nuclear energy souce is distinguished.
- Accretion: The luminosities decline further and new material is accreted.
- Convection: Fresh material and β^+ unstable nuclei are transported to the surface enabling new nuclear reactions.

5.3.2 Dwarf Novae

Dwarf novae have more than one observed eruption and the time between each can be from 10 days to 10s of years. Each outburst lasts from 2 to 20 days and is usually 2-5 magnitudes in brightness. There are three subtypes of dwarf novae: Z Cam stars (show protracted standstills just below maximum), SU UMa stars (occasional superoutbursts) and UGem stars (all other dwarf novae). The outburst mechanism is a release of gravitational energy due to a temporary increase in the mass transfer rate.

5.3.3 Recurrent Novae

Recurrent novae are classical novae that have more than one observed eruption. The difference between recurrent novae and dwarf novae can be seen in spectral observations as recurrent novae eject a substantial shell after the eruption but dwarf

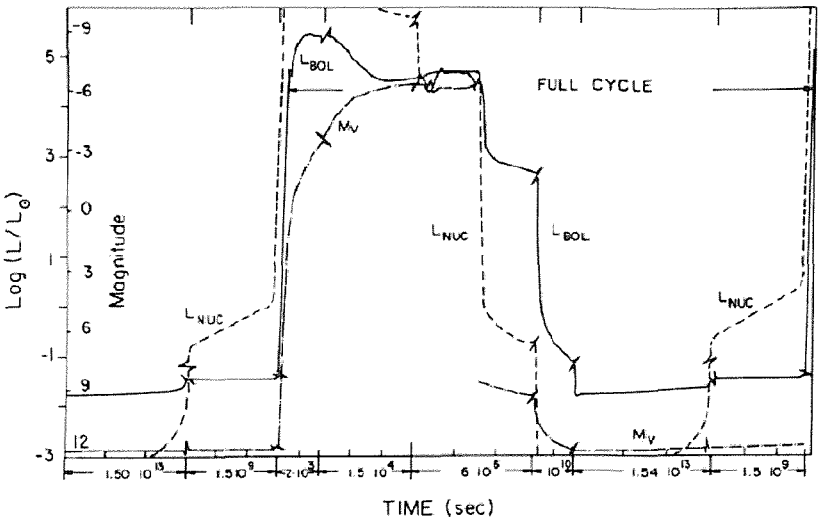

Figure 5.5: Evolution of bolometric luminosity (solid line), nuclear luminosity (dashed line) and visual magnitude (dot-dashed line) through a complete nova cycle and the accretion phase preceding it. The time axis is divided into intervals corresponding to phases of different evolutionary time scales [54].

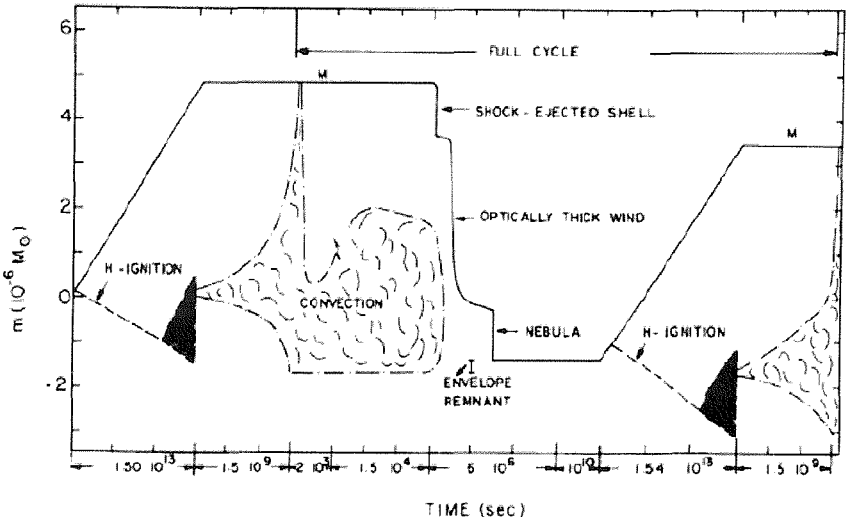

Figure 5.6: History of the structure of the envelope above the original white dwarf core (m>0) and below it (m<0). The solid line (labelled M) shows the total mass (M_{WD}+M) as a function of time. Dot-dashed lines show the boundaries of convection zones. Solid areas denote burning shells before the onset of convection [54].

novae do not. The outburst mechanism for recurrent novae is a thermonuclear runaway whilst for dwarf novae there is a release of gravitational energy due to a change in the mass transfer rate.

5.3.4 Nova-likes

This sub-class includes all non-eruptive cataclysmic variable stars, for example, pre-novae, post-novae and Z Cam stars which are effectively in permanent standstill. Magnetic CVs, also included in this class, are divided into polars and intermediate polars depending on the strength of the magnetic field of the primary star and the extent of the resulting disruption to the accretion disc.

Polars

The magnetic field surrounding the primary star of a polar is strong enough to control the flow of accretion and disrupt the formation of the accretion disc. Three polars have been observed at energies >2keV: AM Her, EF Eri and BY Cam. The hard x-ray spectrum of AM Her is shown in figure 5.7.

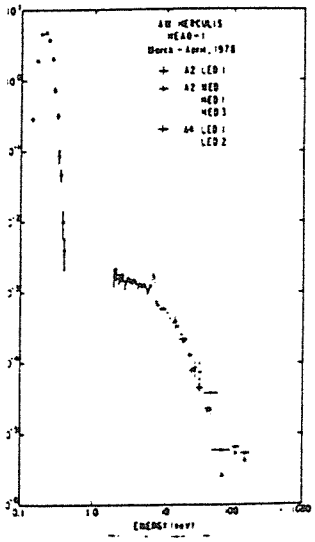

Figure 5.7: The x-ray spectrum of AM Her obtained by detectors on HEAO-1 [70]

Intermediate Polars

The magnetic field of intermediate polars is less powerful than that of polars and the accretion disc is only partially disrupted. Intermediate polars however are believed to be stronger emitters of hard x-rays due to their high mass transfer rates.

5.4 BATSE Earth Occultation Analysis of Classical Novae

5.4.1 Introduction

At the time of the outburst the thermonuclear runaway generates a temperature of $\sim 10^6$K [70] implying that novae are good emitters of soft x-rays. These emissions have been observed by various satellites including ROSAT [1]. Theoretical models predict hard x-ray emission to come from the Compton degradation of radioactive decay in particular due to the Comptonisation of photons emitted in the 511keV line [27]. Since BATSE operates in the energy range 20-100keV any detections made would allow confirmation of the continuum emissions and place constraints on theoretical models such as that mentioned above.

A preliminary search for hard x-ray emission prior to the visual outburst has been conducted using BATSE data by Hernanz et al (see below and [28]). Their sample, however, consists of only 8 randomly selected sources and a thorough search for hard x-rays from both before and during the outburst would extend and improve upon their research.

5.4.2 Earth Occultation Technique

An occultation of the target source by the Earth produces a step-like feature in the recorded data. This step is superposed on the background count rate induced in the detectors and on the count rates due to nearby bright sources. Each orbit produces a pair of rising/setting occultations. Thus BATSE's 90 minute orbit could produce up to 32 occultations of a hard x-ray source per day. By measuring the size of each step recorded a count rate history can be generated. The technique used here fits 1-2 minutes of the background count rate on either side of the occultation step and, since the time interval is very short, the background variation is assumed to be approximately linear [24]. All step measurements where there are known contaminating sources, occulting at the same time, are removed. When the source's elevation with respect to the orbital plane (β) is greater than about 70° the step feature is broadened [24]and this data is therefore removed also. Finally data from each of the 8 detectors are combined to give better statistics.

The sensitivity of BATSE could be improved further through the subtraction of a predicted background count rate before the standard occultation analysis (flat fielding). The BATSE background model is currently being developed at Southampton University to enable the BATSE data to be flat fielded. This model has not however been developed in time for this research and the standard occultation analysis described above has been used.

5.4.3 The γ-ray outburst

The sample, consisting of all classical novae from "A Catalogue and Atlas of Cataclysmic Variables - 2nd edition" [15], is shown in table 5.3. This is an improvement

on the Hernanz sample [28] which, to date, consisted only of 8 randomly selected sources (PUP91, SGR92/1, CYG92, SCO92, CAS93, AQL95, CIR95 and VEL99).

The γ-ray outburst is believed to occur just before the visual maximum [28] which is quoted as the outburst TJD (Truncated Julian Date) in table 5.3. The analysis is therefore extended to 30 days before the outburst TJD and to 10 days afterwards in one day sums.

Source	Outburst TJD	Right Ascension	Declination	Max mag
Sgr91	8470	273.5576	-32.2079	7.0v
Sct91	8515	281.7912	-8.3482	10.5v
Pup91	8617	122.9097	-35.125	6.4p
Sgr92/1	8665	272.3954	-25.8661	7.3
Cyg92	8671	307.6319	52.6308	4.2v
Sco92	8768	256.8224	-43.2561	7.3v
Sgr92/2	8812	275.8622	-28.3665	7.8p
Sgr92/3	8908	275.9222	-22.9913	8.0p
Aql93	9121	288.2783	1.5731	7.6p
Sgr93	9215	273.2075	-29.4846	7.7v
HY Lup93	9245	217.9591	-51.1758	8.0v
Cas93	9329	355.4467	57.5172	5.3v
Oph94	9505	263.9358	-19.3261	6.5p
Sgr94/2	9520	277.5962	-17.1991	10.8p
Cir95	9745	221.2228	-63.8987	7.2v
Aql95	9755	286.3607	-1.7009	8.2v
Cen95	9771	195.6332	-60.1939	7.2p

Table 5.3: The sample of classical novae taken from [15]. Visual magnitudes are given where known (symbolised by v) - otherwise the photographic magnitude is given (symbolised by p).

Some data on the resulting light curves, shown in figure 5.8, are missing due to corrupt data files, occultations where $\beta > 70°$ and occultations where an interferring source is occulting at the same time as the target source. The figure shows that BATSE data for each source do not reveal a significant flux, in the energy range 20keV-100keV, from the γ-ray outburst prior to the visual outburst.

The sensitivity of BATSE has been calculated using 3 years of observations of the Piccinotti AGN by [74]. In summary:

- 3σ - 3 years sensitivity: F_{picci}=2.2mCrab
- 3σ - 8 years sensitivity: F_{picci}=1.4mCrab
- 5σ - 3 years sensitivity: F_{picci}=3.7mCrab
- 5σ - 8 years sensitivity: F_{picci}=2.3mCrab

Classical novae are highly transient and the γ-ray emission is likely to last only a matter of days. Since emission in the energy band 20-100 keV has not been observed

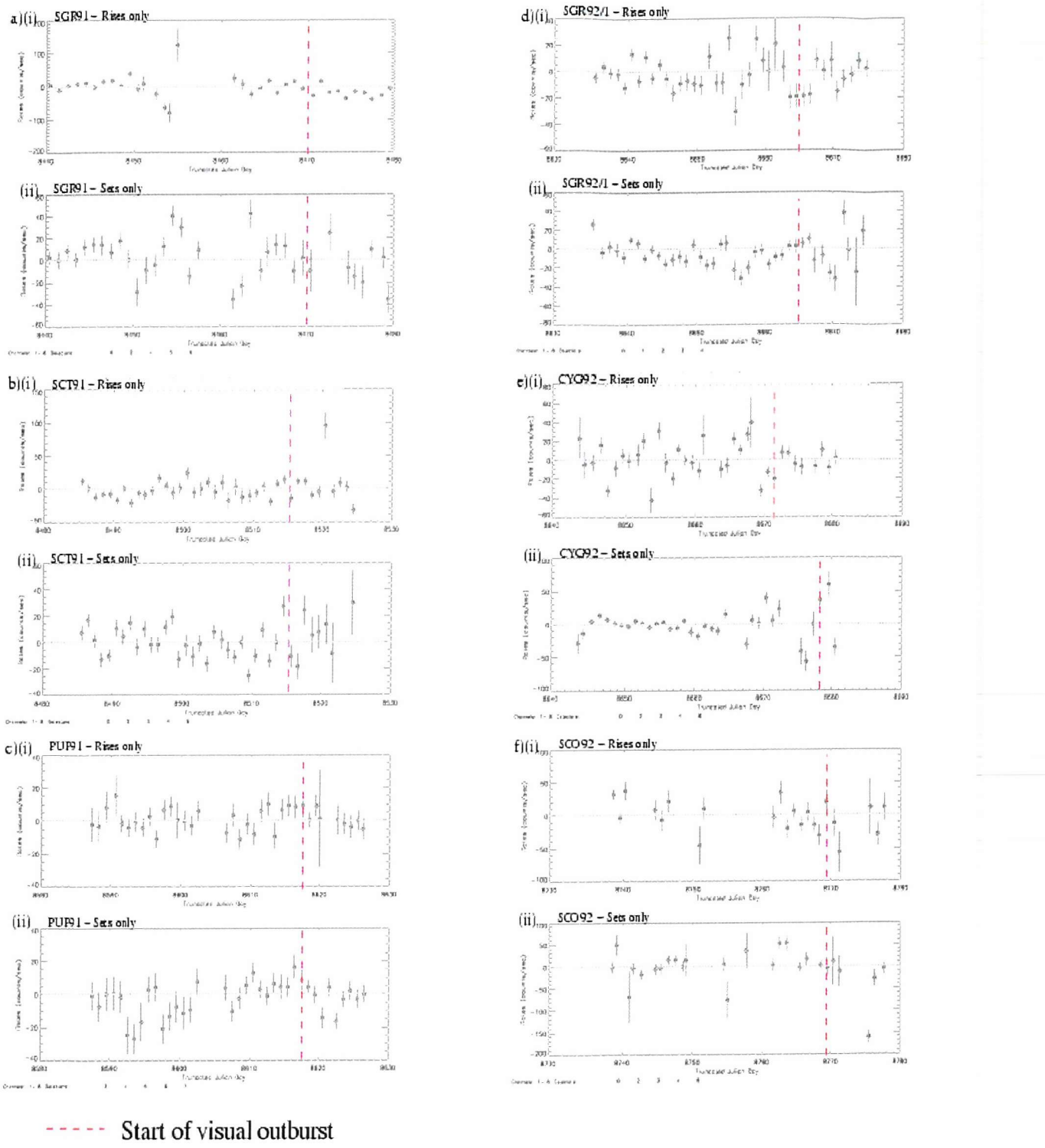

Figure 5.8: BATSE Earth Occultation data of a) SGR91 b) SCT91 c) PUP91 d) SGR92/1 e) CYG92 f) SCO92

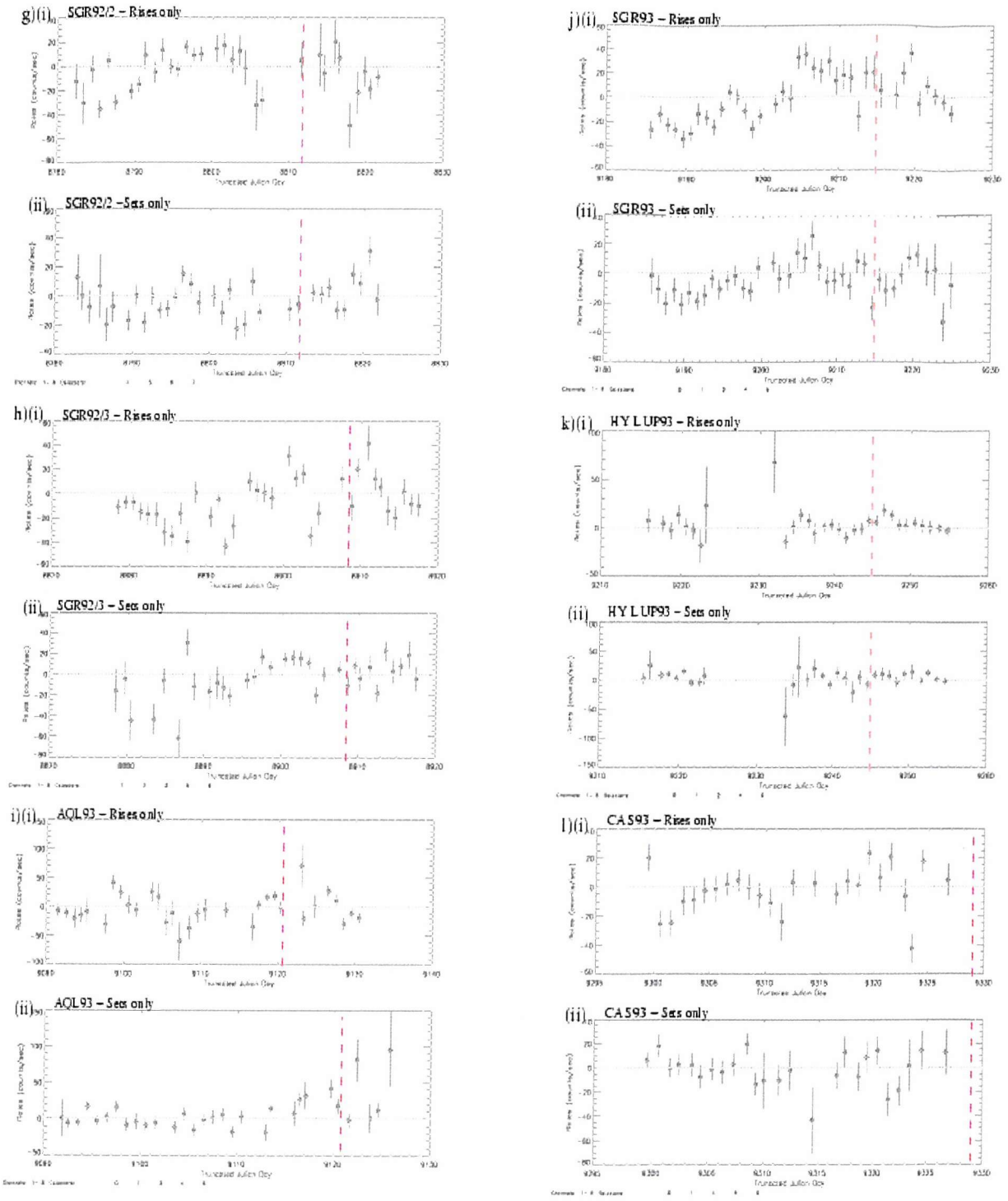

Figure 5.8: BATSE Earth Occultation data of g) SGR92/2 h) SGR92/3 i) AQL93 j) SGR93 k) HY LUP93 l) CAS93

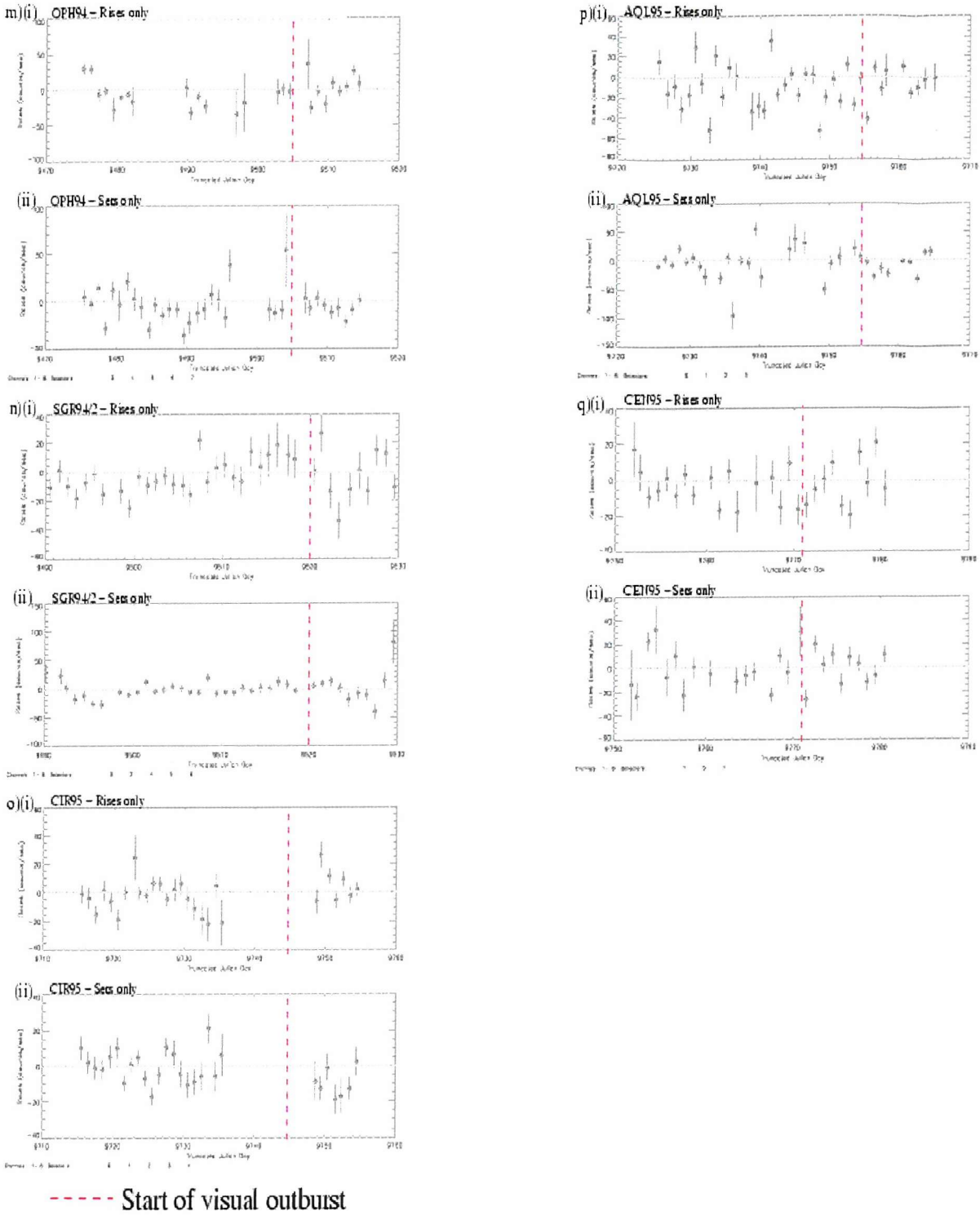

Figure 5.8: BATSE Earth Occultation data of m) OPH94 n) SGR94/2 o) CIR95 p) AQL95 q) CEN95

the length of observing time available is not known for certainty. For the sake of argument this has been taken to be 10 days in these calculations. Sensitivity $\propto \frac{1}{\sqrt{T}}$, so the sensitivity of BATSE to classical nova outbursts is:

- 3σ - 10 days sensitivity: F_{picci}= 23.0 mCrab (4.9×10^{-10} ergcm^{-2}s^{-1})
- 5σ - 10 days sensitivity: F_{picci}= 38.7 mCrab (8.2×10^{-10} ergcm^{-2}s^{-1})

If BATSE is likely to detect a 10 day γ-ray outburst from a classical nova then the outburst must be $>$ 23.0 mCrab for a 3σ detection or $>$ 38.7 mCrab for a 5σ detection. Figure 5.8 shows that BATSE did not make any significant detections from the sample chosen and each of the sources are therefore likely to be $<$ 23.0 mCrab (4.9×10^{-10} ergcm^{-2}s^{-1}) in the energy range 20-100keV. Cyg 92 is the brightest source in the sample and is at a distance of 1.7 kpc. An upper limit standardised to 1kpc would provide a useful figure for comparison to other sources. At 1kpc the 3σ upper limit of the flux of hard x-ray emission from Cyg 92 is 66.4 mCrab (since $F_d = \frac{F_0}{4\pi d^2}$).

5.4.4 The nova remnant

Observations of nova remnants have been seen at hard x-ray wavelengths, for example the x-ray light curve of Cyg 1992 shown in figure 5.9. The energy band of the ROSAT PSPC (Position Sensitive Proportional Counter) is much lower than that of BATSE (0.1-2.4 keV compared to 20-100 keV) and the x-ray emission is clearly seen to peak several hundred days after the visual outburst. It would be interesting therefore to study a similar period after the visual outburst with BATSE to see if the remnant emits harder x-rays also.

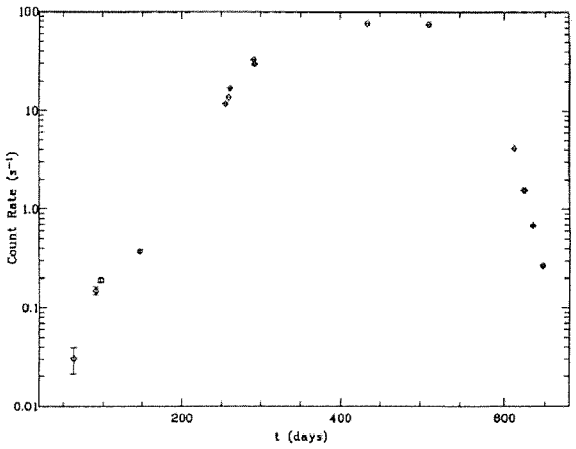

Figure 5.9: The X-ray light curve of the remnant of Cyg92 in the ROSAT PSPC 0.1-2.4 keV energy band [37]

The earth occultation technique described above was used to study BATSE data for evidence of hard x-ray emission from the nova remnants of the sample of classical novae detailed in table 5.3. A period of 800 days (in one day sums) was analysed

for each of the sources and the resulting hard x-ray light curve of the brightest, Cyg 1992, is shown in figure 5.10.

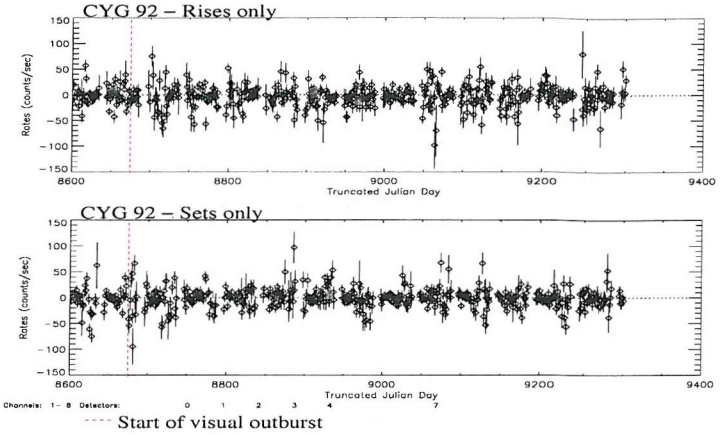

Figure 5.10: The X-ray light curve of the remnant of Cyg 1992 as seen by BATSE in the energy range 20-100 keV.

The BATSE data does not show significant hard x-ray emission from the nova remnant. Since a longer period of time has been used the sensitivity of BATSE will be better than for the detection of the γ-ray outburst and any sources >2.5 mCrab (5.3×10^{-11} ergcm^{-2}s^{-1}) are likely to give a 3σ detection. Since there are no significant indications of x-ray emission from the BATSE data the remnant of each of the novae studied is likely to be fainter than 2.5mCrab in the energy range 20-100keV.

5.5 BATSE Earth Occulation Analysis of other Cataclysmic Variables

In addition to Classical Novae other types of CV have also been analysed. The earth occultation analysis technique was used to gain x-ray light curves over a period of 500 days for the sources listed in table 5.4. Intermediate polars are believed to be stronger emitters of hard x-rays than polars [70] but magnetic CVs in general are likely to be good candidates for hard x-ray emission. A sample of 4 intermediate polars (labelled IP in the table) and 3 polars (labelled P in the table) has therefore been selected. Again the BATSE data did not show any significant flux. The sensitivity of BATSE indicates that these sources must therefore be fainter than 4.8 mCrab in the energy range 20-100keV.

5.6 Conclusions

A sample of classical novae have been analysed for γ-ray emission prior to the visual outburst. Classical novae have been studied in the hard x-ray range by Hernanz et

Source	Type of CV	Right Ascension	Declination
AM Her	P	274.0555	49.8678
BY Cam	P	85.7037	60.8588
AR UMa	P	168.936	42.9730
EX Hya	IP	193.1016	-29.2490
FO Aqr	IP	334.4809	-8.3512
GK Per	IP	52.7992	43.9046
AE Aqr	IP	310. 0381	-0.8708
DQ Her	IP	271.8760	45.8588

Table 5.4: The sample of Cataclysmic Variables (non Classical Novae). P = Polar, IP = Intermediate Polar, DN = Dwarf Nova

al [28] but ours is the first complete sample. The earth occultation technique was applied to BATSE data in the energy range 20-100keV. No significant fluxes were detected and an upper limit of 23 mCrab is therefore implied for a 10 day γ-ray outburst from these sources. The same technique was also applied for a longer period of time after the outburst to search for evidence of hard x-ray emission from the nova remnants. Again no significant fluxes were detected and an upper limit of 2.5 mCrab is therefore derived. Figure 5.11 shows the theoretical spectral evolution of a CO nova at a distance of 1 kpc compared to the sensitivity of BATSE for 10 days of data. Since BATSE's sensitivity for 10 days is much higher than the flux expected for 1 day no detections would, in fact, be expected. For detection of the higher flux available for up to 6 hrs after the outburst, the sensitivity would be increased (according to $\sqrt{T}$) and the sensitivity line in figure 5.11 would move up above the 6hr spectrum. If the sensitivity could be lowered (ie the sensitivity line in figure 5.11 lowered), for example through the subtraction of the background noise, then such theoretical models could either be confirmed or disgarded.

This work is, therefore, a perfect example of the type of study that background modelling is designed to enhance. No hard x-ray emissions can be detected from the sample using Earth Occultation Analysis alone but the improvement in sensitivity achieved through modelling the background noise and subsequently flat fielding the BATSE data could enable such faint emissions to be detected. Thus even after all the observations have been made and the data analysed there is still potential to keep on improving the sensitivity, detect emissions previously not seen and therefore confirm or disprove the theoretical models proposed. Future work in this area could include the flat fielding of these sources using BATSE data after the background model has been fully implemented (unfortunately scheduled for after completion of this thesis). Furthermore one of the objectives of INTEGRAL, due to be launched in 2002 (see chapter 8), is to search for classical novae at γ-ray energies [26].

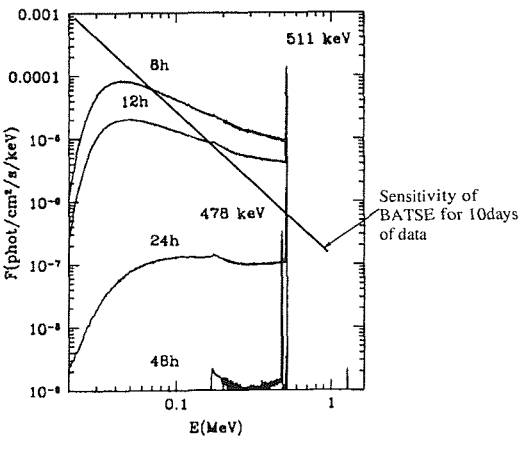

Figure 5.11: A theoretical spectrum for CO novae showing the BATSE sensitivity on 10 days of data being higher than the flux emitted for 24 hours. The theoretical spectrum is taken from [26].

Chapter 6

Analysis of the static background noise in LEGRI

6.1 Introduction

LEGRI (Low Energy Gamma Ray Imager) is one of three instruments on board the first Spanish MINISAT platform launched into a low earth orbit (600 km altitude) by a Pegasus rocket in April 1997. Of the other two instruments, EURD studies the background radiation in the extreme ultra-violet and CPLM is a study of micro-gravity conditions.

The technological objectives of LEGRI included a feasibility study of mercuric iodide detectors (HgI_2) in the low energy range (10-100 keV). As discussed in Chapter 3, HgI_2 is a room temperature semiconductor detector. Its higher Z and higher density (see table 3.1) than CdTe, Ge and Si allow for better efficiency at a given thickness. The energy required per electron-hole pair in HgI_2 is less than in CdTe so the energy resolution should be better. Ge and Si require even less energy per electron-hole pair but they require cooling which is often inconvenient and costly. Thus HgI_2 is a very interesting alternative semiconductor material. There are several problems however and these include:

- Severe charge trapping in crystals more than $\sim$ 1mm thick worsens the energy resolution. HgI_2 is therefore more useful at lower energies ($\sim$ 20 keV) when the interaction is near the cathode and the holes have less distance to travel.
- The buildup of charges due to the charge trapping can cause the electric field to become distorted thereby further reducing the charge collection.
- Exposure of the crystal to air for weeks or months can cause the surface to deteriorate and the material must therefore be encapsulated.

Much research has therefore been invested into this material and its viability for ground and spacecraft detectors. Crystals of HgI_2 were first grown in the 1970s.

Early versions were grown from solution but it was later discovered that using vapour growth gives better charge collection and thus better energy resolution [75].

During the 1980s advances were made in the fabrication of the crystal and research also began to look into its durability and longevity. Iwanczyk [30] discovered that although there was no evidence of internal degradation of the material over a period of 7 years, HgI_2 alone was not suitable for long term operation in vacuum conditions. The crystals must be coated in either acrylic or Parylene. Longevity tests by Iwanczyk et al [31] showed excellent durability for Parylene coated HgI_2 exposed to two years of severe conditions. A sample of detectors were subjected to intense proton irradiation and found to show good resistance to damage [31]. Iwanczyk [30] also developed the possibility of using HgI_2 in an array of crystals offering the benefits of spatial resolution, large active areas and high count rate capabilities.

Gerrish et al [22] discovered that impurities in the original material used during vapour growth could increase the effects of hole trapping. Attempts to produce crystals with better energy resolution lead researchers to purification of the starting materials obtained from commercial vendors. Different amounts of impurities were present in the crystals however and this lead to inconsistencies in the resulting detectors. Some researchers therefore made their own HgI_2 from potassium iodide and mercuric chloride [68].

Further development of this material was required and LEGRI was proposed as a technological mission with the following objectives:

- Viability of using HgI_2 in γ-ray detectors on astronomy space missions
- Test the durability and longevity of HgI_2 under space conditions
- Deepen the general understanding of HgI_2 technology

The scientific objectives for LEGRI were:

- Spectral studies of strong γ-ray sources
- A study of γ-ray extragalactic astronomy.
- The location of new strong γ-ray sources (such as those described in Chapter 2)

The sensitivity of LEGRI with potential target sources is shown in figure 6.1.

The Minisat-01 platform is shown in figure 6.2. LEGRI was based on a coded mask system with a fully coded field of view of 11 degrees and an angular resolution of 2 degrees. The detector was originally designed as a 10 by 10 array of HgI_2 elements. The problems of crystal fabrication, however, lead to crystals of inconsistent size and quality. Ground testing exposed the poor imaging capabilities of the HgI_2 and it was decided to replace some of the HgI_2 pixels with CdZnTe. The final composition was therefore an 8 by 10 array of HgI_2 with 20 1 cm^2 CdZnTe. The

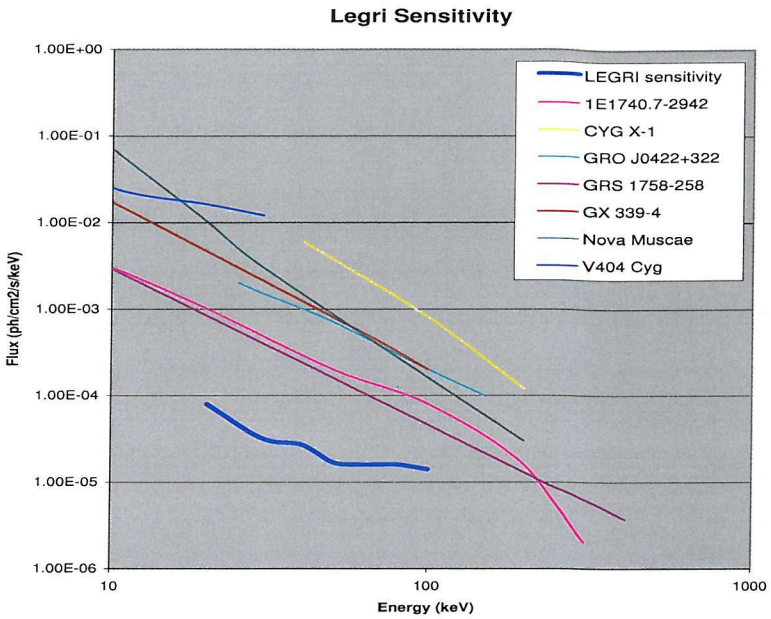

Figure 6.1: The sensitivity of LEGRI with several potential target sources

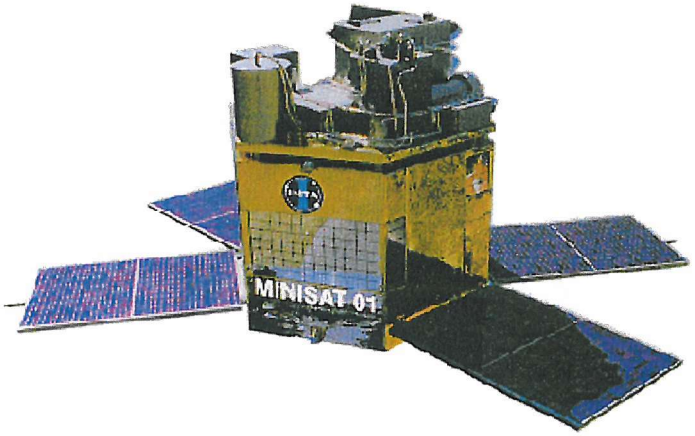

Figure 6.2: Minisat-01

collimator was made of 11 horizontal and vertical tantalum slats. Surrounding the whole detector was a passive shield of lead, tantalum, tin and iron. The mask unit consisted of a coded aperture mask made from tungsten elements on a honeycomb plate. The star sensor was used to determine the attitude of the satellite.

An analysis of the background noise in LEGRI will allow a better understanding of the causes of background noise in satellites and enable more sensitive instruments to be designed in the future. It is an ideal test case due to its simplicity and the complete access to observational data, both scientific and orbital. The ability to schedule specific background obervations allows a direct comparison between these and background simulation results.

6.2 Effect of latitude on LEGRI observed in-flight background

The intensity of the sources of background noise dependent on cosmic rays varies with latitude (see Chapter 4). An orbit history for the spacecraft is therefore vital to be able to analyse observational data for the different components of background noise. Figure 6.3 shows an orbit plot for one day (DOY 220 1997) where there is an SAA pass and the spacecraft reaches its extremes of latitude (+/- 28^0). LEGRI's orbit is 90 minutes and each path in figure 6.3 represents the time for which LEGRI is turned on during one particular orbit. The orbit precesses and so every day will have a different plot. DOY 220 1997 was chosen in particular since LEGRI was not observing any particular astronomical source and the count rates seen should be due solely to the background noise and the sum of any weak sources in the FOV.

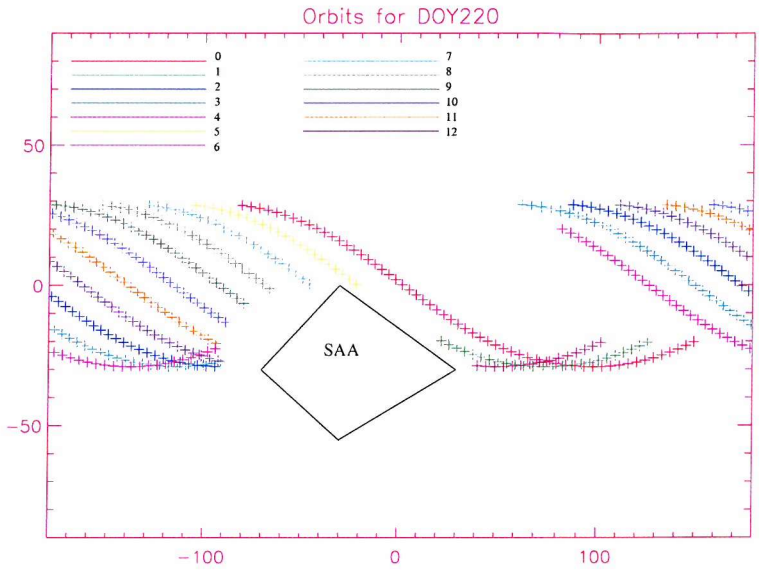

Figure 6.3: Orbit paths for DOY 220 1997. Legri travels from right to left. One of the only windows unaffected by the SAA is therefore window 0.

For each path there is a corresponding "window" of data when LEGRI is taking data. During eclipse EURD operates and LEGRI does not. The orbital position of LEGRI can be matched to the count rates received by matching the paths on the orbit plot to the corresponding "window" of data. This is useful in analysing the effect of geomagnetic cut-off ie latitude on the count rates.

Observations of the count rates in the HgI_2 rows (see figure 6.4) show very narrow peaks with no physical origin which implies an unstable detector response due to the inconsistencies in the quality of the pixels [52]. Such unstable behaviour was seen both pre-launch and throughout flight, making analysis of the detector data virtually impossible. Future observations and simulations therefore consider only the CdZnTe pixels which had better stability.

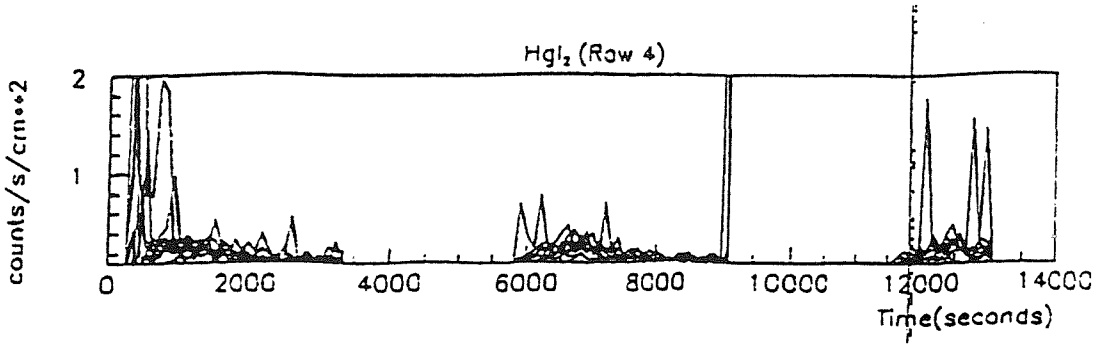

Figure 6.4: Counts v time for one row of HgI_2 showing detector instability [52].

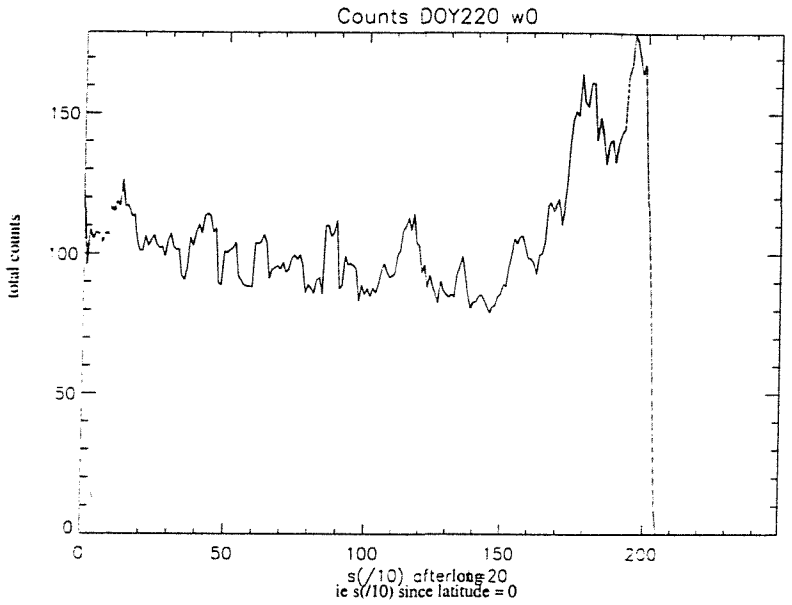

Figure 6.5: Counts v time for DOY 220 window 0. There is no SAA pass and the effect of geomagnetic cut off can be seen as an increase in the count rate from 0.5 $c/cm^2/s$ to 0.75 $c/cm^2/s$.

Window 0 in figure 6.3 is not affected by the South Atlantic Anomaly (SAA) but the satellite passes from minimum to maximum latitude thereby exposing LEGRI to the full effects of geomagnetic cut-off. The effects due to the SAA will be discussed further in Chapter 7. Figure 6.5 shows how the count rate increases in this window from 0.5 $c/cm^2/s$ to 0.75 $c/cm^2/s$ as the latitude increases from 0^0 to 28^0. "Total counts" in figure 6.5 represents total counts over all of the 20 CdZnTe pixels and 10 second time bins. Total count rates of 100 or 150 therefore correspond to 0.5 $counts/cm^2/second$ and 0.75 $counts/cm^2/second$ respectively.

Figure 6.5 shows a distinct periodicity. This is due to the instability of the detectors below channel 900. Figure 6.6 shows only channels below 900 in window 12 of DOY220 and figure 6.7 shows all channels for this window. The accentuation of the periodicity in figure 6.6 indicates that it is primarily caused by the lower energy channels where the detector response is unstable. All future work should

consider only channels > 900 to avoid this effect.

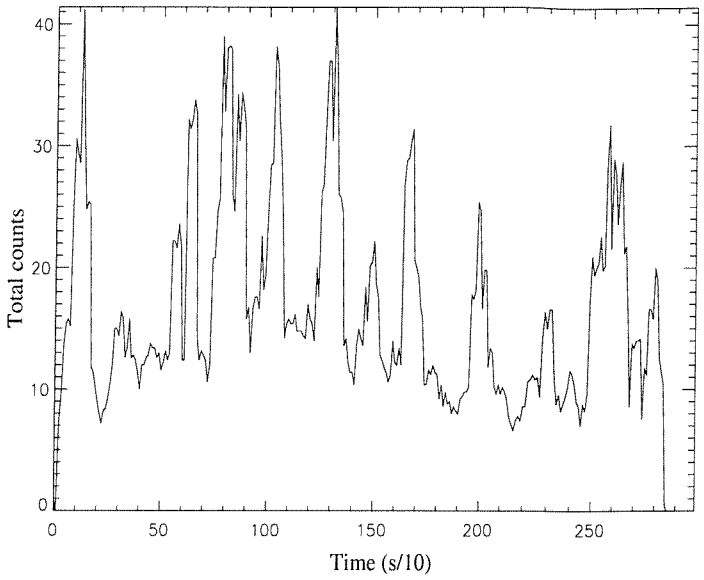

Figure 6.6: DOY 220 window 12 showing only channels < 900 and the resulting extreme periodicity

So far only a select few days have been analysed. The count rates for randomly selected days between DOY 246 1997 and DOY 90 1998 are shown in table 6.1. The sample size is restricted to those days not pointing at astronomical sources. The average count rate over this period was 0.68 $c/cm^2/s$. The count rate for each window was different and there are three main reasons for this:

- Different latitudes may be attained during different windows and varying degrees of geomagnetic cutoff may therefore have been experienced.
- The pointing of the detector may have been different implying a different mix of cosmic diffuse and atmospheric.
- The orbital history of the spacecraft may have been different for each window and irradiation of the spacecraft due to the SAA may have increased the count rate in some windows more than in others.

There does not seem to be any long term trend and the count rate would appear to be approximately constant. This implies that there is not an accumulation of activated isotopes, over the sampled period of six months, and that the background noise does not increase with time. This agrees with the observations shown in figure 6.8.

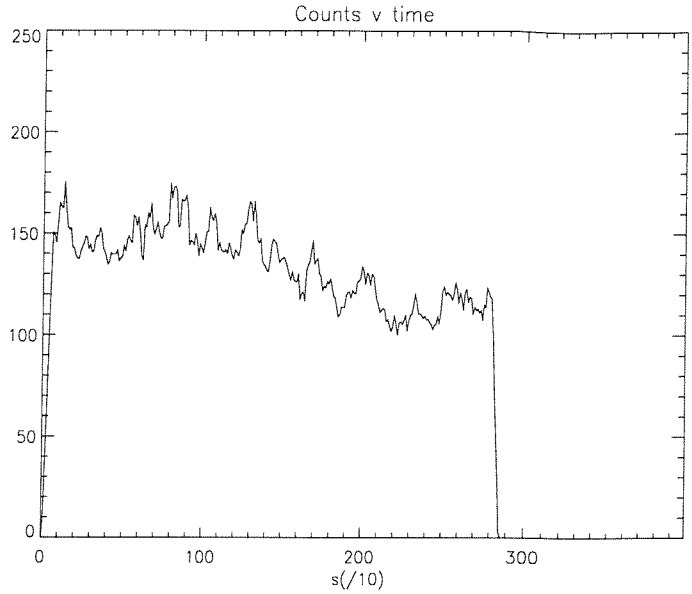

Figure 6.7: DOY 220 window 12, all channels

Day	Window	c/cm^2/s
246 1997	1	0.60
250 1997	0	0.62
260 1997	3	0.72
342 1997	7	0.70
354 1997	4	0.75
12 1998	9	0.74
18 1998	6	0.64
89 1998	1	0.63
94 1998	4	0.72

Table 6.1: Background noise count rates over a period of 200 days

6.3 Monte-Carlo simulations of the LEGRI background noise

6.3.1 Introduction

The previous section shows the effect of latitude on the observed count rates of LEGRI. These results can be used for verification of simulations of the background noise by comparing observed and simulated count rates. The simulations can then be used for further analysis of the background noise. The targets of this section are therefore to:

- build a "GGOD model" of LEGRI to describe the geometry and materials of the spacecraft (see chapter 4 for explanations of GGOD and GEANT)
- define the radiation environment for LEGRI through a break down of the background components

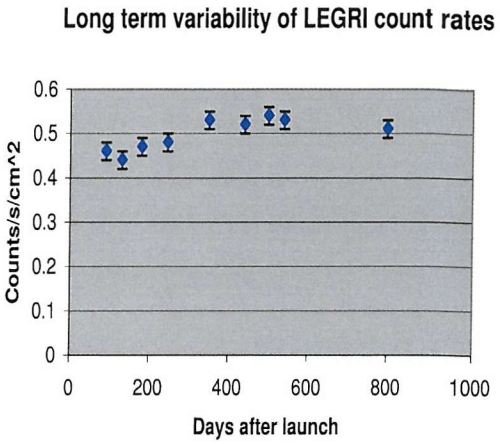

Figure 6.8: Long term observational background counting rates in LEGRI (private communication with University of Valencia)

- generate simulated count rates of the static background noise (ie excluding any effects of the SAA)
- compare simulated and observed count rates at the equator and the poles
- analysis of LEGRI's static background noise using simulated spectra and count rates

6.3.2 Detailed Geometry of the "GGOD model"

The LEGRI mass model was constructed using GEANT 3. Figure 6.9 shows a drawing from INTA of the MINISAT platform. Figure 6.10 shows the top view of the model of the platform.

Each of the units has been modelled as listed:

- Coded Mask: Tungsten pixels form the coded mask pattern. There is a thin layer of carbon fibre on one side of the mask and the whole structure is supported by two aluminium blocks.
- Detector shielding: The four layers of shielding are lead (2mm thick), tantalum (0.25mm), tin (0.5mm) and iron (1mm). These surround the detector on three sides leaving an open window for the detector plane. Within this there is an aluminium box which is 2mm thick on three sides and 50μm thick in front of the detector plane. The central part of the detector behind the detector plane is filled with an electronics mix.

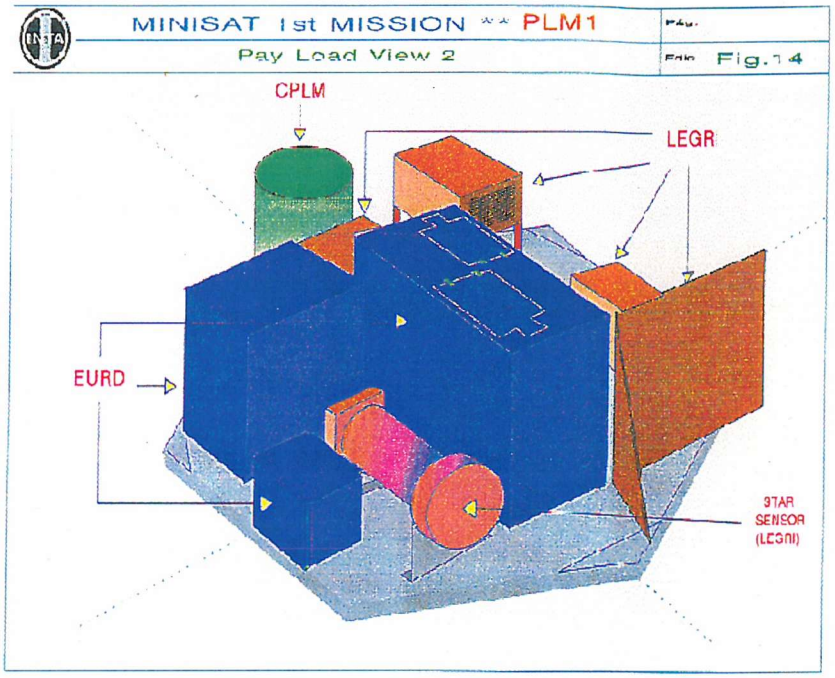

Figure 6.9: Drawing of the Minisat platform (INTA).

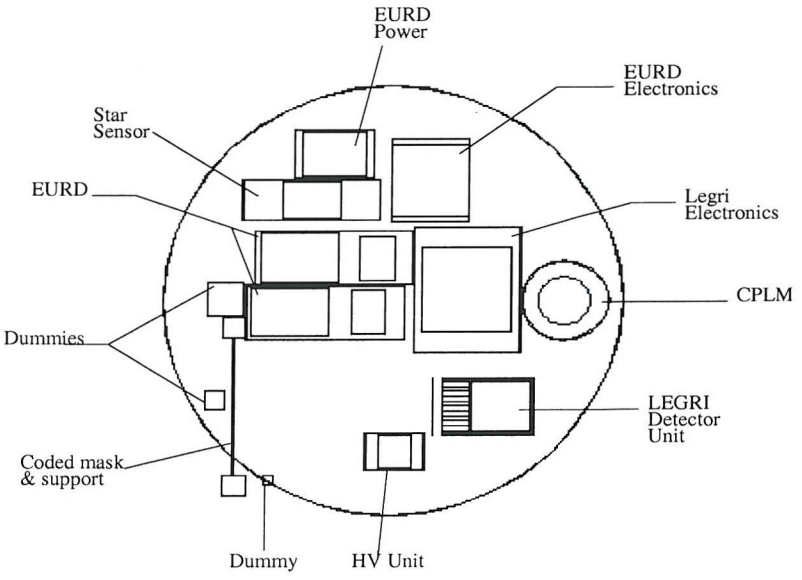

Figure 6.10: Top view of the Geant model of the platform.

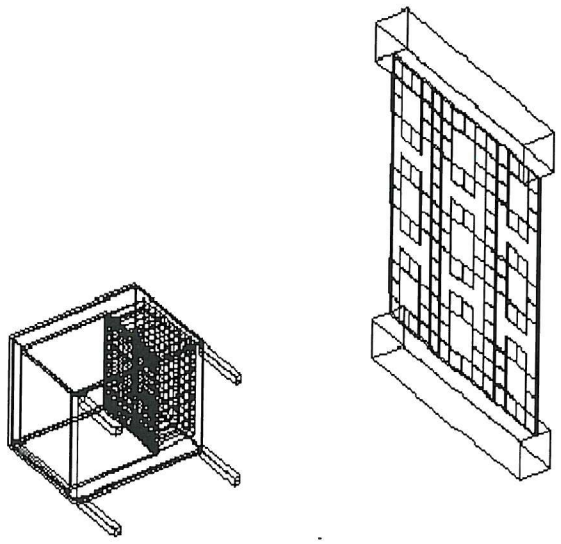

Figure 6.11: The LEGRI detector and coded mask system

- Collimator: Eleven horizontal and vertical tantalum slats (each 0.25mm thick) placed in front of the aluminium window and detector plane.
- Detector Plane: Two rows of 10 cadmium zinc telluride ($Cd_{0.8}Zn_{0.2}Te$) pixels each 2mm thick and 10mm square. These two rows are separated by an array of 8 by 10 HgI_2 pixels. Since these are all of different sizes the model simply includes 8 non-sensitive strips of HgI_2 each corresponding to the total mass of the pixels in that row. All pixels and strips are fixed onto a carbon fibre layer.
- Legs: The detector sits on 4 aluminium legs.

The above lists the most important components of the spacecraft on the basis that these are the closest and are therefore more likely to give rise to counts in the detector plane. These components are therefore modelled to a high degree of accuracy since simplifying them even a little could impair the simulated count rates and spectra. Figure 6.11 shows the detail of the coded mask system.

The following units are far enough away from the detector plane and/or are small enough that they *can* be greatly simplified. In most cases a thin (2mm) aluminium shell encompasses an "electronics mix" such that the total mass of the unit matches that detailed in the Instrument Definition Document.

- EURD Power Supply (1.55 kg), EURD electronics (6.5kg), Star sensor (2.5kg), CPLM (3.6kg), HV Unit (0.3kg), LEGRI electronics (5.0kg): Aluminium shell encompassing an electronics mix (carbon, copper, silicon and aluminium of total density 1.0 gcm^{-3}).
- EURD (2×10.75kg): Aluminium shell. Remainder made up equally of an electronics mix and silicon dioxide which represents the glass diffraction grating.

- Dummies × 3 (2.5kg, 1.8kg, 0.2kg): Each made of tungsten.

6.3.3 Radiation environment and Monte-Carlo simulations of its components

For a general description of the different types of background noise see Chapter 4. The cosmic diffuse, atmospheric, cosmic ray and SAA fluxes constitute the radiation environment for LEGRI and are shown in figure 6.12. All of the components are modelled using a power law spectrum except the SAA which is modelled using a monochromatic beam of 100 MeV protons. SAA simulations are discussed in Chapter 7.

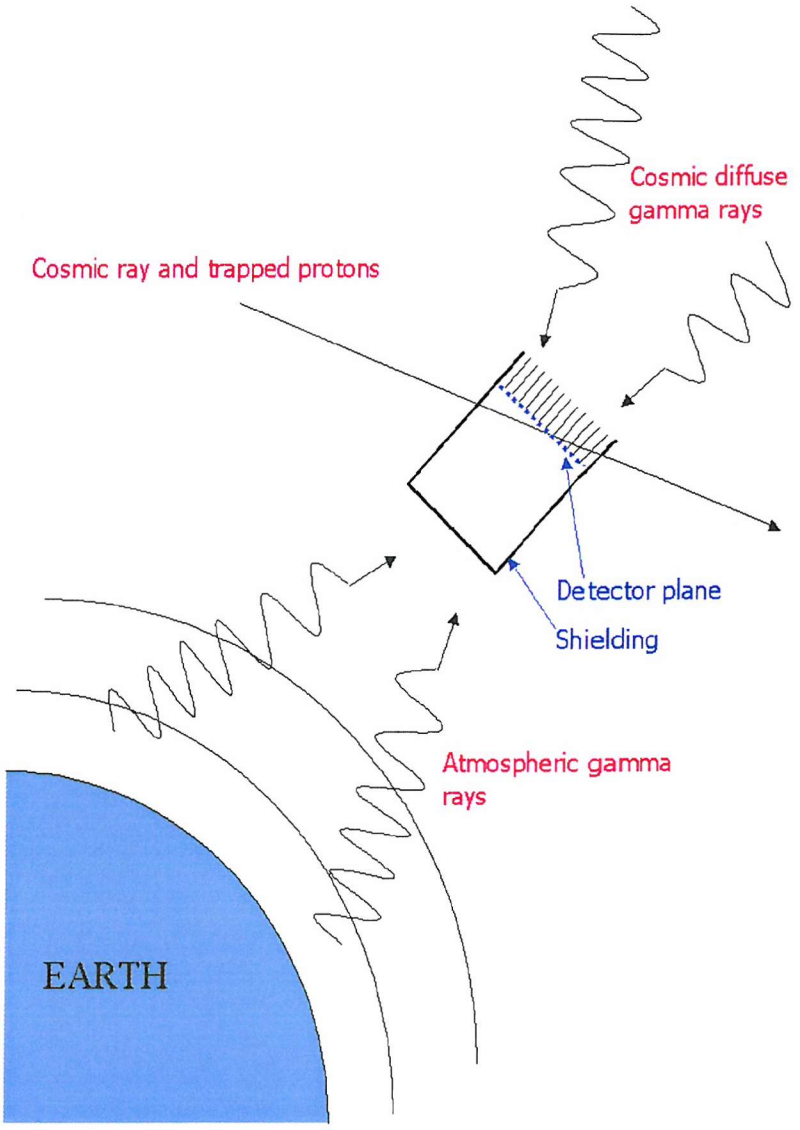

Figure 6.12: Sources of background noise for LEGRI

A given number of photons or protons are fired in over an imaginary sphere and the time equating to this number of photons or protons is calculated. The count rate is gained from the normalised spectra produced.

It has been assumed that LEGRI is pointing away from the Earth such that the cosmic diffuse background can be fired in over a hemisphere encompassing the aperture of the detector and the atmospheric background can be fired in over the hemisphere encompassing the shield. This *is* a valid assumption since it is most important to analyse the background noise during observations and this occurs when LEGRI is pointing in the direction assumed. Occasionally however LEGRI may observe at a slight tilt and therefore receive different quantities of atmospheric and cosmic diffuse background noise. This has been tested and the results are given in the respective following "Cosmic diffuse flux" and "Atmospheric flux" sections.

The sphere over which *photons* have been fired has a radius of 60cm to encompass the full detector and mask. To increase the radius of the sphere to include more of the spacecraft would increase the required CPU time beyond reasonable limits. The contribution from photons penetrating the spacecraft would be negligible and so a sphere of radius 60cm is a good compromise. Hadronic background can cause a dramatic increase in count rate particularly at the poles and some fraction could come from activation of the spacecraft. The radius of the sphere over which *protons* have been fired in is therefore 100cm so as to encompass the whole spacecraft and achieve maximum accuracy.

The energy spectra for the cosmic diffuse and atmospheric components are produced after one Monte-Carlo simulation using GEANT. As shown in Chapter 4 the spectral indices of the cosmic diffuse and atmospheric fluxes are -2.3 and -1.39 respectively. The input energy range for the cosmic diffuse flux is 10keV - 1MeV. The atmospheric photons are fired in over the hemisphere encompassing the shield of the detector and photons < 50 keV are therefore likely to be stopped by the shielding. The input energy range can therefore be restricted to 50keV - 1MeV for the atmospheric background noise. In both cases an upper limit of 1MeV is used This is again to maximise the efficiency of the Monte-Carlo simulations and minimise the CPU time required. The spectral forms used means there are few photons $>$ 1MeV. Any photons that are $>$ 1MeV are likely to pass straight through the spacecraft and detector system. If they do interact it is unlikely that the resulting counts will be within the range of the detectors (10 - 100 keV).

Although the atmospheric flux is latitude dependent the spectral index remains approximately constant. A Monte-Carlo simulation can be run for the equator only and the results scaled to give the count rate and spectrum at 28^0.

The background resulting from cosmic ray flux however is more complex to simulate. The cosmic ray background at the equator must be modelled separately

from that at 28^0 due to the different energy limits. It has been assumed that LEGRI has been in orbit for one year and has therefore been exposed to cosmic ray background noise for one year. LEGRI's orbit is represented as a sine wave in figure 6.13. If LEGRI is assumed to be nearer its latitude extremes above 14^0 and nearer the equator below this latitude then LEGRI spends $\sim 2/3$ of its orbit near the poles and $\sim 1/3$ near the equator. Thus the total exposure of LEGRI to the cosmic ray flux requires two separate simulations: one as if LEGRI had been at the poles for a year and one as if LEGRI had been at the equator for a year. The actual cosmic ray flux for LEGRI would then be represented by two thirds of the resulting spectrum from the polar simulation and one third of the spectrum from the equatorial simulation. The two can simply be added to give the overall cosmic ray spectrum for LEGRI for one year. Although rigidity is not linear with latitude it was not possible within available CPU time to model the cosmic ray flux at many different latitudes and sum the resulting contributions.

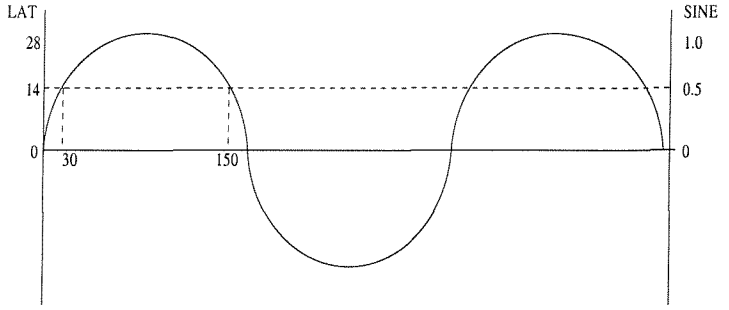

Figure 6.13: LEGRI's orbit spends $\sim 2/3$ of the time at 28^0 and $\sim 1/3$ at the equator.

Cosmic Diffuse Flux

As discussed in Chapter 4 the cosmic diffuse background component is the easiest to evaluate due to its isotropic nature, constant spectral shape and lack of rigidity dependence. The flux has been obtained from Schonfelder et al., 1980 and [47] and modified to equation 6.1 from discussions with F. Lei.

$$\begin{aligned} Flux &= 112E^{-2.3}dEphcm^{-2}keV^{-1}sr^{-1}s^{-1} \\ &= 448\pi\int_{10}^{1000} E^{-2.3}dEphcm^{-2}s^{-1} \\ &= 54.11phcm^{-2}s^{-1} \end{aligned} \tag{6.1}$$

Thus over a 60cm radius hemisphere (see above for an explanation of the size of the hemisphere):

$$Flux = 2\pi(60)^2 54.11 = 1.223 \times 10^6 phs^{-1}$$

Firing in 100 million photons over a 60cm radius hemisphere is therefore equivalent to 81.76 seconds. In practice several hundred million photons were used to achieve reasonable statistics.

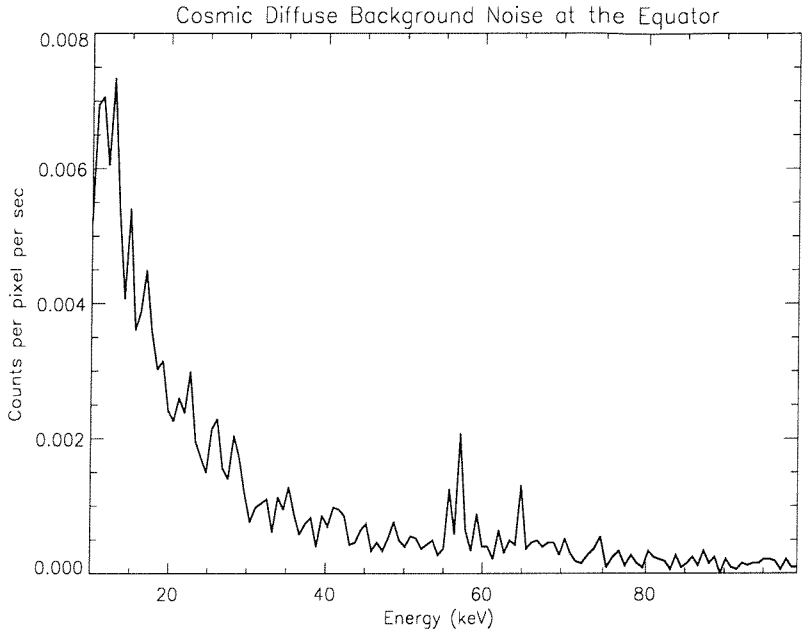

Figure 6.14: Cosmic diffuse background spectrum at the equator.

The cosmic diffuse background spectrum for LEGRI at the equator is shown in figure 6.14. Cosmic diffuse background noise is not dependent on latitude (see Chapter 4) and the spectrum will therefore be the same whether LEGRI is at the equator or poles. The cosmic diffuse component is greater at lower energies due to the input power law spectrum used and the better detection efficiency of the CdZnTe in this lower energy range. The count rate due to the cosmic diffuse flux, at the equator and poles, is $\sim 0.142 \pm 0.002$ c/cm^2/s. The Kα_2, Kα_1 and Kβ_1 edges of tantalum are 56.28, 57.54 and 65.2 keV respectively. The peaks seen in the cosmic diffuse spectrum are therefore likely to be due to fluorescence from the tantalum collimator. Fluorescence is the transformation of photons of relatively high energy to lower energy photons after photoelectric absorption. The original interaction of the photon and atom during photoelectric absorption creates an ionised atom. There is a vacancy in one of the inner shells which gets filled by an outer shell electron (or free electron). This generates an X-ray whose energy depends on the levels involved. Thus for any one absorber there may be a certain number of different emitted photon energies corresponding to the different shells involved. This gives rise to the characteristic Kα_2, Kα_1 and Kβ_1 edges seen here. The fluorescence from

the tantalum was confirmed when the Monte-Carlo simulations were run without the collimator and the peaks at $\sim$ 56, 57 and 65 keV disappeared.

These results are dependent on the assumption that LEGRI is pointing away from the Earth. Later simulations were conducted using a full sphere from which to fire in photons. These results showed the count rates for the cosmic diffuse flux were 0.165 $\pm$ 0.002 c/cm^2/s. The original results, therefore, are still valid and the worst case scenario would be $\sim$ 15% increase in the count rate.

Atmospheric Flux

The spectral index of the atmospheric background noise (Imhof et al, 1976) is taken to be the same at the equator and 28^0 (in reality $\alpha \sim$ -1.39 at the equator compared with $\alpha \sim$ -1.34 at the poles).

At the equator:

$$\begin{aligned} Flux &= 10^{-3}(E/100)^{-1.39} dEphcm^{-2}keV^{-1}sr^{-1}s^{-1} \\ &= 2.41\pi \int_{50}^{1000} E^{-1.39} dEphcm^{-2}s^{-1} \\ &= 2.909 phcm^{-2}s^{-1} \end{aligned} \tag{6.2}$$

Thus over a 60cm radius hemisphere:

$$Flux = 2\pi(60)^2 2.909 = 6.580 \times 10^4 phs^{-1}$$

At the poles:

$$\begin{aligned} Flux &= 2 \times 10^{-3}(E/100)^{-1.39} dEphcm^{-2}keV^{-1}sr^{-1}s^{-1} \\ &= 4.82\pi \int_{50}^{1000} E^{-1.39} dEphcm^{-2}s^{-1} \\ &= 5.819 phcm^{-2}s^{-1} \end{aligned} \tag{6.3}$$

Thus over a 60cm radius hemisphere:

$$Flux = 2\pi(60)^2 5.819 = 1.316 \times 10^5 phs^{-1}$$

Firing in 100 million photons over a 60cm radius hemisphere is therefore equivalent to 1519.75 seconds at the equator and 759.87 seconds at the poles. As with the cosmic diffuse several hundred million photons were used to achieve reasonable statistics. The smaller atmospheric flux and limited CPU time means that the statistics achieved for the cosmic diffuse flux are not easily possible for the atmospheric flux. The overall contribution of the atmospheric flux to the total background noise however is negligible and the lower statistics is not an issue.

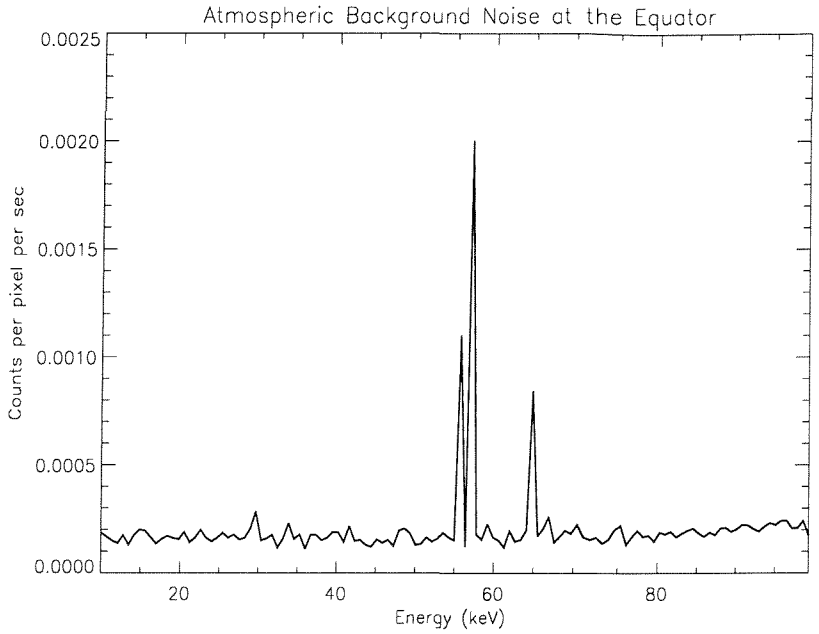

Figure 6.15: Atmospheric background spectrum at the equator.

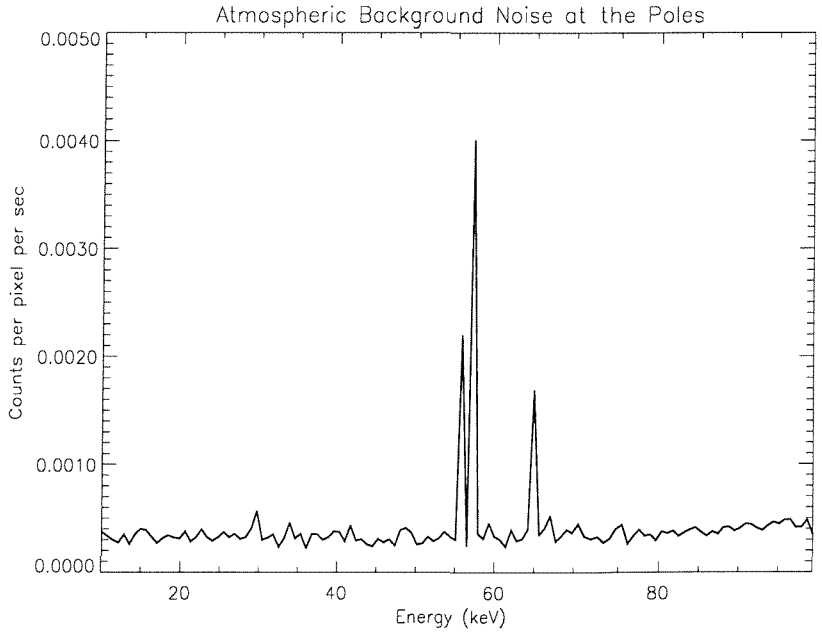

Figure 6.16: Atmospheric background spectrum at the poles.

The atmospheric component at the equator and poles is shown in figures 6.15 and 6.16. The fluorescence peaks are extremely clear but the overall contribution from the atmospheric is negligible at all energies. The atmospheric background noise is dependent on cosmic rays (see Chapter 4) and is therefore higher at the poles than at the equator (0.0242 ± 0.0002 c/cm^2/s compared to 0.0481 ± 0.0005 c/cm^2/s).

Again these results are dependent on the assumption that LEGRI is pointing away from the Earth. Later simulations whereby the atmospheric flux is fired in over a whole sphere encompassing the satellite do not alter the count rate and the original simulations are therefore valid whether LEGRI is pointing away from or towards the Earth.

Cosmic Ray Flux

The cosmic ray flux at the equator is completely different to that at the poles (Webber & Lezniak, 1974) due to the different cut-offs. The two must therefore be treated separately.

At the equator:

$$\begin{aligned} Flux &= (10^{-3}/5)(E/10^5)^{-2.7} prm^{-2} sr^{-1} s^{-1} MeV^{-1} \\ &= (4\pi/5) \times 10^{-3} \int_{12900}^{300000} (E/10^5)^{-2.7} prm^{-2} s^{-1} \\ &= 4.782 \times 10^3 prm^{-2} s^{-1} \end{aligned} \tag{6.4}$$

Thus over a 1m radius sphere:

$$Flux = 4\pi(1)^2 4.782 \times 10^3 = 6.010 \times 10^4 prs^{-1}$$

At the poles:

$$\begin{aligned} Flux &= (10^{-3}/5)(E/10^5)^{-2.7} prm^{-2} sr^{-1} s^{-1} MeV^{-1} \\ &= (4\pi/5) \times 10^{-3} \int_{6900}^{300000} (E/10^5)^{-2.7} prm^{-2} s^{-1} \\ &= 1.389 \times 10^4 prm^{-2} s^{-1} \end{aligned} \tag{6.5}$$

Thus over a 1m radius sphere:

$$Flux = 4\pi(1)^2 1.389 \times 10^4 = 1.745 \times 10^5 prs^{-1}$$

Firing in 100 million protons over a 1m radius sphere is therefore equivalent to 1663 secs at the equator and 573 secs at the poles.

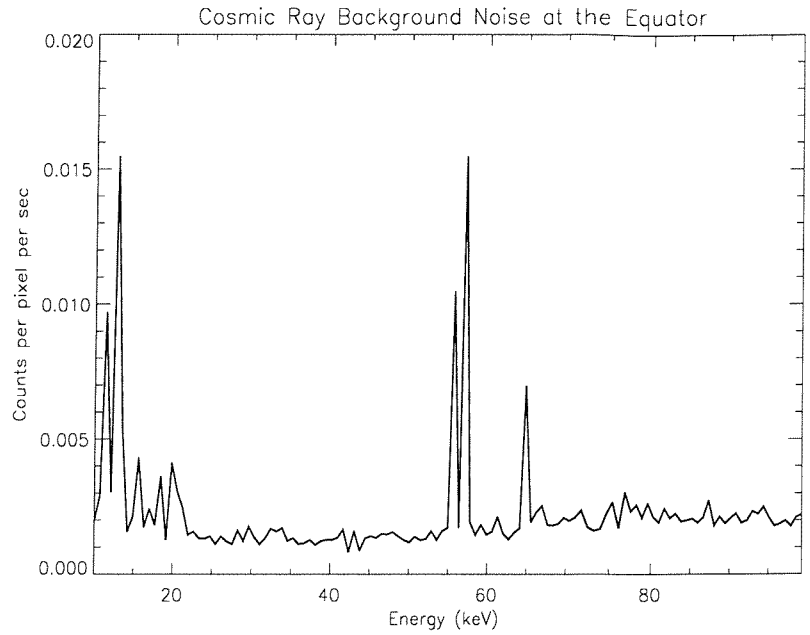

Figure 6.17: Cosmic ray background spectrum at the equator.

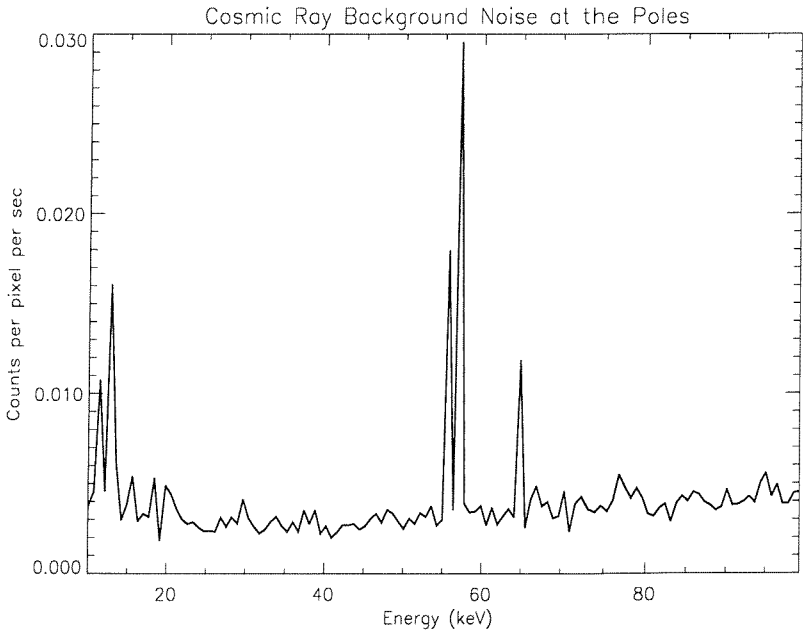

Figure 6.18: Cosmic ray background spectrum at the poles.

Figures 6.17 and 6.18 show the total cosmic ray background spectra at the equator and poles respectively. Again the fluorescence peaks can be seen and the contribution at the poles is greater than at the equator (0.262 ± 0.011 c/cm^2/s compared to 0.521 ± 0.011 c/cm^2/s).

6.3.4 Total simulated spectra and count rates

Figures 6.19 and 6.20 show the total background noise at the equator and poles with a break down of each of the constituents. In both cases the atmospheric background noise is negligible. At low energies (below $\sim$ 25-30 keV) the cosmic diffuse and cosmic ray components are roughly equal. Above these energies the cosmic ray component dominates. Figure 6.21 shows a comparison of the total background noise at the equator and poles. The two spectra have very similar shapes with clear fluorescence peaks but the background noise at the poles is much higher over virtually all energies.

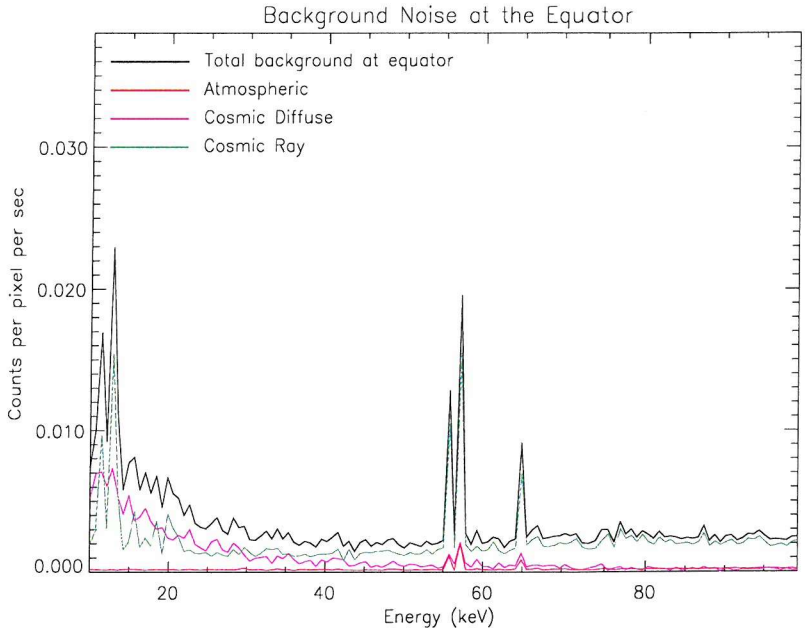

Figure 6.19: Break down of the background components at the equator (not including any effects due to the SAA).

Table 6.2 shows the count rate contributions from each component. The cosmic ray contribution accounts for more than 60% of the total count rate at the equator and more than 70% at the poles. The total count rate increases by ~ 0.28 c/cm^2/s at the poles which is in excellent agreement to the observed increase of ~ 0.25 c/cm^2/s (see section 4.2).

The count rates shown in table 6.2 are taken from raw spectra and do not include any effects due to detector response. Charge trapping and poor energy resolution (discussed in Chapter 7) "blur" the spectra and can shift some of the energy deposits

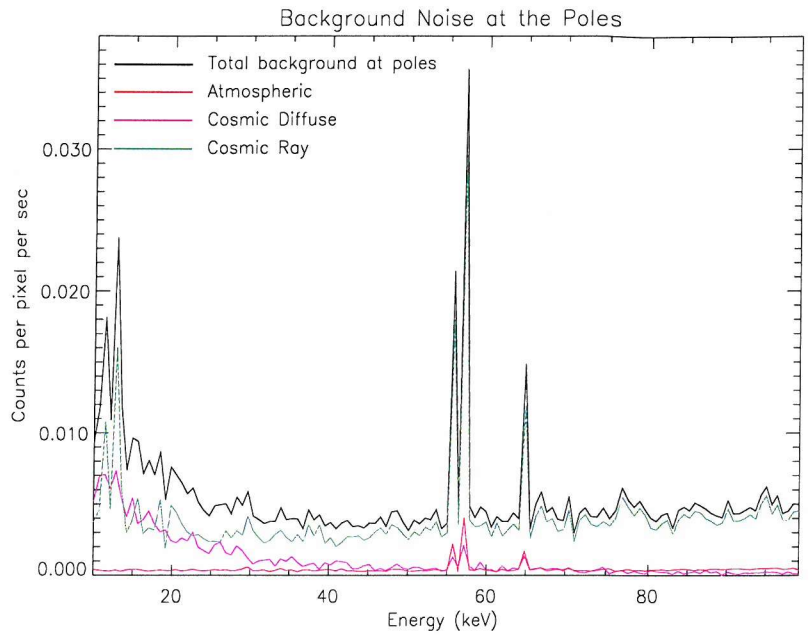

Figure 6.20: Break down of the background components at the poles (not including any effects due to the SAA).

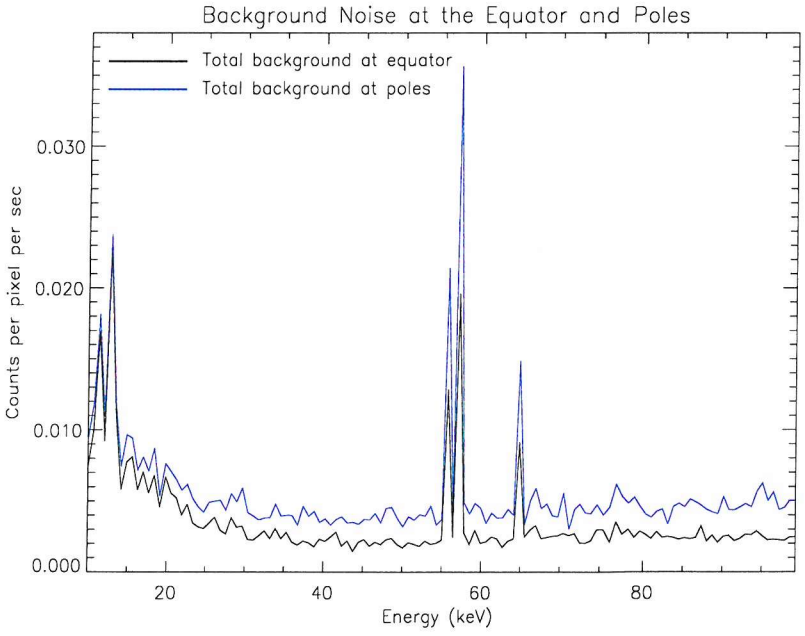

Figure 6.21: Total background count rate at the equator and poles (not including any effects due to the SAA).

Component	Equator c/p/s	Poles c/p/s
Cosmic Diffuse	0.142	0.142
Atmospheric	0.024	0.048
Cosmic Ray	0.262	0.521
Total	0.428	0.712

Table 6.2: Background noise count rates at the equator and poles. Errors are shown in the text.

down to lower energies. This could affect the count rate in the energy band 10-100 keV if some deposits are shifted from > 100 keV to <100 keV. Since the background noise components discussed so far follow a power law, the contribution from energy deposits being shifted from > 100 keV to < 100 keV is small. The resulting count rates are still, therefore, accurate but may be slightly lower than observed count rates. Comparing simulated and observed count rates this is shown to be exactly the case. The simulated equatorial count rate of 0.428 $\pm$ 0.012 c/cm^2/s *is* slightly lower than the observed count rate of 0.5 c/cm^2/s. Also the simulated polar count rate of 0.712 $\pm$ 0.012 c/cm^2/s *is* slightly lower than the observed count rate of 0.75 c/cm^2/s.

6.4 Conclusions and Discussion

The simulations provide count rates and spectra for the different types of static background noise which are compared to observational data. The simulated count rate increases from $\sim$ 0.42 c/cm^2/s at the equator to $\sim$ 0.71 c/cm^2/s at the poles. These count rates are slightly lower than those observed due to the effects of charge trapping and energy resolution which are not taken into account at this stage. In spite of this the observed count rates of $\sim$ 0.5 c/cm^2/s and $\sim$ 0.75 c/cm^2/s at the equator and poles respectively *are* in excellent agreement with our simulations. This increase in count rate is due to the effects of geo-magnetic cut-off on the cosmic ray and atmospheric background components. The cosmic ray component accounts for more than 60% of the total count rate at the equator and more than 70% at the poles. The simulated spectra show significant peaks at $\sim$ 56, 57 and 65 keV due to fluorescence from the tantalum collimator. The next chapter studies the effects of an observed and simulated SAA pass on LEGRI. The internal sources of the increase in count rate are determined and the recovery of the detector after proton bombardment during the SAA is discussed.

Chapter 7

Analysis of the effects of an SAA pass on LEGRI

7.1 Introduction

The previous chapter described how Monte-Carlo simulations can be used to describe the static background noise for LEGRI. The term "static" was used to describe those background components which either do not vary or are at most only slowly varying. This included the cosmic diffuse, atmospheric and cosmic ray fluxes only.

There is, however, an additional source of background noise for Low Earth Orbit satellites including LEGRI. Up to a third of any one orbit for LEGRI could include a passage through the South Atlantic Anonomaly (SAA) during which the spacecraft and its detectors receive an intense dose of protons. Although the detectors are turned off actually during the pass the intense proton bombardment results in a large number of activated isotopes. These isotopes subsequently decay to produce an increase in the background noise. As the radioactive isotopes decay the additional background noise dies away over a characteristic timescale. This is now a dynamic situation and the simulations must be modified to allow for the evolution of the induced count rates.

In this chapter the effects of an SAA pass are studied using observational and simulated data. The simulations are compared to observations and then used for further analysis of the SAA background noise. This analysis will concentrate on identifying the most significant components of the spacecraft contributing to the increased count rate.

7.2 Effect of the SAA on LEGRI observed in-flight background

Chapter 6 uses observational data to study the effect of latitude on the background noise in LEGRI. Here the data is used to study the effects of an SAA pass. Figure

6.3 shows the orbit paths for DOY 220 1997 and this day is also used for the analysis of the SAA pass. Window 0 does not include an SAA pass but window 8 on the same day does include an SAA pass. The detector is turned off actually during the pass but once turned on again the induced radioactivity is still decaying and producing background count rates. Figure 7.1 shows counts against time after the SAA pass. The geomagnetic cut-off goes some way to counteracting the SAA contribution and must therefore be subtracted from window 8. Window 0 (figure 6.5) is subtracted from window 8 to give the sole SAA contribution in figure 7.2. The count rate drops from 1.3 c/cm^2/s to zero in $\sim$ 30 minutes. This estimate for the count rate due to the SAA is higher than previous estimates of 0.5 c/cm^2/s [52] and the decay time is also quicker than expected [52]. The assumption that subtracting window 0 from window 8 removes the non-SAA background noise may be invalid or inaccurate. Window 0 and window 8 may be different in terms of orbital position although data were selected for the same latitudes. LEGRI may therefore experience different levels of non-SAA background noise.

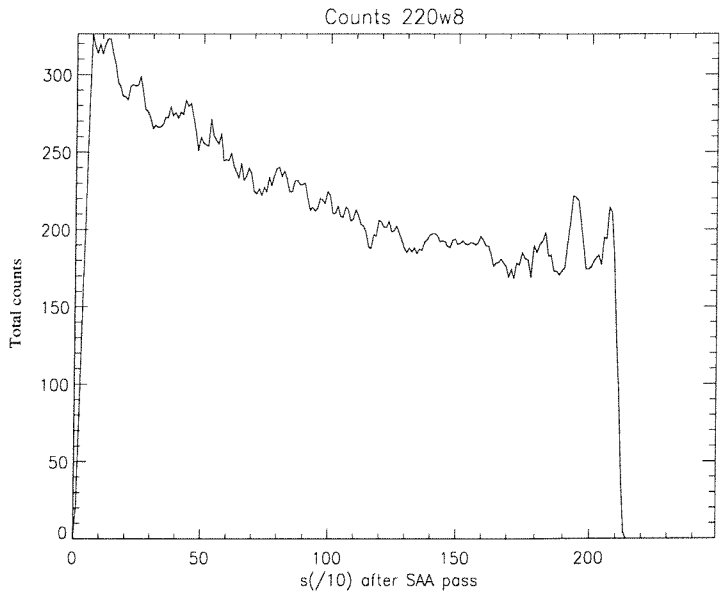

Figure 7.1: Counts v time for DOY 220 window 8. There is an SAA pass though the effects of geomagnetic cut off are superimposed on top of any SAA effect

Figures 6.5, 7.1, 7.2 each show a periodicity due to the instability of the detectors below channel 900. This is explained and verified in section 6.2.

Figure 7.3 shows a small high frequency sine wave as the satellite moves to and from its extremes of latitude superimposed on a larger lower frequency sine wave due to the slow exponential decay of radiation due to SAA passes.

Further analysis of DOYs 284-289 and 219-220, when LEGRI is not pointing at a specific source, give us a colour map of how the background count rate varies with the orbit path. North-South ("downs") passes have not passed through the SAA

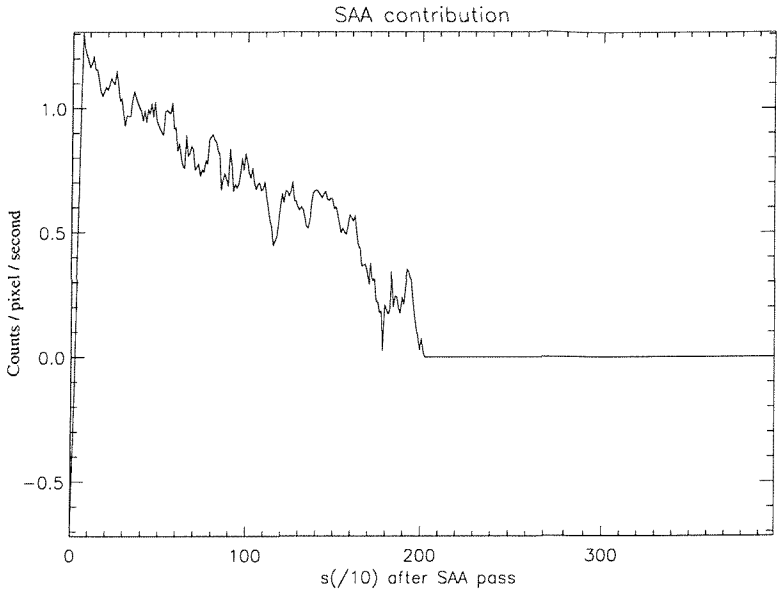

Figure 7.2: Count rate due solely to the SAA pass just experienced.

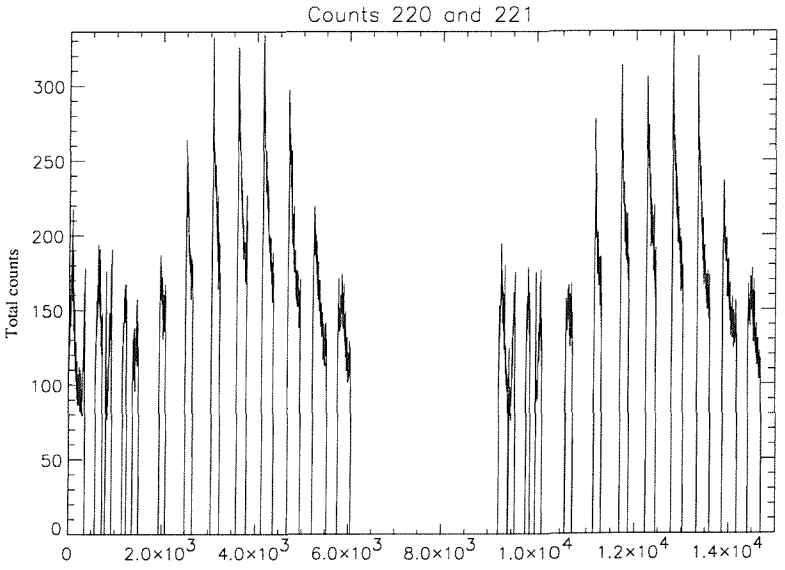

Figure 7.3: Counts v time for DOYs 220 and 221 showing the high frequency geomagnetic sine wave superimposed on the lower frequency sine wave due to continual SAA passes.

and may dilute any effects due to the SAA. They have therefore been separated from the South-North ("ups") passes. Figure 7.4 shows the "ups" and figure 7.5 shows the "downs".

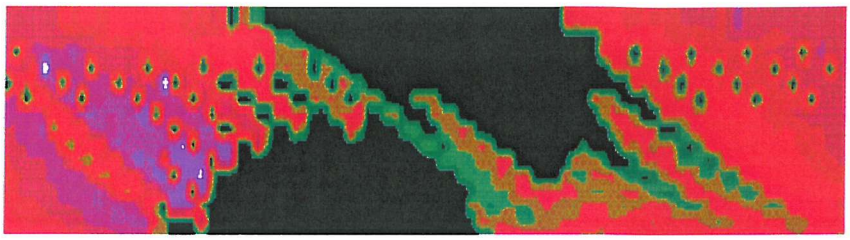

Figure 7.4: Colour map of how the background count rate varies with orbital position (plot shows latitude versus longitude), channels > 900, South-North passes only. Purple/white show areas show regions of intense background noise. The intensity of the background noise is seen to increase after the SAA pass.

Figure 7.5: Colour map of how the background count rate varies with orbital position. Details as for figure 7.4 but here only North-South passes are shown.

These colour maps give us an immediate idea where the background noise "hot spots" are. The dark semi-cirle in figure 7.4 is where the detector has been turned off during the SAA pass. Immediately afterwards there is a dramatic increase in background noise due to the radioactivity induced in the spacecraft during the pass.

7.3 Radiation Environment

Figure 7.6 shows the proton flux, for a spacecraft 650 Km high in a 28^0 orbit. The contours range from < 10 pr/cm^2/s to several 1000 pr/cm^2/s. The SAA flux that LEGRI will receive on any one orbit depends on the extent to which the path cuts through the SAA. Table 7.1 shows the peak and total proton fluxes for a day's passes. The first 4 orbits miss the SAA altogether. Then as the orbit

precesses the intensity of the pass increases until the total flux reaches a maximum of 1.66×10^6 protons/cm^2. The total flux per orbit then decreases down to zero by the end of the day. These are "typical" passes based on a SPenvis (http://www.spenvis.oma.be/spenvis) simulation and do not correspond to specific LEGRI orbits.

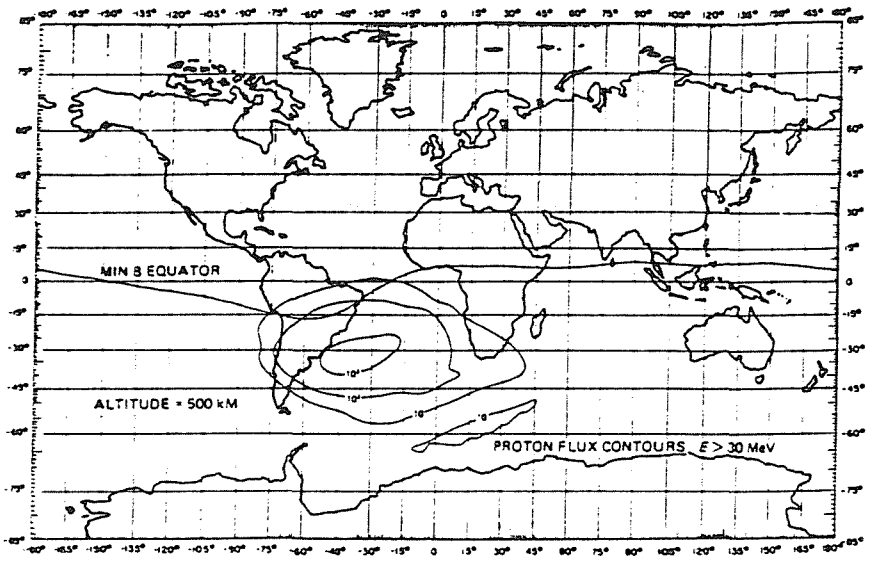

Figure 7.6: SAA proton flux contours, [76].

7.4 Monte-Carlo simulations of spectra and count rates

Since it is not possible to simulate a constantly varying flux within GGOD three separate simulations were used. First a flux of 650 prcm^{-2}s^{-1} for 280s, then 1000 prcm^{-2}s^{-1} for 250s and again 650 prcm^{-2}s^{-1} for 280s. This is to account for the lower radiation levels at the edges of the SAA. Originally a constant flux model was used but this was found to be inappropriate since much of the proton flux occurs in the centre of the SAA and therefore has at least some time to decay before the end of the pass is reached and the detectors are turned on again. Figure 7.7 shows the input proton flux for the variable flux and constant flux models.

Section 6.3.3 discussed how the input spectra for each of the static background components is used in the Monte-Carlo simulations. As with the cosmic ray flux the SAA protons are fired in over an imaginary sphere of radius 100cm.

Thus the simulated flux per orbit is as follows:

$$\begin{aligned} 650\text{prcm}^{-2}\text{s}^{-1} &= 650 \times \text{surface area of sphere} \times \text{exposure time} \\ &= 650 \times 4\pi.100^2 \times 280 \\ &= 2.287 \times 10^{10}\text{protons} \end{aligned}$$

Orbit No	Peak Flux (/cm^2/sec)	Orbit start time (hrs)	Total flux per orbit (/cm^2/orbit)
1	0.00E+00	0.0	0.00E+00
2	0.00E+00	1.5	0.00E+00
3	0.00E+00	3.0	0.00E+00
4	0.00E+00	4.5	0.00E+00
5	1.22E+00	6.0	1.46E+02
6	3.33E+02	7.5	2.47E+05
7	1.51E+03	9.0	9.77E+05
8	2.44E+03	10.5	1.57E+06
9	2.55E+03	12.0	1.66E+06
10	2.19E+03	13.5	1.29E+06
11	1.27E+03	15.0	7.26E+05
12	4.47E+02	16.5	2.01E+05
13	1.25E+00	18.0	1.51E+02
14	0.00E+00	19.5	0.00E+00
15	0.00E+00	21.0	0.00E+00

Table 7.1: Peak and total proton fluxes of the SAA pass per orbit at energy > 1.0 MeV

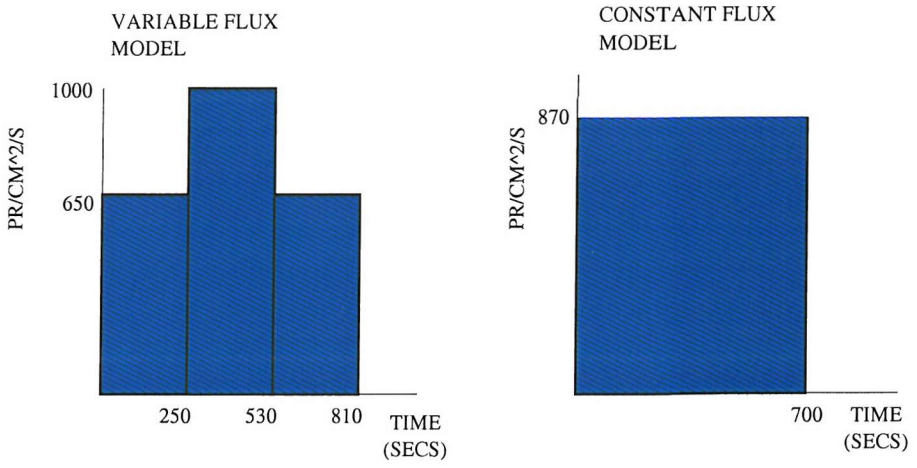

Figure 7.7: Variable input flux model versus constant input flux model. The total integrated flux is the same for each.

(7.1)

$$\begin{aligned} 1000\text{prcm}^{-2}\text{s}^{-1} &= 1000 \times \text{surface area of sphere} \times \text{exposure time} \\ &= 1000 \times 4\pi.100^2 \times 250 \\ &= 3.1415 \times 10^{10}\text{protons} \end{aligned}$$

(7.2)

$$\begin{aligned} \text{Total simulated flux} &= (2 \times (2.287 \times 10^{10})) + (3.1415 \times 10^{10}) \\ &= 7.71 \times 10^{10}\text{protons/orbit} \end{aligned}$$

(7.3)

According to SPenvis (table 7.1) if LEGRI passes through the *centre* of the SAA the flux would be:

$$\begin{aligned} 1.66 \times 10^6\text{pr/cm}^2\text{/orbit} &= (1.66 \times 10^6) \times \text{surface area of sphere} \\ &= (1.66 \times 10^6) \times 4\pi.100^2 \\ &= 2.086 \times 10^{11}\text{protons/orbit} \end{aligned}$$

(7.4)

or for a more moderate pass the flux would be:

$$\begin{aligned} 9.77 \times 10^5\text{pr/cm}^2\text{/orbit} &= (9.77 \times 10^5) \times \text{surface area of sphere} \\ &= (9.77 \times 10^5) \times 4\pi.100^2 \\ &= 1.227 \times 10^{11}\text{protons/orbit} \end{aligned}$$

(7.5)

Thus if the simulations are to represent a moderate pass the results should be scaled by a factor of $\frac{1.227\times10^{11}}{7.715\times10^{10}} = 1.59$ or $\frac{2.086\times10^{11}}{7.715\times10^{10}} = 2.7$ to represent a very intense pass.

Although three separate input proton pulses were used, as shown in the variable flux model in figure 7.7, only one Monte-Carlo 1 was required (see Chapter 4 for an explanation of Monte-Carlo 1 and Monte-Carlo 2). This Monte-Carlo 1 was then said to represent different lengths of time so that the respective intensities were different. For example, say 100 million protons were fired in in Monte-Carlo 1, a peak of intensity 650 pr/cm^{-2}/s would represent 1.2 seconds but a peak of 1000

pr/cm^2/s would represent 0.8 seconds. The cooling times (again see Chapter 4) for each peak were adjusted so that all three aligned after the simulated SAA pass and their results could therefore be added. The cooling times used ranged from an equivalent of $\sim$ 1 second to $\sim$ 90 minutes after the pass. No prompt spectra or count rates were used since the detectors were turned off actually during a pass.

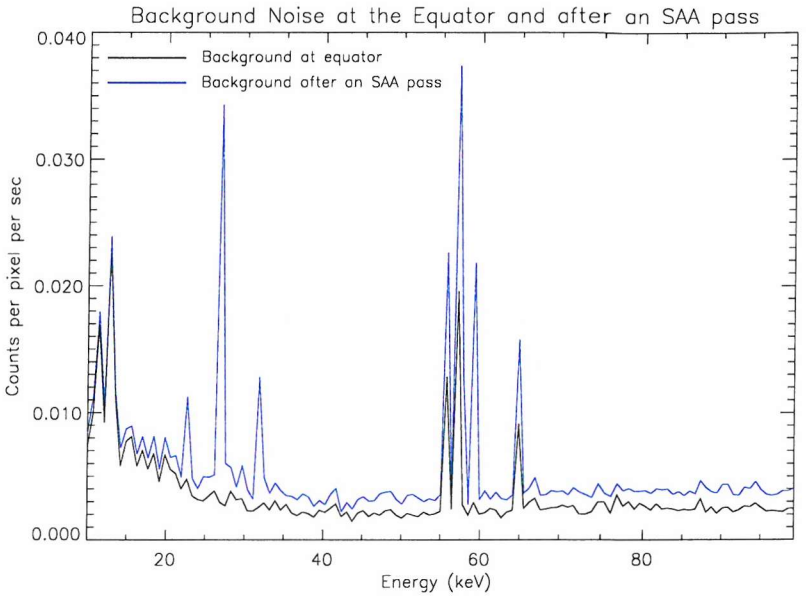

Figure 7.8: Total background count rate at the equator with and without an SAA pass.

Figure 7.8 shows how a simulated passage through the SAA affects the spectrum of the total background noise. The spectrum has a similar shape but has additional peaks as shown in table 7.2. The CdZnTe undergoes proton capture whereby some of the cadmium is changed to indium and the some of the tellurium is changed to iodine. The indium and iodine subsequently decay by electron capture (see Chapter 4 and below). The transition of electrons between shells in the resulting cadmium and tellurium gives rise to the lines seen. This also occurs for tungsten in the model which becomes rhenium after proton capture. Again the rhenium decays by electron capture.

Electron capture decay process in indium, iodine and rhenium:

$^{49}\mathrm{In} + \mathrm{e}^- \rightarrow {}^{48}\mathrm{Cd} + \nu$

$^{53}\mathrm{I} + \mathrm{e}^- \rightarrow {}^{52}\mathrm{Te} + \nu$

$^{75}\mathrm{Re} + \mathrm{e}^- \rightarrow {}^{74}\mathrm{W} + \nu$

7.4.1 Simulating realistic spectra

The simulated spectra discussed so far are for a perfect detector. This was sufficient for the static background noise since the fluxes modelled followed a power law. There were, therefore, few energy deposits > 100 keV that may be shifted to < 100

Line energy (keV)	EC Isotope	Decay process	Transition Isotope
22.69	^{49}In	K_{α_3} transition	^{48}Cd
26.71	^{49}In	K_{β_4} transition	^{48}Cd
26.87	^{53}I	K_{α_3} transition	^{52}Te
31.81	^{53}I	$KO_{2,3}$ transition	^{52}Te
59.31	^{75}Re	K_{α_1} transition	^{74}W

Table 7.2: Energy of the lines in the SAA spectrum. Electron Capture (EC) occurs on the EC isotope which produces the "Transition" isotope. This gives rise to the spectral lines through transitions of electrons between shells.

keV and into the energy range being considered (see later for an explanation of why detector response may shift energy deposits). For the SAA spectra however the flux is not power law and the raw energy deposits calculated by the Monte-Carlo are substantially changed by the detector response. This was initially noticed as a result of the simulated count rates being significantly lower than the observed count rates. The main effects to be considered are charge trapping/incomplete charge collection and energy resolution.

Charge trapping / incomplete charge collection

Cadmium telluride suffers from a problem known as charge trapping which occurs due to the low mobility of the electrons and particularly the holes within the material. This means that instead of electrons and holes drifting all the way to the electrodes as they should, some get trapped by imperfections in the crystal. Figure 7.9 shows the resulting pulse height spectrum where the full signal has not been collected and there is a characteristic tail on the peak.

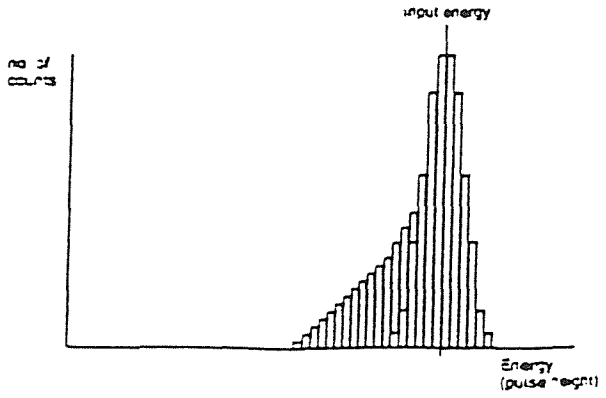

Figure 7.9: Effect of charge trapping on a CdTe spectrum.

To make the Monte-Carlo spectra more realistic therefore some of the energy deposits should be shifted down to simulate this tailed spectrum. Energy deposits > 100 keV may be shifted into the 10 - 100 keV region. The resulting spectra of the initial simulations should therefore be extended up to 500 keV to allow for any deposits that may be later shifted into the 10 - 100 keV region and so appear in the final data. This has the effect of increasing the overall count rate in this energy band as well as altering the shape of the spectrum.

Energy resolution

Energy resolution defines how accurately a detector can measure the energy of a photon. Charge carrier statistics can effect the energy resolution as errors in counting the electrons may be significant. The main component which may worsen the energy resolution is due to the electronic noise which is added to the signal by the readout electronics. As a result of these contributions the signal received by the detector may not perfectly match the input photon energy and this results in a simple, Gaussian blurring about the true energy as shown in figure 7.10.

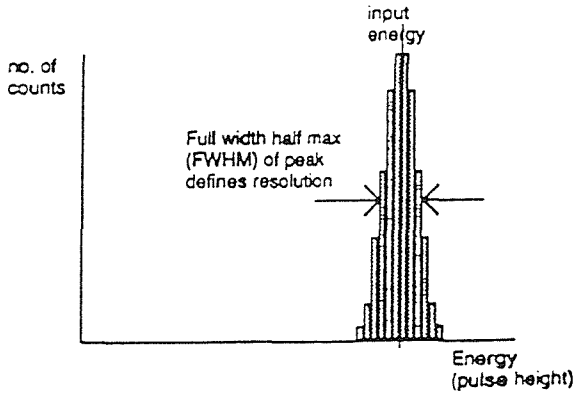

Figure 7.10: Effect of energy resolution on a spectrum.

The blurring algorithm is shown in figure 7.11. A γ-ray entering the CdZnTe pixel reaches a depth d (depending on its energy) which is "blurred" according to a simple Gaussian law. This calculation is performed for each of the n photons entering the crystal. To calculate the charge trapping effect it is assumed that the electrons are always seen ie they always reach the positive plate. The holes are trapped depending on the depth of the original photon interactions. If d=0 then no holes are trapped but if d=D (the full width of the pixel) then 100% of the holes may be trapped. The interpolation for the holes is linear between 0 and 100%

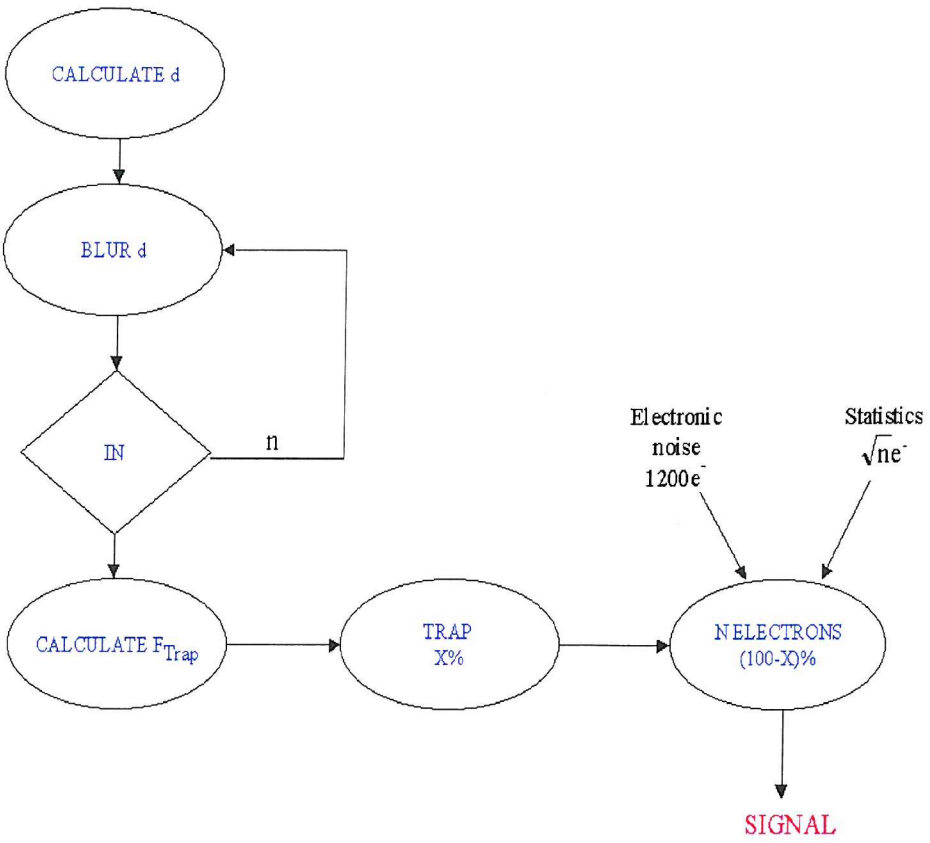

Figure 7.11: The blurring algorithm applied to the raw spectra

for 0<d<D. These effects are combined with those due to electronic noise and the statistics of the charge carriers to produce the final signal as shown in figure 7.11.

Observational data suggests that the shape of the spectrum is unchanged by a passage through the SAA yet figure 7.8 shows that there are additional peaks in the post-SAA raw energy spectrum. Figure 7.12 shows a comparison of pre and post SAA spectra after the blurring algorithm has been applied. The two spectra have a very similar shape which is in agreement with observations. Any changes to the raw energy deposits is totally masked by the detector response and we cannot, therefore, use the observed spectra for any diagnostic purposes.

Figure 6.19 shows the count rate is higher below energies of about 20 keV due to the spectral forms used for the various types of background. This shows up as the blurred peak at $\sim$ 20 keV in figure 7.12. The SAA blurred peak at $\sim$20keV is slightly shifted due to the additional peaks shown in figure 7.8. The lower count rates shown at $\sim$10-15 keV are an anomaly due to the blurring of the spectra. The blurred peak at $\sim$55 keV is due to fluorescence from the tantalum collimator (as

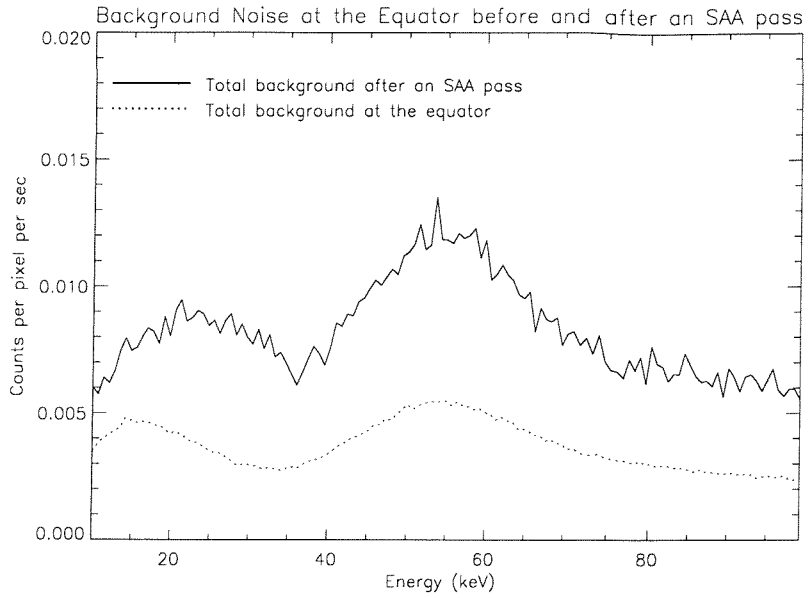

Figure 7.12: Total background count rate before and after an SAA pass with blurring

Time after SAA pass Secs	No blurring Moderate pass $c/cm^2/s$	No blurring Intense pass $c/cm^2/s$	Blurred Moderate pass $c/cm^2/s$	Blurred Intense pass $c/cm^2/s$
0	0.41	0.55	0.66	0.89
200	0.36	0.48	0.58	0.78
600	0.28	0.38	0.45	0.61
1200	0.21	0.29	0.34	0.46
1800	0.17	0.23	0.28	0.38
5250	0.08	0.11	0.13	0.18

Table 7.3: The increase in count rates after a moderate and intense SAA pass, with and without blurring. Errors on all count rates are $< 10\%$.

discussed earlier) combined with the radiation effects. There is an overall increase in the counts above $\sim$ 60 keV due to deposits that were in the unblurred spectra above 100 keV now shifted down in the blurred spectra to below 100 keV.

Table 7.3 shows the simulated post SAA count rates with and without blurring for both a moderate pass and a very intense pass. Observations are typical of a moderate pass and indicate an increase in the count rate of 0.5 $c/cm^2/s$ immediately after the SAA [52] which is in line with our simulations after blurring. After approximately one orbit (5250 seconds) up to $\sim$ 20% of the count rate remains and this would accumulate on top of any subsequent SAA pass. Thus our simulations assume no SAA passes in the previous several orbits. This is slightly inaccurate since prior to a moderate pass it is likely that the satellite at least "clipped" the SAA.

Figure 7.13 shows how the count rate decays with time after a moderate pass through the SAA. The blurred count rates are consistently higher than the unblurred count rates indicating that even 90 minutes after the SAA pass there are counts above 100 keV which get shifted below 100 keV by the blurring algorithm. The decay appears exponential but attempts to fit the curves to a single exponential failed. The decay profiles are made up of many different exponentials as there are many different activated isotopes decaying. An analysis of the the SAA count rate by isotope and volume is provided in the next section.

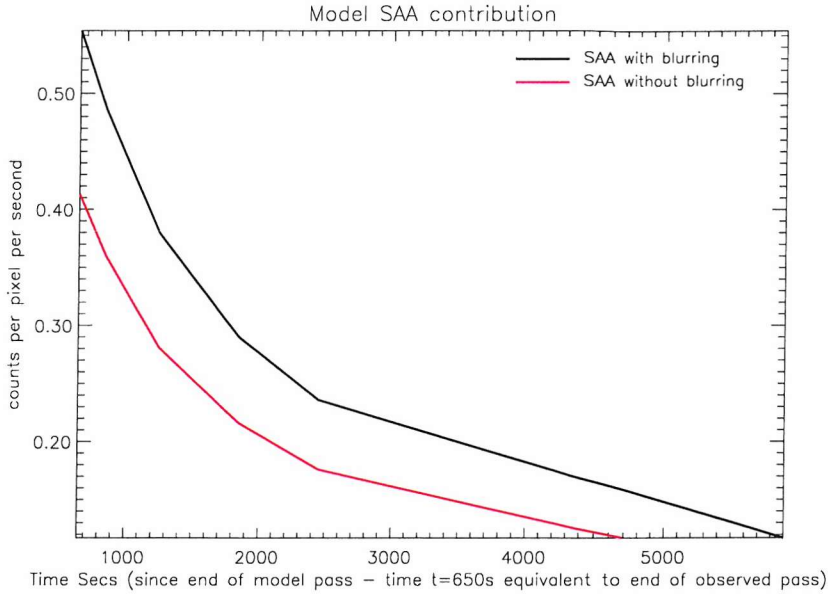

Figure 7.13: The decay of the background count rates after an SAA pass.

7.5 Analysis of spacecraft activation

The decay profiles of the previous section indicate that there must be more than one decaying isotope producing the post-SAA background count rate. Figure 7.14 shows a break-down by isotope of the count rate immediately after the SAA. Tungsten is the most significant contributor which at first glance may seem unusual since there is little tungsten near enough to the detectors in the model to produce such a count rate. On closer inspection most of the significant contributors, such as indium, antimony, iodine and bismuth, are not included in the model at all. In each case the previous isotope, ie that with an atomic number smaller by one, *is* in the model, close to the detector plane and not producing a significant count rate. The most likely explanation for this is that proton capture occurs on, for example, the cadmium, tin, tellurium, tantalum or lead which then becomes indium, antimony, iodine, tungsten or bismuth and decays producing the count rates seen. Note that this agrees with our identification of the lines in figure 7.8.

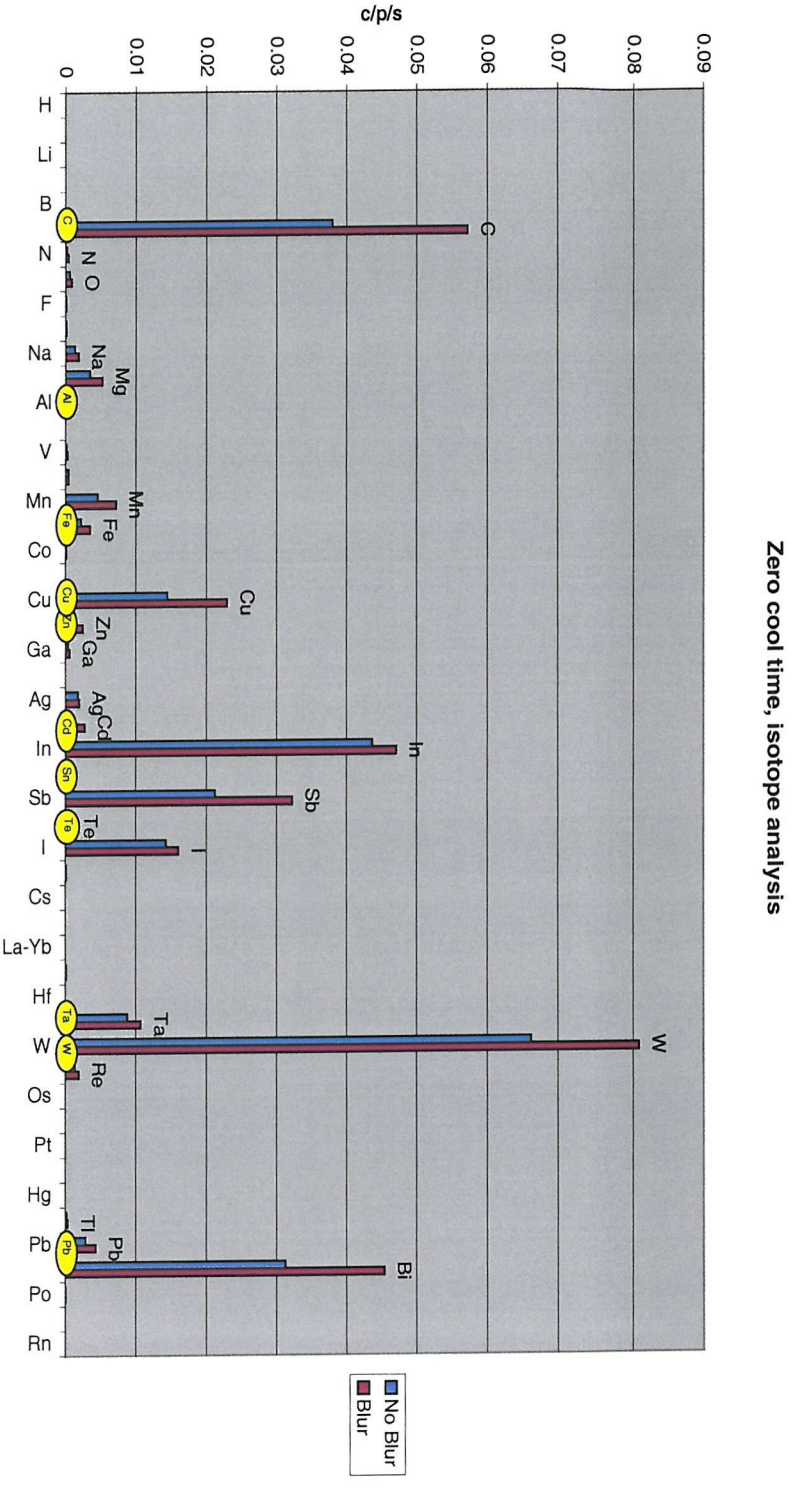

Figure 7.14: Break down by isotope of the background noise immediately after the SAA. The yellow discs indicate those isotopes which are present in the model of LEGRI

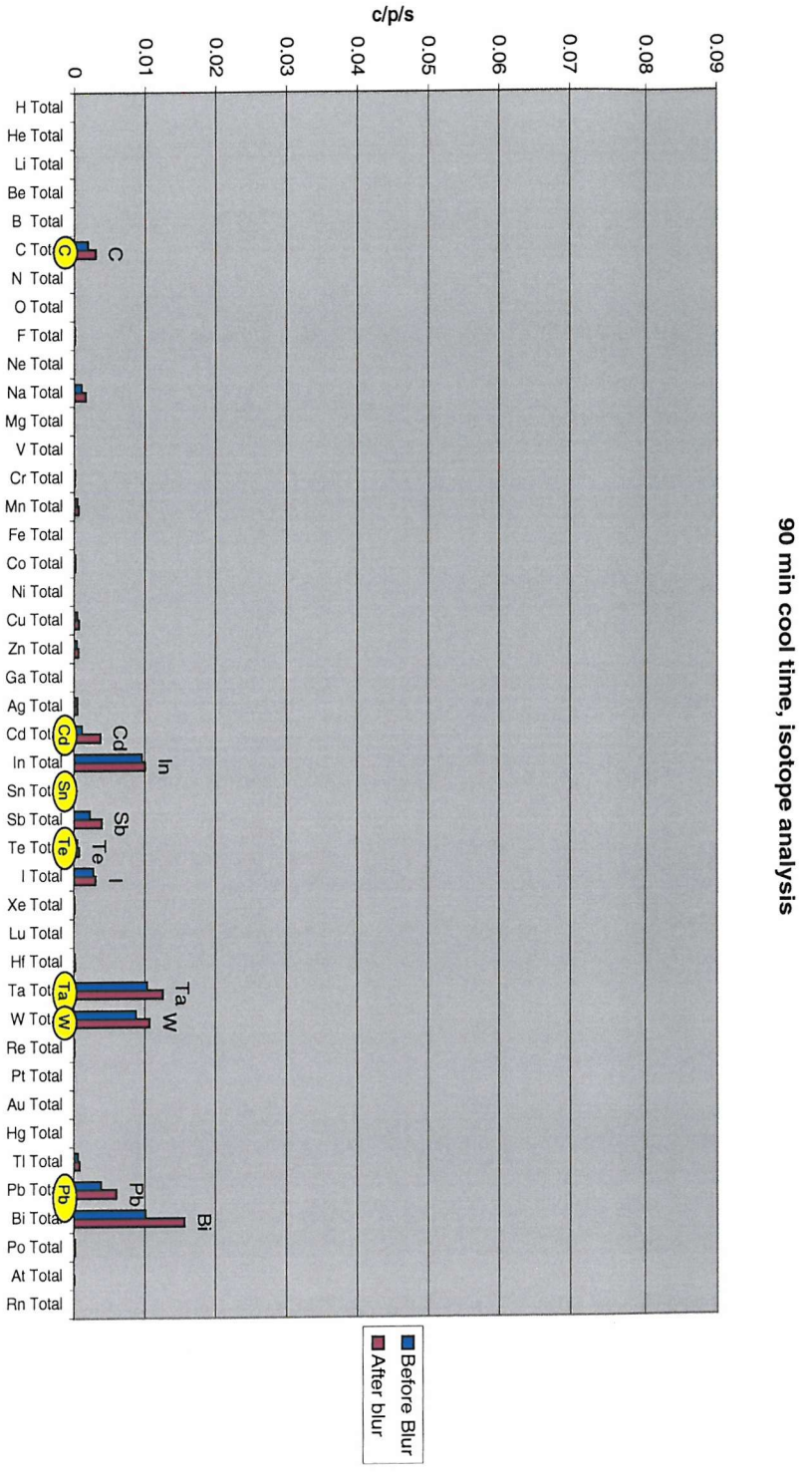

Figure 7.15: Break down by isotope of the background noise 90 minutes after an SAA pass. The yellow discs indicate those isotopes which are present in the model of LEGRI

Figure 7.15 shows a break down by isotope 90 minutes after the simulated SAA pass. All of the isotope contributions have decreased and figure 7.15 is on the same scale as figure 7.14 to show this. The count rates relative to each other, however, have changed. The tungsten isotopes contributions have dropped below the tantalum indicating that the tantalum isotopes are long-lived whereas the tungsten isotopes have short half-lives.

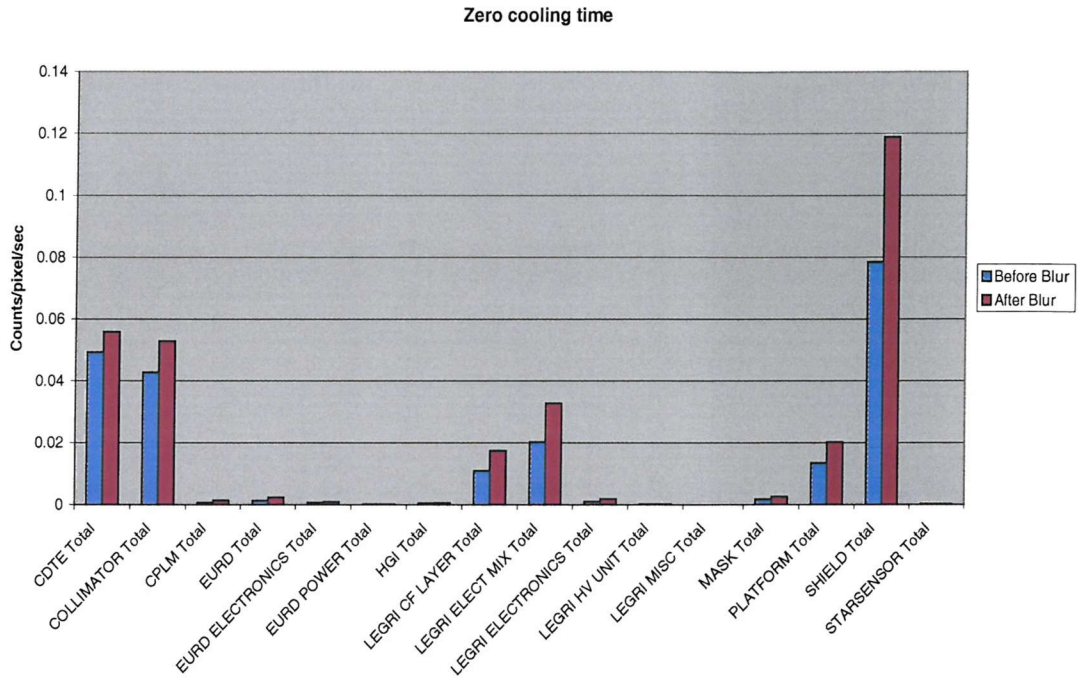

Figure 7.16: The background noise immediately after an SAA pass split by volume

By analysing which volumes (components of the spacecraft) the background noise comes from, future satellites can be designed to minimise internal sources. The background count rates can be grouped by volume instead of by isotope for this purpose. Figure 7.16 shows the volume contributions immediately after the SAA. The shield is the highest source of background noise though this includes the lead, tantalum, tin and iron. The cadmium telluride and collimator are also significant contributors. Volumes outside of the LEGRI detector itself are insignificant since

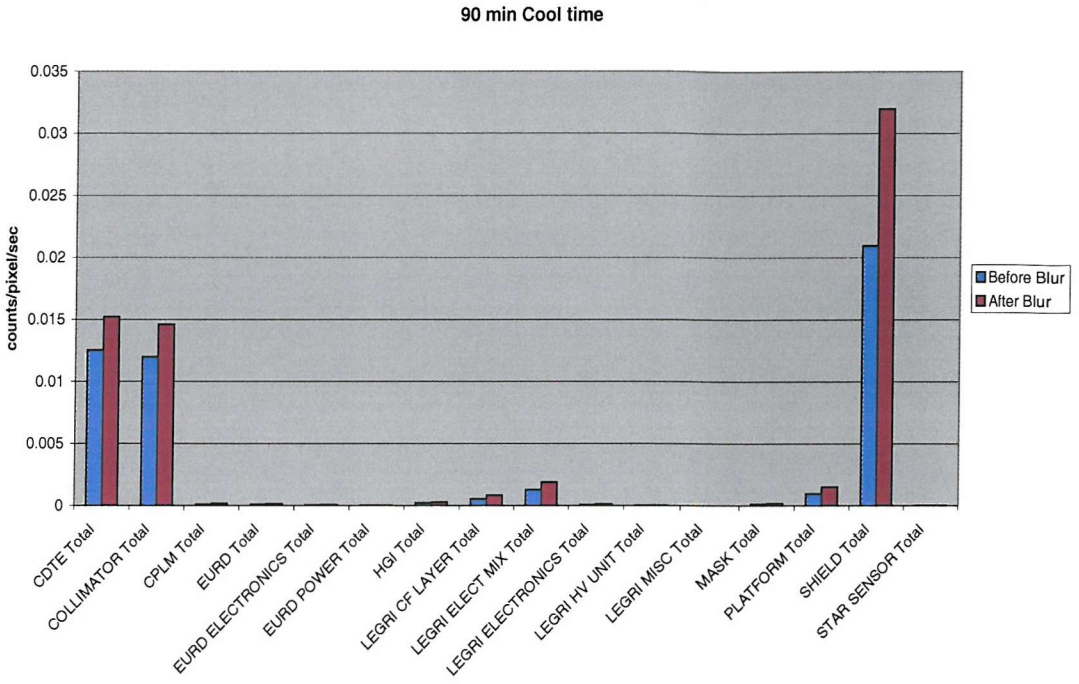

Figure 7.17: The background noise 90 minutes after an SAA pass split by volume

they are far away and most of the counts coming from these will be blocked by the shielding.

Figure 7.17 shows the volume contributions 90 minutes after the SAA pass. The shield, collimator and cadmium telluride are still the dominant contributors in approximately the same ratio to each other. Any other contributions at this stage are negligible.

To simplify this further figures 7.18 and 7.19 show the most significant volumes ie those contributing at least 10% of the maximum count rate from any one volume. Immediately after the SAA the lead shielding, cadmium telluride, and collimator give the highest count rates and only volumes within or in direct contact with the detector contribute at least 10% of the highest count rate. After 90 minutes the main contributors are again the cadmium telluride, collimator and lead shielding though in a different ratio to immediately after the SAA.

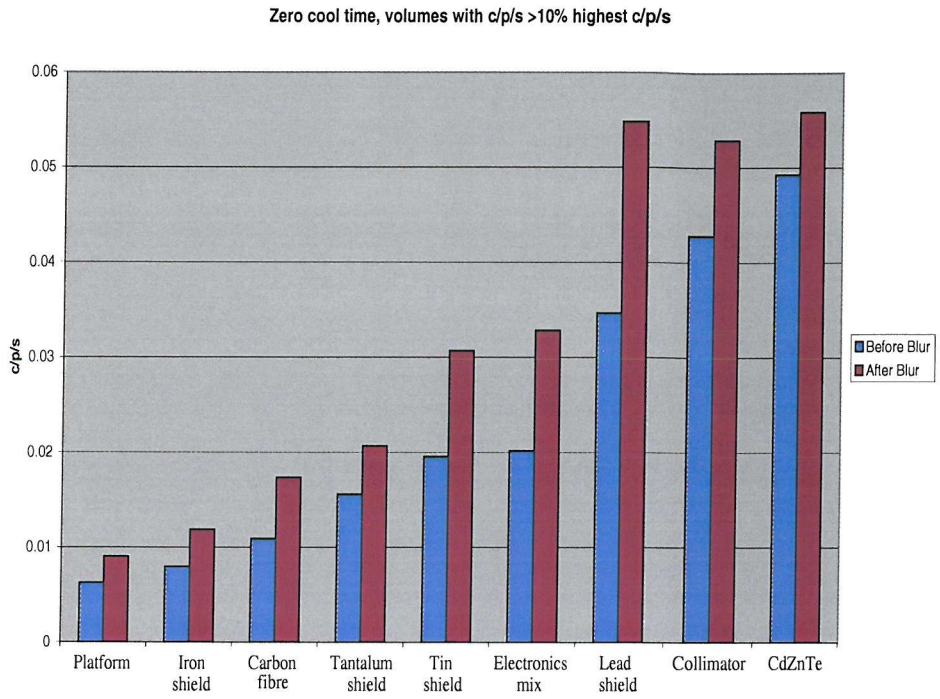

Figure 7.18: Volumes contributing > 10% of the highest count rate immediately after an SAA pass

7.6 Conclusions

Although the LEGRI detectors are turned off during a passage through the SAA there is still an increase in count rate afterwards due to activation of the spacecraft components. The count rate immediately after the simulated SAA pass increases by $\sim 0.6 \pm 0.06$ c/cm^2/s thus agreeing with observations. The decay of the count rate cannot be modelled by only two exponentials and an analysis of the internal sources of the background noise shows several isotopes contribute. The collimator, cadmium telluride and shielding are found to be the most significant volumes contributing both immediately after the SAA and 90 minutes later. The post SAA raw spectrum is similar to the pre SAA spectrum but has additional peaks due to electron capture on the cadmium telluride. The fluorescence peaks due to the tantalum collimator are clear in both pre and post SAA raw spectra. After a blurring algorithm is

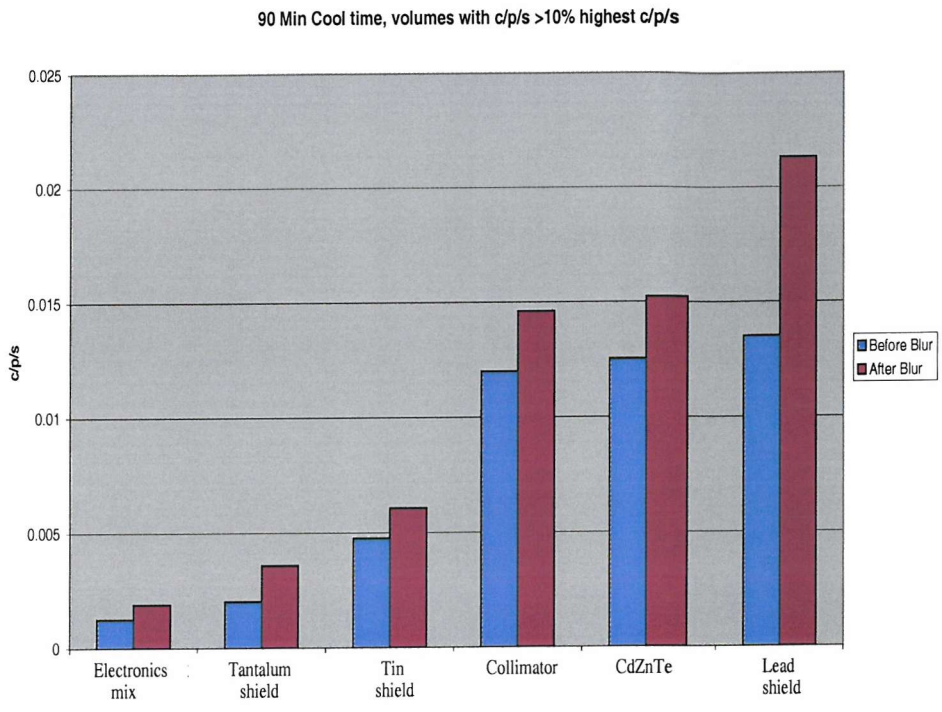

Figure 7.19: Volumes contributing > 10% of the highest count rate 90 minutes after an SAA pass

applied to account for charge trapping and energy resolution the two spectra are identical in shape.

Chapter 8

Modelling the effects of a solar flare on INTEGRAL

8.1 Introduction

8.1.1 The INTErnational Gamma Ray Astrophysics Laboratory

INTEGRAL (INTErnational Gamma Ray Astrophysics Laboratory) was selected by the ESA Science Programme Committee in 1993 as the next medium sized satellite in the Horizon 2000 programme. It will be launched in 2002 by a Russian Proton into a highly eccentric 72 hour orbit with inclination 51.6°. Observations can be made when the spacecraft is above 40,000 km. The lifetime of the satellite will be 2 years with a possible extension to up to 5 years. Figure 8.1 shows an artists impression of the INTEGRAL spacecraft with solar arrays deployed.

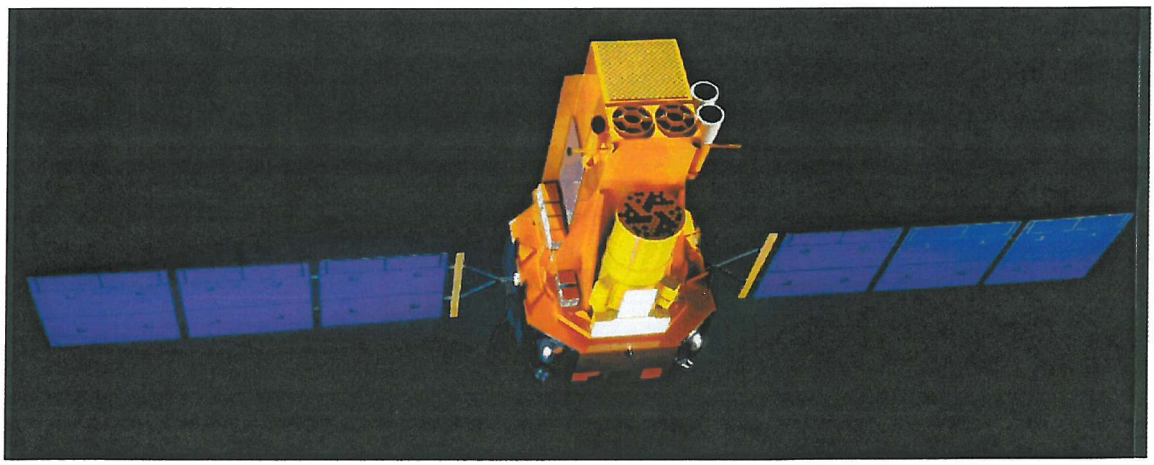

Figure 8.1: An artist's impression of the INTEGRAL spacecraft

Fine spectroscopy ($\frac{E}{\Delta E}$=500) and fine imaging (angular resolution: 12 arcmin FWHM) allow a broad range of scientific objectives for INTEGRAL. Topics that will be addressed include:

- Compact Objects (White Dwarfs, Neutron Stars, Black Hole Candidates)
- High Energy Transients
- The Galactic Centre
- Extragalactic Astronomy (Nearby Galaxies, Clusters, AGN)

Chapter 3 discusses these topics in more detail. In particular INTEGRAL, with its excellent resolving power, will be able to use line-forming processes such as nuclear excitation and positron annihilation as tools in unveiling new discoveries. The most recent high resolution space instrument, that on-board HEAO-3 in 1979-1980, was 100 times less sensitive than INTEGRAL.

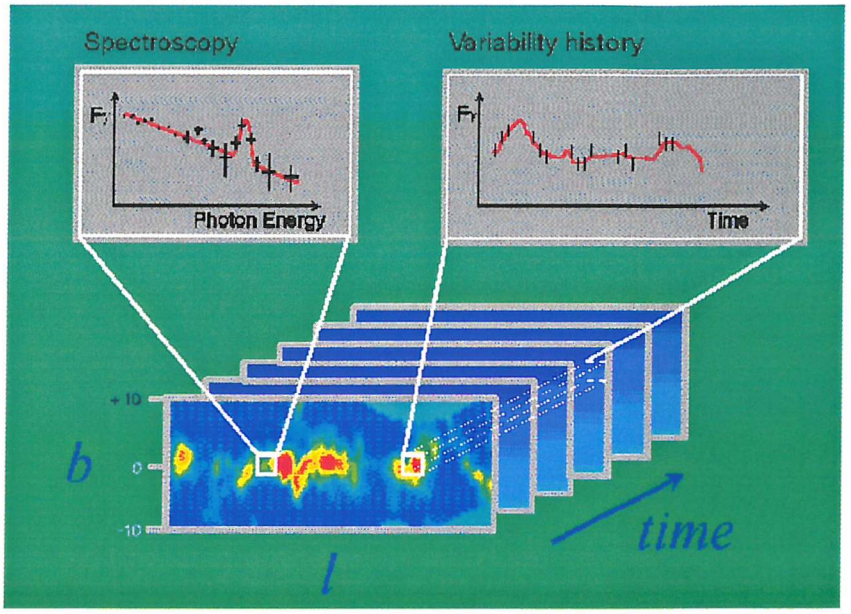

Figure 8.2: INTEGRAL will monitor the galactic plane for transient sources.

The γ-ray instruments on-board will be SPI (the spectrometer) and IBIS (the imager). The technical details of these are shown in table 8.1. There will also be an X-ray monitor (JEM-X) and an optical monitoring camera (OMC) to complement the γ-ray detectors. JEM-X monitors the sky over the energy range 3-35 keV and the OMC operates in the 500-850 nm band.

SPI will provide a spectral analysis of γ-ray point sources and diffuse line emission sources in the 20 keV - 8 MeV energy range. Figure 8.3 shows a slice through the SPI instrument. The coded mask consists of 63 hexagonal tungsten elements each 3cm thick. The detector plane has 19 hexagonal germanium bars (of global area 500 cm^2) surrounded by a BGO veto shield.

IBIS will provide imaging of celestial γ-ray sources in the energy range 15 keV - 10 MeV. Figure 8.4 shows a slice through the IBIS instrument. IBIS has two detector planes. The front layer, ISGRI, consists of 8 Modular Detection Units (MDU) each containing 2048 pixels of cadmium telluride (CdTe). The succeeding

	SPI	IBIS
Energy range	20 keV - 8 MeV	ISGRI: 15 keV - 1 MeV PICsIT : 100 keV - 10 MeV
Spectral resolution	2 keV @ 1.3 MeV	7 keV @ 100 keV
Field of View (fully coded)	16°	9° × 9°
Angular resolution (FWHM)	2°	12'
Continuum sensitivity*	7×10^{-8} @ 1MeV	4×10^{-7} @ 100 keV
Line sensitivity*	5×10^{-6} @ 1MeV	1×10^{-5} @ 100 keV
Mass (kg)	1309	628
* Sensitivities are 3σ in 10^6s, units: ph/(cm^2.s.keV) [cont.] and ph/(cm^2.s) [line]		

Table 8.1: Technical details of the INTEGRAL instruments SPI and IBIS.

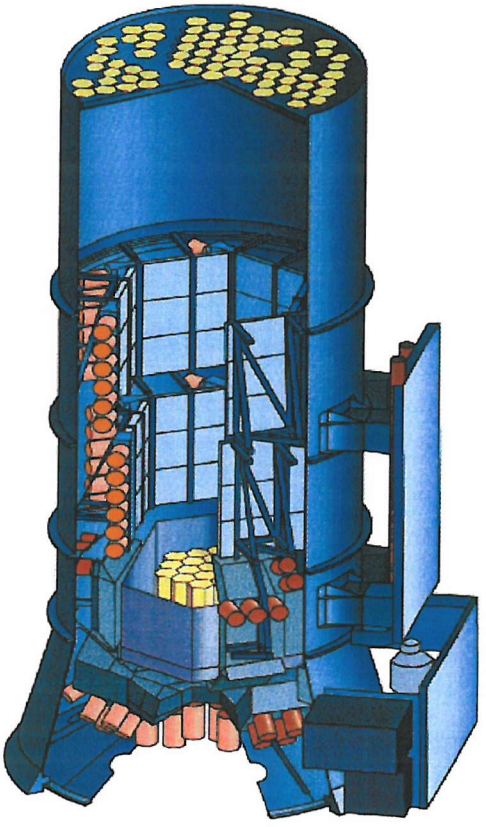

Figure 8.3: Cut-through view of the INTEGRAL spectrometer, SPI

layer, PICsIT, has 8 rectangular modules each containing 512 pixels of caesium iodide (CsI). The sensitive areas of ISGRI and PICsIT are 2621 cm^2 and 2994 cm^2 respectively. IBIS was originally designed with CsI alone. The CdTe was introduced in order to bridge the energy gap between the CsI and JEM-X. CdTe also has better spectral resolution than CsI. The detector system is surrounded by an active BGO veto system. The collimator contains a hopper, made of tungsten, and a tube with two walls made from tungsten and the other two forming part of the payload module. The coded mask is made from tungsten.

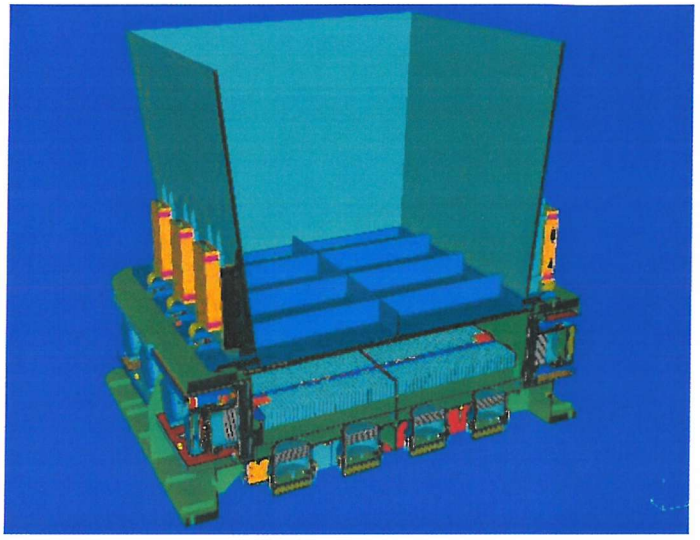

Figure 8.4: Cut-through view of the IBIS detector assembly and shield (hopper)

Unlike most other satellites INTEGRAL does not have a flight spare. The INTEGRAL Mass Model (TIMM) has therefore been constructed for post-launch trouble shooting as well as pre-launch instrument compatibility testing and background noise analysis. Figure 8.5 shows a wire diagram of TIMM. The complexity of the model, containing 46,024 volumes, can be seen.

Chapters 6 and 7 show the design and use of the LEGRI mass model to analyse both the static and dynamic background noise. Simulations of this kind have already been performed for INTEGRAL [40] but due to the timing and orbit of this satellite there is another type of background noise that should be taken into account. The sun enters a phase of high activity during 2001 and solar flares are likely to emit large numbers of charged particles. Thus at any time INTEGRAL could be subjected to an intense solar flare radiation environment. The subject of this chapter is to gain a better understanding of solar flares and the effects they could have on the instruments on-board INTEGRAL. The next section gives an introduction to solar flares and subsequent sections provide an analysis of solar flare background noise for INTEGRAL.

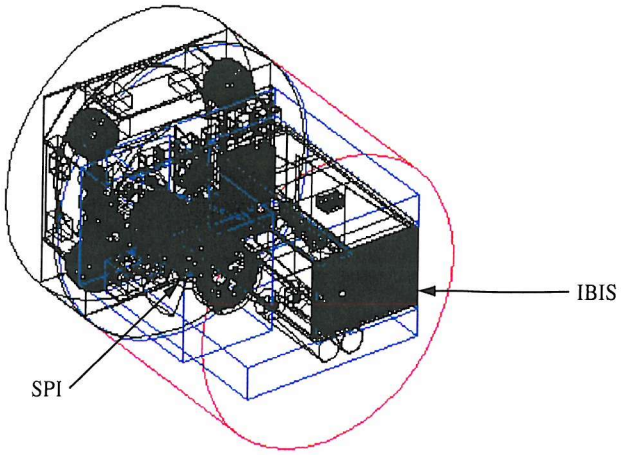

Figure 8.5: Wire diagram of The INTEGRAL Mass Model.

8.2 Solar Flares

The sun undergoes an 11 year cycle during which there is a period of high activity when solar flares are more common. The current period of high activity started in 2001 and will last for several years during which INTEGRAL will be observing. Solar flares are sudden releases of energy from the sun as a result of a build up of magnetic energy. There are three stages to a solar flare as follows (http://hesperia.gsfc.nasa.gov/sftheory):

- Precursor stage. The release of magnetic energy is triggered and soft x-ray emission can be detected.
- Impulsive stage. Protons and electrons are accelerated to energies exceeding 1 MeV. Radio waves, hard x-rays and γ-rays are emitted.
- Decay stage. A gradual build up and decay of soft x-rays.

The left frame of figure 8.6 shows an image of a solar flare in soft x-rays taken with the Yohkoh Soft X-ray Telescope (SXT). The right frame is a magnified flare with a map of hard x-ray emission superimposed on the soft x-ray map. The flare has a simple loop structure and the magnetic field lines can be seen (http://hesperia.gsfc.nasa.gov/sftheory/flareimage.htm).

Solar flares radiate at many frequencies from γ-rays to radio waves and they also emit solar cosmic rays consisting of protons, electrons and atomic nuclei. Most of the particles observed are protons. Alpha particles may also be seen but the electrons lose most of their energy in exciting radio bursts in the sun's corona. This chapter deals solely with the effects of the solar cosmic ray protons since these are the most abundant particles.

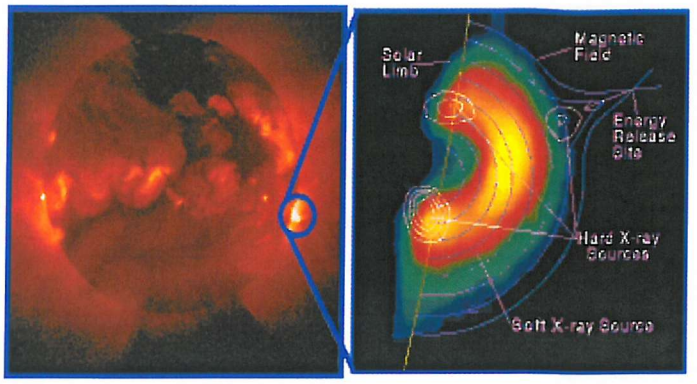

Figure 8.6: Image of a solar flare in hard and soft x-rays (http://hesperia.gsfc.nasa.gov/sftheory/flareimage.htm)

8.3 Solar flare radiation environment

The orbit of INTEGRAL may expose the detectors on board to an extremely intense proton flux due to a solar flare. Solar flares vary greatly in intensity and duration and it is therefore difficult to generalise or even to chose a typical solar flare to simulate.

The event chosen occurred in March 1991 and the corresponding proton spectrum varied over a period of 5 to 6 days. This particular flare was chosen as it is well documented and is a flare of "reasonable" intensity and duration.

Constant Flux Model

Our preliminary simulations used figure 8.7 (at the time of arrival of shock 2) to simplify the flux to a constant 2.51×10^5 $E^{-3.4}$ protons/cm^2/s/sr/MeV over a period of five days. The total integrated flux of this simulated flare is equal to that of the observed flare (1.5×10^{14} protons) [53],[58].

Variable Flux Model

The flare has since been more accurately modelled by assuming a variable flux over ~5 days again with the same total integrated flux as the observed flare. Figure 8.8 was used to break down the proton flux into the following:

- Day 0: α = -3.5 (α = spectral index), duration = 7 hours, flux = 22 protons/cm^2/sec
- Day 1: α = -4.5, duration = 24 hours, flux = 579 protons/cm^2/sec
- Day 2: α = -4.5, duration = 24 hours, flux = 347 protons/cm^2/sec
- Day 3: α = -4.5, duration = 24 hours, flux = 173 protons/cm^2/sec
- Day 4: α = -4.5, duration = 24 hours, flux = 86 protons/cm^2/sec
- Day 5: α = -4.5, duration = 24 hours, flux = 43 protons/cm^2/sec

Figure 8.9 shows the input proton flux of the variable flux model.

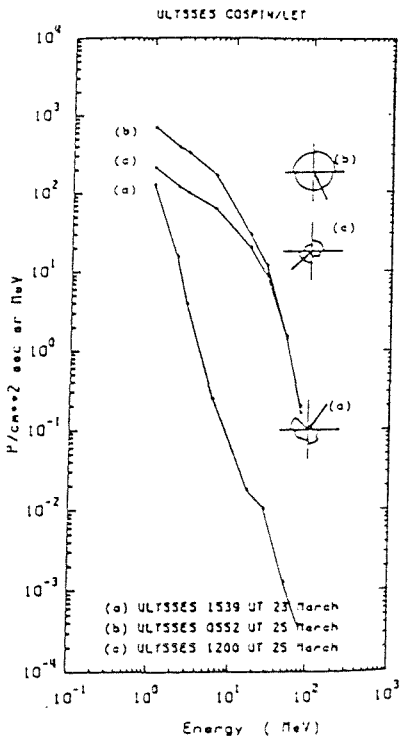

Figure 8.7: Spectra observed at Ulysses (a) at the time of arrival of shock 1 (b) at the time of arrival of shock 2 and (c) during the passage of a magnetic cloud.

8.4 Monte-Carlo simulations of the March 1991 solar flare

Over a billion protons were fired in from a cylinder surrounding the INTEGRAL spacecraft. As in Chapters 6 and 7 for LEGRI the time equating to this number of protons was calculated and used as a scaling factor before producing the isotope production rates and isotope decay rates. The isotope decay rates are then passed in to the second Monte-Carlo as explained in Chapter 4. In the variable flux model the second Monte-Carlo must be run separately for each of days 0-5 and also for each cooling time (see Chapter 4). Thus 54 separate Monte-Carlo 2s were required. This was the main reason for our first approximation of a constant flux where only one Monte-Carlo 2 was required for each cooling time (a total of 9 Monte-Carlo 2s).

Constant Flux Model

As discussed in the previous section the constant flux model assumed a flux of 2.51 $\times$ 10^5 $E^{-3.4}$ protons/cm^2/s/sr/MeV over a period of 5 days. After the end of the flare cooling times of 1 min, 10 min, 30 min, 60 min, 2 hr, 6 hr, 24 hr were used in order to build up a profile of how the count rate declines after the end of the flare. Such a profile for each instrument is shown in figure 8.10. In order to maximise the efficiency of future simulations the constant flux model was split into several different input energy bands. Each of the input energy bands had an upper limit of 2 GeV but different lower energy limits as follows: 10 MeV, 30 MeV, 50 MeV

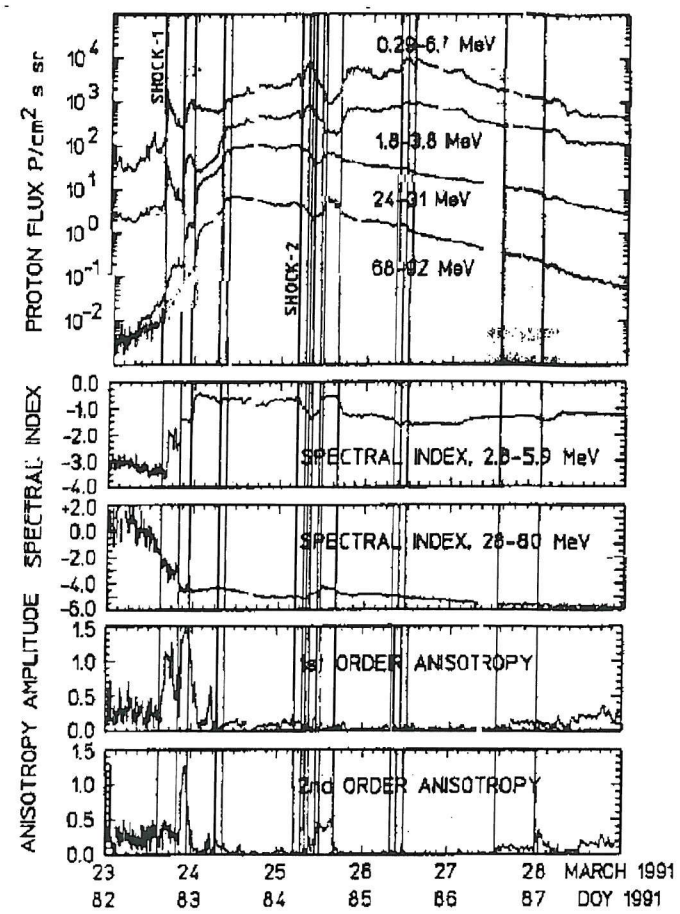

Figure 8.8: Time intensity profiles as observed with the COSPIN instrument, together with spectral indices

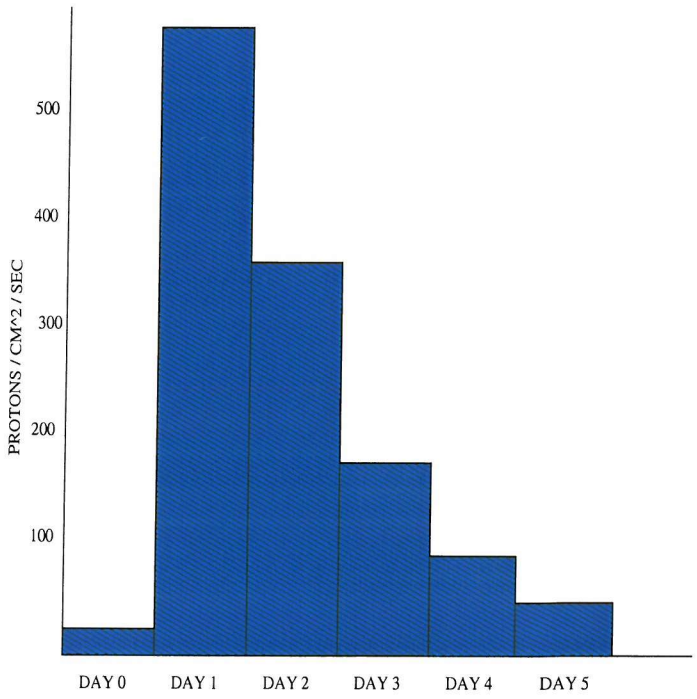

Figure 8.9: The solar flare variable flux model

and 100 MeV. The resulting count rates from the 10 MeV and 30 MeV simulations are identical and there is, therefore, no need in future simulations to extend the energy band down to 10 MeV. Protons in the energy range 10 MeV - 30 MeV are stopped by the spacecraft and detector shielding and are therefore not detected and do not increase the count rate. There is a difference in the count rates of the 30 MeV and 50 MeV simulations and protons in the band 30 - 50 MeV do contribute to the background noise. The ideal input proton energy range is therefore 30 MeV - 2GeV. The spectrum is steep enough that there are very few protons > 2 GeV and this is therefore a good upper limit.

The decay profiles in figure 8.10 show the declining count rates for each instrument:

- SPI: The count rate declines from $\sim$ 190 counts / second 1 minute after the end of the flare to $\sim$ 60 counts / second 24 hours after the flare. Thus up to a third of the radiation is still decaying a day later.
- ISGRI: The count rate declines from $\sim$ 530 counts / second 1 minute after the end of the flare to $\sim$ 140 counts / second 24 hours later. Approximately 20% of the activity is therefore remaining a day later.
- PICsIT: The count rate declines from $\sim$ 3300 counts / second 1 minute after the end of the flare to $\sim$ 800 counts / second. Again approximately 20% of the activity is therefore remaining a day later.

Figure 8.11 shows the spectrum for each instrument one minute after the end of the flare. The SPI and ISGRI spectra are binned into 1 keV bins. PICsIT has much poorer energy resolution (see table 8.1) and 10 keV binning is therefore sufficient. Many spectral lines can be seen and these are due to isotopes decaying and emitting characteristic x-rays. A full analysis of spectral lines is discussed for the variable flux model in the next section.

Variable Flux Model

The variable flux model attempts to simulate the solar flare more realistically by using a variable input proton flux over a period of 5 to 6 days. After the end of the flare cooling times of 1 min, 10 min, 30 min, 60 min, 2 hours, 6 hours, 24 hours, 48 hours and 96 hours were used to build up a profile of count rate versus time for each instrument. These profiles are shown in figure 8.12 and are summarised below:

- SPI: The count rate declines from $\sim$ 10 counts / second 1 minute after the end of the flare to $\sim$ 2 counts / second 96 hours later.
- ISGRI: The count rate declines from $\sim$ 70 counts / second 1 minute after the end of the flare to $\sim$ 25 counts / second 96 hours later.
- PICsIT: The count rate declines from $\sim$ 280 counts / second 1 minute after the end of the flare to $\sim$ 100 counts / second 96 hours later.

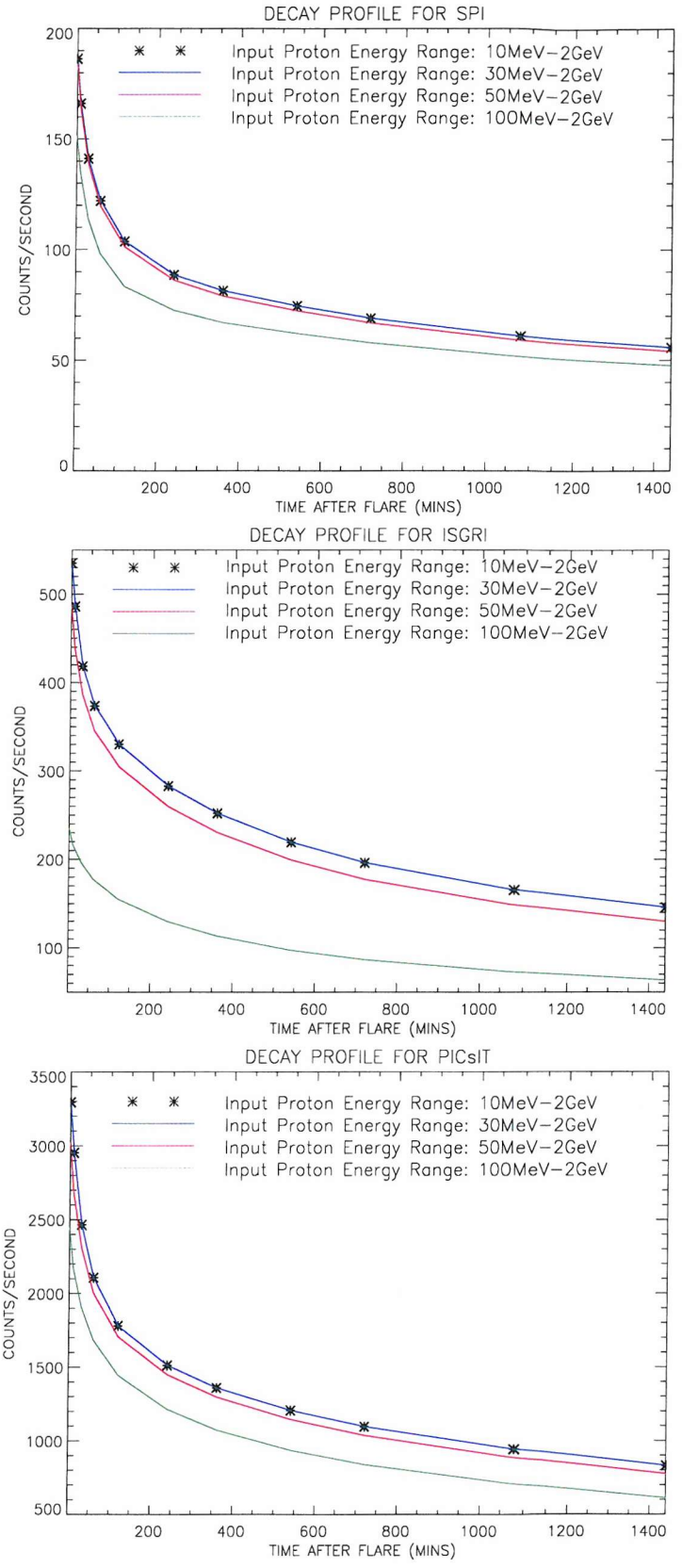

Figure 8.10: Constant flux model: Decay profiles (count rate versus time) for SPI, ISGRI and PICsIT up to 24 hours after the end of the flare

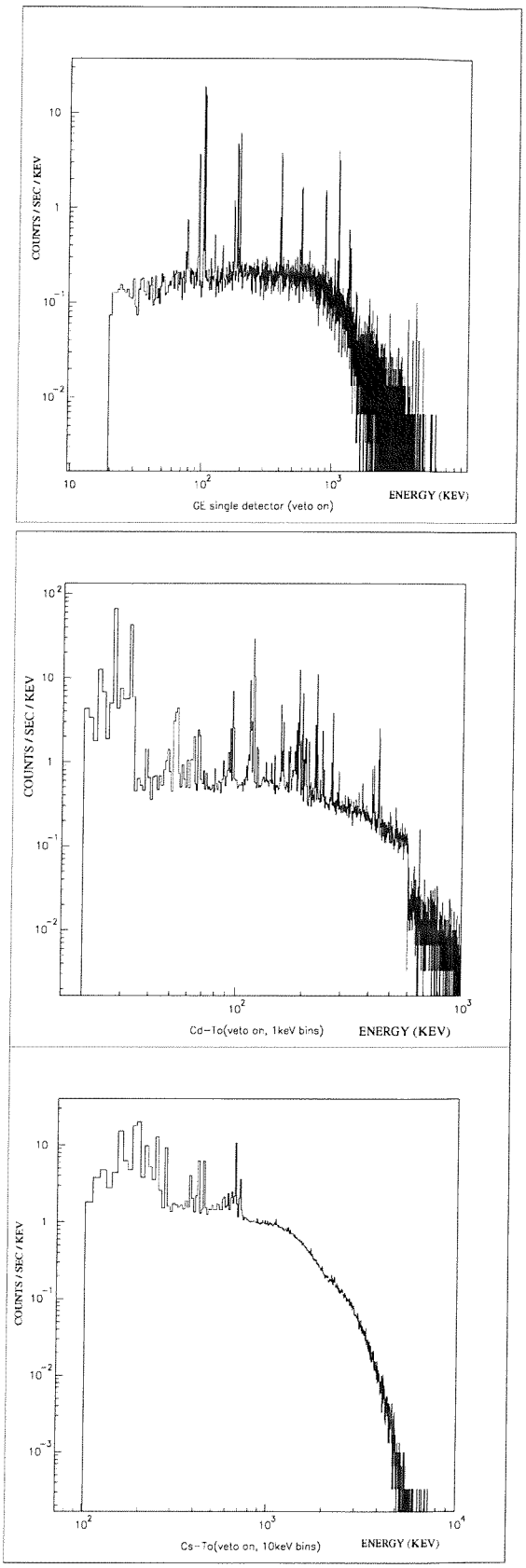

Figure 8.11: Constant flux model: Spectra one minute after the end of the flare for SPI, ISGRI and PICsIT

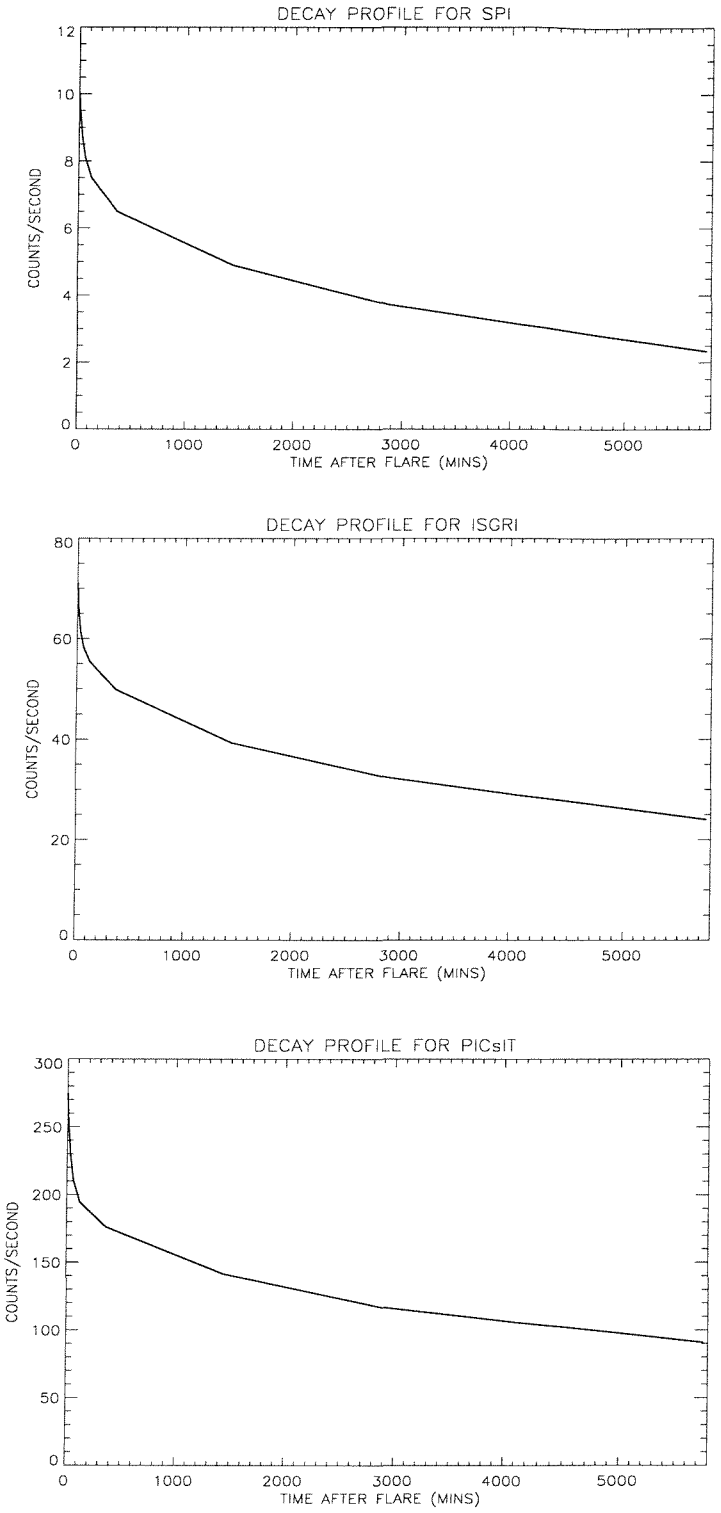

Figure 8.12: Variable flux model: Decay profiles (count rate versus time) for SPI, ISGRI and PICsIT up to 4 days after the end of the flare

The count rates one minute after the end of the flare for the variable flux model are approximately one tenth of the constant flux model count rates. The integrated flux for each model was equated to that calculated from [58] but two different figures were used for the calculations (figure 8.7 for the constant flux model and figure 8.8 for the variable flux model). Thus the total integrated flux for the variable flux model (1.0×10^{14} protons) is in fact lower than the total integrated flux for the constant flux model (1.5×10^{14} protons). Another important characteristic of the variable flux model is the way in which the protons are fired in. As shown in figure 8.9 nearly 50% of the total proton flux is fired in on Day 1 and only $\sim$ 10% of the total flux is fired in on days 4 and 5. Isotopes activated on day 1 can decay at least in part before the end of the flare. The count rates seen one minute after the end of the flare are due to long lived isotopes activated on days 1 and 2 and a mixture of short and long lived isotopes from the lower input flux days 3, 4 and 5. This has the effect of lowering the count rates seen after the end of the flare.

Figure 8.13 shows the spectrum for ISGRI one minute, one hour, one day, two days and four days after the end of the flare. The spectral shape does not appear to evolve over this period and even the relative intensities of many of the lines remain the same.

Table 8.2 shows the spectral lines one minute after the end of the flare. Most of the lines are due to electron capture on indium or iodine. The ISGRI detector plane contains cadmium and tellurium (CdTe). The most likely processes occurring are therefore proton capture on cadmium and tellurium resulting in indium and iodine respectively. These isotopes then decay by electron capture producing their characteristic x-rays.

To illustrate these processes the following has been taken as an example:

- Proton capture on ^{110}Cd: $^{110}\mathrm{Cd} + \mathrm{p} \rightarrow {}^{111}\mathrm{In}$
- Electron capture on ^{111}In: $^{111}\mathrm{In} \rightarrow {}^{111}\mathrm{Cd} + \nu$
- Electron capture on ^{111}In produces lines at 171.28, 245.35 and 416.70 keV
- Electrons move from K to L_3 shell ($K\alpha_1$) and produce x-rays at 195.49, 269.56 and 440.91 keV (original x-ray energies plus K-L_3 shell binding energy)
- Electrons move from L_3 to M_5 ($L\alpha_1$) and produce x-rays at 174.56, 248.63 and 419.98 keV (original x-ray energies plus L_3 - M_5 shell binding energy)

Table 8.2 shows that some of the lines are also produced by β^{-1} decay and IT decay as follows:

- β^{-1} decay: $^{126}\mathrm{Sb} \rightarrow {}^{126}\mathrm{Te} + \mathrm{e}^-$ produces lines at 414.8, 666.3 and 697.0 keV
- IT decay: Isomeric transition of ^{114}In from excited to stable state produces a line at 190.27 keV (half-life of 49.5 days)

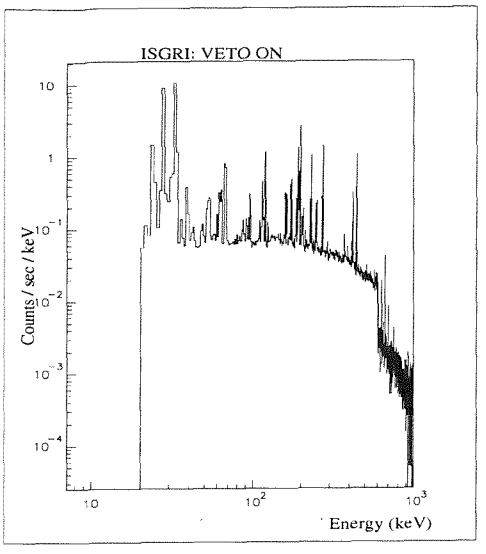

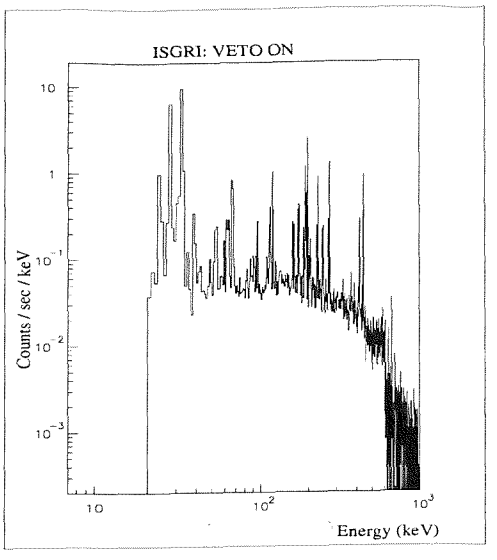

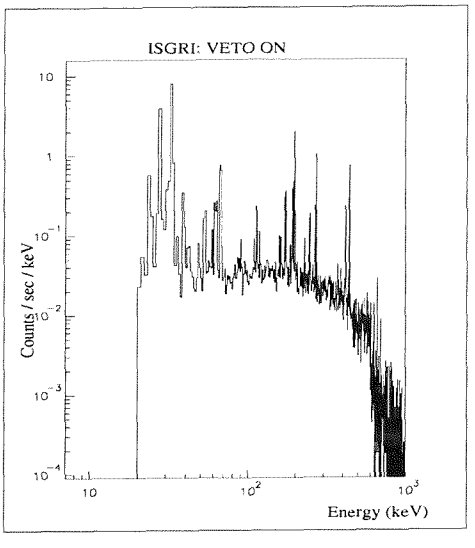

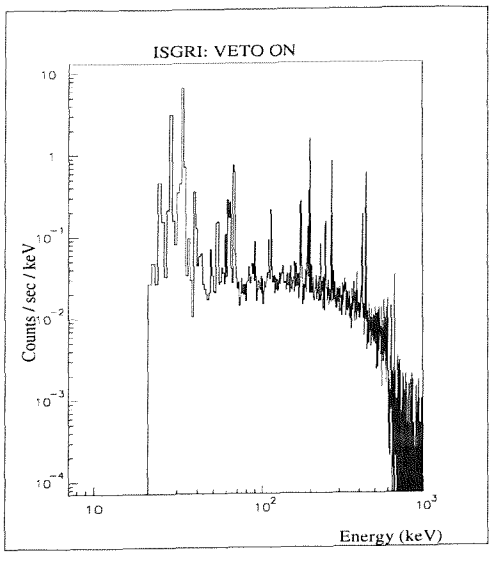

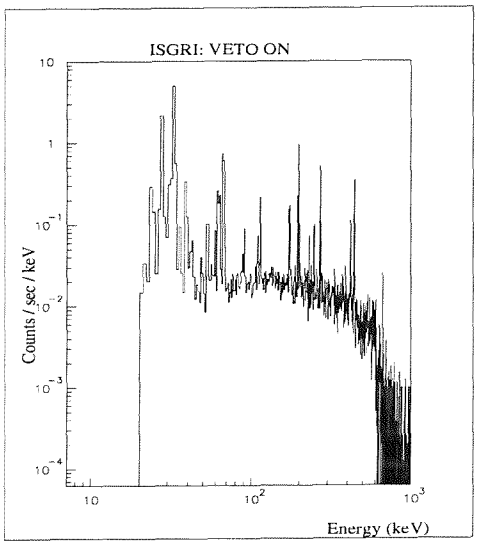

Figure 8.13: Variable flux, 1 keV bins. Spectrum detected in ISGRI one minute, one hour, one day, two days and four days (from left to right) after the end of the flare.

Isotope	Line Energy (keV)	Decay scheme
^{111}In	171.28	Electron capture
	245.35	Electron capture
	416.70	Electron capture
^{111}In	195.49	Kα_1
	269.56	Kα_1
	440.91	Kα_1
^{111}In	174.56	Lα_1
	248.63	Lα_1
	419.98	Lα_1
^{114}In	190.27	IT decay
^{119}Sb	23.87	Electron capture
	50.22	Kα_1
	27.47	Lα_1
^{123}I	159.10	Electron capture
	439.7	Electron capture
	687.88	Electron capture
	697.55	Electron capture
^{125}I	35.49	Electron capture
	64.10	Kα_1
	67.78	Lα_1
^{126}I	666.33	Electron capture
	694.94	Kα_1
^{126}Sb	414.8	β^{-1} decay
	666.3	β^{-1} decay
	697.0	β^{-1} decay
^{129}Te	695.88	β^{-1} decay

Table 8.2: Lines seen in the ISGRI spectrum (one minute after the end of the flare) and the isotopes causing them

Figure 8.14 shows the spectra for PICsIT one minute, one hour, one day, two days and four days after the end of the flare. The binning has been changed to log binning in order to represent the spectra actually detected by the CsI during flight. The spectral shape remains approximately the same for up to 4 days after end of the flare.

The spectra for SPI are shown in figure 8.15. Again the spectral shape shows little evolution for up to 4 days after the end of the flare and the relative intensities of the lines seems to remain the same.

Table 8.3 shows the spectral lines for SPI one minute after the end of the flare. As with ISGRI, electron capture is the dominant decay process producing the lines. This is illustrated as follows:

- Electron capture on ^{69}Ge: $^{69}\text{Ge} \rightarrow {}^{69}\text{Ga} + \nu$ produces lines at 574.21, 872.13 and 1107.03 keV

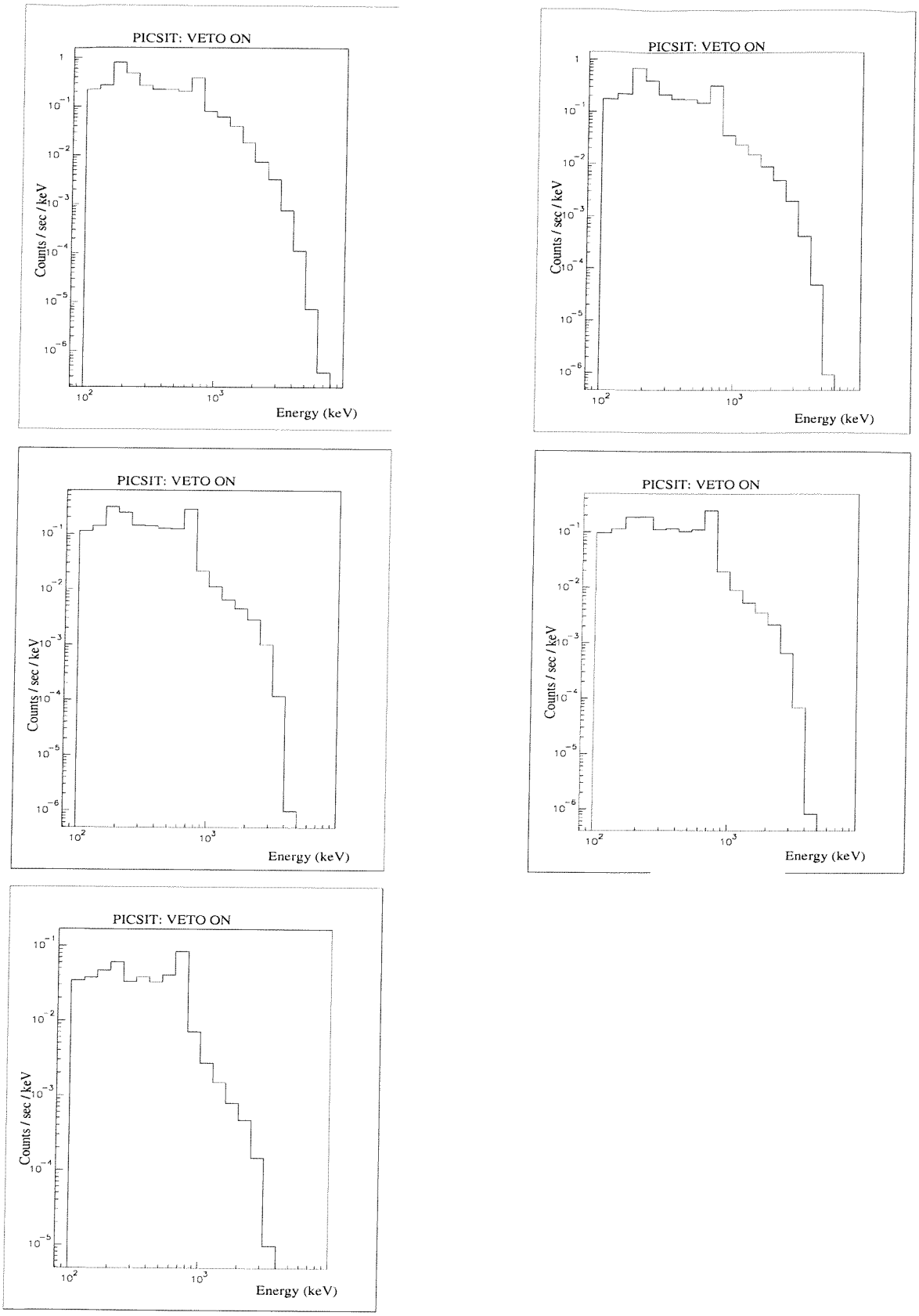

Figure 8.14: Variable flux, log bins. Spectrum detected in PICsIT one minute, one hour, one day, two days and four days (from left to right) after the end of the flare.

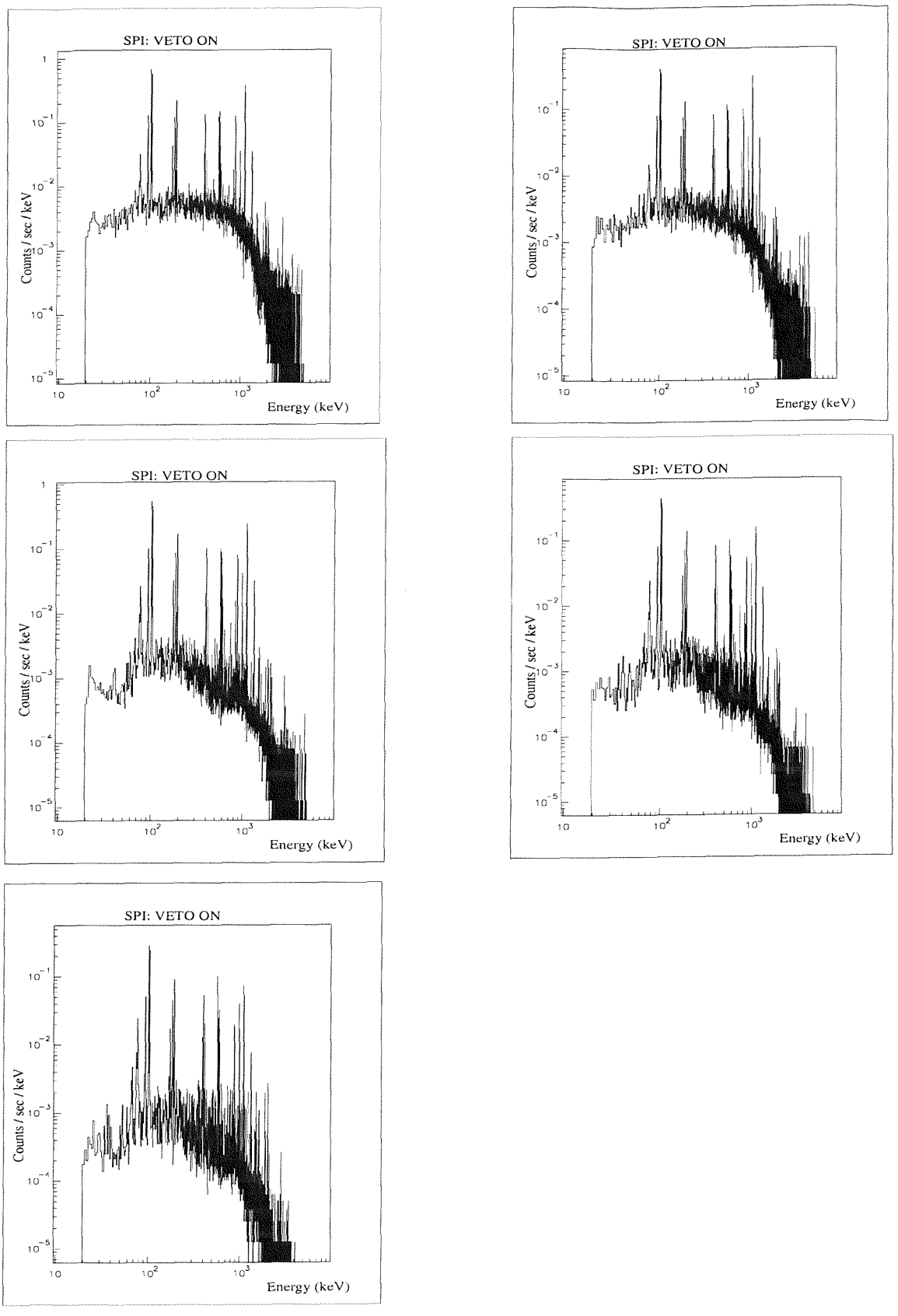

Figure 8.15: Variable flux, 1 keV bins. Spectrum detected in SPI one minute, one hour, one day, two days and four days (from left to right) after the end of the flare.

Isotope	Line Energy (keV)	Decay scheme
^{67}Ga	93.31	Electron Capture
	184.57	Electron Capture
	393.53	Electron Capture
^{67}Ga	102.56	Kα_1 transition
	193.83	Kα_1 transition
	402.78	Kα_1 transition
^{67}Ga	102.53	Kα_2 transition
	193.80	Kα_2 transition
	402.75	Kα_2 transition
^{69}Ge	574.21	Electron Capture
	872.13	Electron Capture
	1107.03	Electron Capture
^{69}Ge	584.09	Kα_1 transition
	882.01	Kα_1 transition
	1116.91	Kα_1 transition
^{67}Ge	584.06	Kα_2 transition
	881.98	Kα_2 transition
	1116.88	Kα_2 transition
^{71}As	174.94	Electron Capture
	185.49	Kα_1 transition
	185.45	Kα_2 transition

Table 8.3: Lines seen in the SPI spectrum (one minute after the end of the flare) and the isotopes causing them

- Kα_1 transition produces lines at 584.06, 882.01 and 1116.91 keV.

8.5 Conclusions

Two models were used to simulate the effects of a solar flare on the instruments onboard INTEGRAL. The solar flare occurred in March 1991 and was approximated first by a constant flux over a period of 5 days (the constant flux model) and then more accurately by a variable flux over a period of 5 - 6 days (the variable flux model). The count rates for the variable flux model were approximately one tenth of the count rates for the constant flux model. This is due to a lower integrated input proton flux for the variable flux model and the decline of the input flux in days 3, 4 and 5 allowing activated isotopes to decay before the end of the flare. The count rates one minute after the end of the flare for the variable flux model were $\sim$ 10 counts / sec for SPI, $\sim$ 70 counts / sec for ISGRI and $\sim$ 280 counts / sec for PICsIT. This compares to an estimated static solar maximum background count rate of $\sim$ 244 counts / sec for SPI, $\sim$ 423 counts / sec for ISGRI and $\sim$ 1048 counts / sec for PICsIT [39]. Thus the solar flare modelled increases the total background count rate one minute after the end of the flare to approximately that expected during solar minimum [39]. It should be remembered however that solar flares vary

greatly in intensity and duration and actually during the flight far greater effects could be experienced. The solar flare background count rates decayed over a period of 96 hours to $\sim$ 2 counts / sec, $\sim$ 25 counts / sec and $\sim$ 100 counts / sec for SPI, ISGRI and PICsIT respectively. The spectra for each of the instruments were similar in shape for each model and for periods of up to several days after the end of the flare. Many line features can be seen in the spectra for SPI and ISGRI and these are found to be mainly due to electron capture on, for example, indium or germanium isotopes.

Chapter 9

Conclusions

The basis of this thesis has been the use of Monte-Carlo simulations to model the background noise in γ-ray satellites. A perfect example of the type of study that background modelling is designed to enhance is provided in the study of classical novae. The hard x-ray emissions from these sources are too faint to be detected by the BATSE Earth Occultation Technique alone but the improvements in sensitivity gained through the subtraction of the background model could allow detections at these wavelengths to be made. Future work may, therefore, include the flat fielding of the BATSE data once the background model has been fully implemented. Furthermore one of the objectives of INTEGRAL, due to be launched in 2002, is to search for classical novae at γ-ray energies. As with BATSE, the INTEGRAL background model can be used to increase the sensitivity of the instruments even after the observations have been made.

Monte Carlo techniques are then used to simulate the background noise in LEGRI (Low Energy Gamma Ray Imager) onboard the Minisat-01 satellite. Initially comparisons between actual and simulated observations are made so that further information can be reliably obtained from the simulated spectra and count rates. The simulated count rate increases from ~ 0.42 c/cm^2/s at the equator to ~ 0.71 c/cm^2/s at the poles. These count rates are slightly lower than those observed due to the effects of charge trapping and energy resolution which are not taken into account at this stage. In spite of this the observed count rates of ~ 0.5 c/cm^2/s and ~ 0.75 c/cm^2/s at the equator and poles respectively *are* in excellent agreement with our simulations. This increase in count rate is due to the effects of geo-magnetic cut-off on the cosmic ray and atmospheric background components. The cosmic ray component accounts for more than 60% of the total count rate at the equator and more than 70% at the poles. The simulated spectra show significant peaks at ~ 56, 57 and 65 keV due to fluorescence from the tantalum collimator.

The next chapter studies the effects of an observed and simulated SAA pass on LEGRI. Although the LEGRI detectors are turned off during a passage through

the SAA there is still an increase in count rate afterwards due to activation of the spacecraft components. The count rate immediately after the simulated SAA pass increases by $\sim$ 0.6 c/cm^2/s thus agreeing with observations. The decay of the count rate cannot be modelled by only two exponentials and an analysis of the internal sources of the background noise shows several isotopes contribute. The collimator, cadmium telluride and shielding are found to be the most significant volumes contributing both immediately after the SAA and up to 90 minutes later. The post SAA raw spectrum is similar to the pre SAA spectrum but has additional peaks due to electron capture on the cadmium telluride. The fluorescence peaks due to the tantalum collimator are clear in both pre and post SAA raw spectra. After a blurring algorithm is applied to account for charge trapping and energy resolution the two spectra are identical in shape.

Finally the last chapter uses two different models to simulate the effects of a solar flare on the instruments onboard INTEGRAL. The solar flare chosen occurred in March 1991 and was first approximated by a constant flux over a period of 5 days (the constant flux model) and then more accurately by a variable flux over a period of 5 - 6 days (the variable flux model). The count rates for the variable flux model were approximately one tenth of the count rates for the constant flux model. This is due to a lower integrated input proton flux for the variable flux model and the decline of the input flux in days 3, 4 and 5 allowing activated isotopes to decay before the end of the flare. The count rates one minute after the end of the flare for the variable flux model were $\sim$ 10 counts / sec for SPI, $\sim$ 70 counts / sec for ISGRI and $\sim$ 280 counts / sec for PICsIT. This compares to an estimated static solar maximum background count rate of $\sim$ 244 counts / sec for SPI, $\sim$ 423 counts / sec for ISGRI and $\sim$ 1048 counts / sec for PICsIT [39]. Thus the solar flare modelled increases the total background count rate one minute after the end of the flare to approximately that expected during solar minimum [39]. It should be remembered however that solar flares vary greatly in intensity and duration and actually during the flight far greater effects could be experienced. The solar flare background count rates decayed over a period of 96 hours to $\sim$ 2 counts / sec, $\sim$ 25 counts / sec and $\sim$ 100 counts / sec for SPI, ISGRI and PICsIT respectively. The spectra for each of the instruments were similar in shape for each model and for periods of up to several days after the end of the flare. Many line features can be seen in the spectra for SPI and ISGRI and these are found to be mainly due to electron capture on, for example, indium or germanium isotopes.

Bibliography

[1] S. Balman, J. Krautter, and H. Ogelman. "the x-ray spectral evolution of classical nova v1974 cygni 1992: A reanalysis of the rosat data". *ApJ*, 499:395, 1998.

[2] S.D. Barthelmy, L.M. Bartlett, N. Gehrels, M. Leventhal, B.J. Teegarden, J. Tueller, S. Belyaev, V. Lebedev, and H.V. Klapdor-Kleingrothaus. "gris background reduction results using isotopically enriched ge". *ApJ*, 427:519, 1994.

[3] R.D. Blandford and M.J. Rees. "A Twin Exhaust model for double radio sources". *MNRAS*, 169:395, 1974.

[4] E. Blucher, B. Gittelman, B.K. Heltsley, J. Kandaswamy, R. Kowalewski, Y. Kubota, N. Mistry, S. Stone, and A. Bean. "Tests of cesium iodide crystals for an electromagnetic calorimeter". *NIM*, A249:201, 1986.

[5] M. Boezio, P. Carlson, and T. Francke et al. "The Cosmic Ray Proton and Helium Spectra between 0.4 and 200 GV". *ApJ*, 518:457, 1999.

[6] S. Brandt, N. Lund, and A.R. Rao. "The Watch all-sky monitor for the GRANAT project". *AdSpR*, 10:239, 1990.

[7] James H. Buckley. "Gamma Ray Astronomy". In *Proceedings of the 26th International Cosmic Ray Conference*, 1999.

[8] Compton Gamma Ray Observatory Science Support Centre. "2704 BATSE Gamma-Ray Bursts". In *http://cossc.gsfc.nasa.gov/cossc/batse/*, 2000.

[9] K.S. Cheng and T. Lu. "Gamma-Ray Bursts: Afterglows and Central Engines". *ChJAA*, 1:1, 2001.

[10] J. Chiang and R. Mukherjee. "The luminosity function of the EGRET gamma-ray blazars". *ApJ*, 496:752, 1998.

[11] G. Conti, L. Chiappetti, S. Molendi, B. Sacco, G. Cusumano, G. La Rosa, M.C. Maccarone, T. Mineo, G. Boella, and O. Citterio. "in-flight performances of grazing incidence x-ray optics on board the x-ray astronomy satellite bepposax". *SPIE*, 3113:394, 1997.

[12] E. Costa, F. Frontera, J. Heise, M. Feroci, J. in't Zand, F. Fiore, M. N. Cinti, D. dal Fiume, L. Nicastro, M. Orlandini, E. Palazzi, M. Rapisarda, G. Zavattini, R. Jager, A. Parmar, A. Owens, S. Molendi, G. Cusumano, M.C.

Maccarone, S. Giarrusso, A. Coletta, L.A. Antonelli, P. Giommi, J.M. Muller, L. Piro, and R.C. Butler. "Discovery of an X-ray afterglow associated with the gamma-ray burst of 28 February 1997". *Nature*, 387:783, 1997.

[13] A.J. Dean, A. Bellomo, P. Coffarom, M. Fatta, G. Gerardi, F. Madonia, A. Russo, and L. Scarsi. "An experiment to Measure the Direction and Energy Spectrum of Extraterrestrial Gamma Rays in the Energy Range 1-10MeV from Balloon Altitudes". *IAUS*, 41:63D, 1971.

[14] A.J. Dean, F. Lei, and P.J. Knight. "Background in Space Borne Low Energy γ-ray Telescopes". *Space Science Rev*, 57:109, 1991.

[15] R.A. Downes, R.F. Webbink, and M.M. Shara. "a catalog and atlas of cataclysmic variables - 2nd edition". *PASP*, 109:345, 1997.

[16] G. J. Fishman, C.A. Meegan, R.B. Wilson, W.S. Paciesas, T.A. Parnell, R.W. Austin, J.R. Rehage, J.L. Matteson, B.J. Teegarden, T.L. Cline, B.E. Schaefer, G.N. Pendleton, Jr. F.A. Berry, J.M. Horack, S.D Storey, M.N Brock, and J.P Lestrade. "BATSE: The Burst and Transient Source Experiment on the Gamma Ray Observatory". In *Proceedings of the First Compton Symposium*, 1989.

[17] N. Gehrels. "instrumental background in balloon-borne gamma-ray spectometers and techniques for its reduction". *NIM*, A239:324, 1985.

[18] N. Gehrels, T.L. Cline, B.J. Teegarden, J. Tueller, M. Leventhal, C.J. MacCallum, and P. Ryge. "Development of a segmented n-type germanium detector and its application to astronomical gamma-ray spectroscopy". In *The Nucl. Sci. Symposium, San Francisco 1983*, 1983.

[19] N. Gehrels, C.J. Crannell, D.J. Forrest, R.P. Lin, L.E. Orwig, and R. Starr. "Hard X-ray and Low Energy Gamma Ray Spectrometers". *Solar Physics*, 118:223, 1988.

[20] N. Gehrels, C.E. Fichtel, G.J. Fishman, J.D. Kurfess, and V. Schonfelder. "The Compton Gamma-Ray Observatory". *Sci. Am.*, 269:68, 1993.

[21] N. Gehrels and C. Shrader. "Status and Future of the Compton Gamma Ray Observatory". In *Proceedings of the Fourth Compton Symposium*, 1997.

[22] V. Gerrish and L. van den Berg. "Improved yield of high resolution mercuric iodide gamma-ray spectrometers". *NIM*, A299:41, 1990.

[23] P.J. Groot, T.J. Galama, J. van Paradijs, R. Strom, J. Telting, R.G.M. Rutten, M. Pettini, N. Tanvir, R. Naber, C. Kouveliotou, J. in't Zand, J. Heise, E. Costa, M. Feroci, L. Piro, F. Frontera, G. Zavattini, L. Nicastro, and E. Palazzi. "GRB 970228". *IAUC*, 6584, 1997.

[24] B.A. Harmon, M.H. Finger, B. Rubin, R. Mallozzi, W.S. Paciesas, R.B. Wilson, G.J. Fishman, M. Brock, and C.A. Meegan. "Occultation Analysis of BATSE

data: Operational aspects". In *The Compton Observatory Science Workshop p69*, 1992.

[25] S. Hayakawa. *"Cosmic Ray Physics"*. Wiley-Interscience New York, 1969.

[26] M. Hernanz, J. Gomez-Gomar, J. Jose, and A. Coc. "Prospects for Detectability of Classical Novae with INTEGRAL". In *The 4th INTEGRAL Workshop, Exploring the gamma-ray universe*, 2000.

[27] M. Hernanz, J. Jose, A. Coc, J. Gomez-Gomar, and J. Isern. "Gamma-Ray Emission from Novae Related to Positron Annihilation: Constraints on its Observability Posed by New Experimental Nuclear Data". *ApJ*, 526:L97, 1999.

[28] M. Hernanz, D.M. Smith, J. Fishman, A. Harmon, J. Gomez-Gomar, J. Jose, J. Isern, and P. Jean. "BATSE Observations of classical novae". In *The Proceedings of the Fifth Compton Symposium, 1999, New Hampshire*, 2000.

[29] W.L. Imhof, G.H. Nakano, and J.B. Reagan. "High resolution measurements of atmospheric gamma rays from a satellite". *J. Geophys. Res.*, 81:2835, 1976.

[30] J.S. Iwanczyk. "Advances in mercuric iodide x-ray detectors and low noise preamplification systems". *NIM*, A283:208, 1989.

[31] J.S. Iwanczyk, Y.J. Wang, J.G. Bradley, J.M. Conley, A.L. Albee, and T.E. Economou. "Performance and durability of HgI_2 x-ray detectors for space missions". *IEEE Trans on Nuc. Sci.*, 36:841, 1989.

[32] W.N. Johnson, J.D. Kurfess, R.L. Kinzer, W.R. Purcell, M.S. Strickman, G.V. Jung, M.P. Ulmer, C.M. Jensen, G.H. Share, D.D. Clayton, C.S. Dyer, and R.A. Cameron. "The Oriented Scintillation Spectrometer Experiment (OSSE): Instrument Description". In *Proceedings of the First Compton Symposium*, 1989.

[33] G. Kanbach, D.L. Bertsch, A. Favale, C.E. Fichtel, R.C. Hartman, R. Hofstadter, E.B. Hughes, S.D. Hunter, B.W. Hughlock, D.A. Kniffen, Y.C. Lin, J.R. Mattox, H.A. Mayer-Hasselwander, C v.Montigny, P.L. Nolan, K. Pinkau, H. Rothermel, E. Schneid, M. Sommer, D.J. Thompson, and A.H. Walker. "The EGRET Instrument". In *Proceedings of the First Compton Symposium*, 1989.

[34] G.F. Knoll. *"Radiation Detection and Measurement"*. John Wiley & Sons, Inc, 1989.

[35] K.S. Krane. *"Introductory Nuclear Physics"*. John Wiley & Sons, Inc, 1988.

[36] W.L. Kraushaar, G.W. Clark, G.P. Garmire, R. Borken, P. Higbie, C. Leong, and T. Thorsos. "High-Energy Cosmic Gamma-Ray Observations from the OSO-3 Satellite". *ApJ*, 177:341, 1972.

[37] J. Krautter, H. Ogelman, S. Starrfield, R. Wichmann, and E. Pfeffermann. "ROSAT X-ray Observations of Nova V1974 Cygni: The Rise and Fall of the Brightest Supersoft X-ray Source". *ApJ*, 456:788, 1996.

[38] J. Kurfess, D.L. Bertsch, G.J. Fishman, and V. Schonfelder. "Overview of the Compton Observatory Instruments". In *Proceedings of the Fourth Compton Symposium*, 1997.

[39] F. Lei, C. Ferguson, A.J. Bird, J.J. Lockley, and A.J. Dean. "The INTEGRAL Mass Model - TIMM". *Astro Lett and Com*, 39:373, 1999.

[40] F. Lei, A. R. Green, A. J. Bird, C. Ferguson, and A. J. Dean. "The INTEGRAL Mass Model and Background M-C Simulations". In *Conference on the High Energy Radiation Background in Space*, pages 66+, 1999.

[41] M. D. Leising and D.D. Clayton. "Positron Annihilation Gamma Rays from Novae". *ApJ*, 323:159, 1987.

[42] M. D. Leising and G. H. Share. "The Gamma-Ray Light Curves of SN 1987A". *ApJ*, 357:638, 1990.

[43] M.D. Leising and G.H. Share. "SMM γ-Ray Observations of SN1987". In *Supernovae. The Tenth Santa Cruz Summer Workshop in Astronomy and Astrophysics, 1989*, 1990.

[44] W.R. Leo. *"Techniques for Nuclear and Particle Physics Experiments"*. Springer-Verlag, 1994.

[45] A. Loeb and E. Waxman. "Cosmic γ-ray background from structure formation in the intergalactic medium". *Nature*, 405:103, 2000.

[46] I. Malet, J.P. Roques, L. Bouchet, G. Vedrenne, J. Paul, B. Cordier, J. Ballet, F. Lebrun, R. Sunyaev, E. Churazov, M. Gilfanov, N. Khavenson, A. Dyachkov, N. Kuleshova, A. Sheikhet, and I. Tzerenin. "SIGMA Observations of the Galactic Center at 511 keV". *ApJ*, 444:222, 1995.

[47] P. Mandrou, G. Vedrenne, and M. Niel. "Diffuse cosmic gamma-ray observations from 0.3 to 6 MeV in two regions near the Galactic center and anticenter". *ApJ*, 230:97, 1979.

[48] P. Mandrou, G. Vedrenne, and M. Niel. "Diffuse Cosmic Gamma-Ray Observations from 0.3 to 6 MeV in Two Regions Near the Galactic Center and Anticenter". *ApJ.*, 230:97, 1979.

[49] M.L. McConnell, J.M. Ryan, W. Collmar, V. Schonfelder, H. Steinle, A.W. Strong, H. Bloemen, W. Hermsen, L. Kuiper, K. ennett, B.F. Philips, and J.C. Ling. "A High Sensitivity Measurement of the MeV Gamma-Ray Spectrum of Cygnus X-1". *ApJ*, 543:928, 2000.

[50] C. Meegan, K. Hurley, A. Connors, B. Dingus, and S. Matz. "A review of Gamma Ray Bursts". In *Proceedings of the Fourth Compton Symposium*, 1997.

[51] R. Mukherjee and J. Chiang. "EGRET γ-ray blazars: luminosity function and contribution to the extragalactic γ-ray background". *Astropart. Phys.*, 11:213, 1999.

[52] University of Valencia. "Private Communication". In *The Low Energy Gamma Ray Imager onboard Minisat-01*, 1998.

[53] C.L. Perfect, C. Ferguson, A. J. Bird, F. Lei, J.J. Lockley, and A.J. Dean. "Modelling the effects of a solar flare on INTEGRAL". In *Proceedings of The Fifth Compton Symposium*, 2000.

[54] D. Prialnik. "the evolution of a classical nova model through a complete cycle". *ApJ*, 310:222, 1986.

[55] A.C. Rester, R.L. Coldwell, J.I. Trombka, R. Starr, and G. Eichhorn. "Performance of bismuth germanate active shielding on a balloon flight over Antarctica". In *The Nucl. Sci. Symposium, San Francisco 1990*, volume 37, 1990.

[56] J.A. Ruiz, J.L Ferrero, G. Bernabeu, V. Reglero, and F. Sanchez. "a 3×3 csi(tl) array as an example of a segmented detector". *ApJ Sup Ser*, 92:659, 1994.

[57] J.M. Ryan. "COMPTEL:, The Imaging Compton Telescope on the Gamma Ray Observatory". In *Proceedings of the First Compton Symposium*, 1989.

[58] T.R. Sanderson and R.G. Marsden et al. "Ulysses Particle Observations of the March 1991 Solar Flare Events". *Geophys. Res. Let.*, 19:1263, 1992.

[59] E.J. Schmahl and B.R. Dennis. "Simulations of hard x-ray imaging spectroscopy with the hessi rotating modulation collimators". *AAS*, 29:02.14, 1997.

[60] V. Schönfelder, F. Graml, and F.-P. Penningsfeld. "The Vertical Component of 1-20 MeV Gamma Rays at Balloon Altitudes". *ApJ*, 240:350, 1980.

[61] V. Schönfelder, U. Graser, and J. Daugherty. "Diffuse Cosmic and Atmospheric MeV Gamma Radiation From Balloon Observations". *ApJ*, 217:306, 1977.

[62] D.A. Schwartz. "The Isotropy of the Diffuse Cosmic X-rays Determined by OSO-III". *ApJ.*, 162:439, 1970.

[63] M. M. Shara. "recent progress in understanding the eruptions of classical novae". *PASP*, 101:5, 1989.

[64] C.R. Shrader and N. Gehrels. "Recent Results from the Compton Gamma Ray Observatory". *PASP*, 107:606, 1995.

[65] G.K. Skinner, A.P. Willmore, C.J. Eyles, D. Bertram, and M.J. Church. "Hard x-ray images of the Galactic Centre". *Nature*, 330:544, 1987.

[66] R.K. Smither, P.B. Fernandez, T. Graber, P. von Ballmoos, J.E. Naya, F. Albernhe, G. Vedrenne, and F. Mohammed. "Crystal diffraction lens telescope for focusing nuclear gamma rays". *SPIE*, 2806:509, 1996.

[67] N. Soker. "A model for the outer rings of SN 1987A". *MNRAS*, 303:611, 1999.

[68] L. van den Berg. "Recent developments in mercuric iodide technology at EG & G Energy Measurements, Inc., Santa Barbara Operations". *NIM*, A322:453, 1992.

[69] J. van Paradijs, C. Kouveliotou, and R.A.M.J. Wijers. "Gamma-Ray Burst Afterglows". *ARA&A*, 38:379, 2000.

[70] B. Warner. *"Cataclysmic Variable Stars"*. Cambridge University Press, 1995.

[71] K. Watanabe, D.H. Hartmann, M.D. Leising, L.-S. The, G.H. Share, and R.L. Kinzer. "The Cosmic γ-Ray Background from Supernovae". In *Proceedings of The Fourth Compton Symposium*, 1997.

[72] W. R. Webber and J.A. Lezniak. "The comparative spectra of cosmic ray protons and helium nuclei". *Ap. Space Sci.*, 30:361, 1974.

[73] G. Weidenspointner, M. Varendorff, S.C. Kappadath, K. Bennett, H. Bloemen, R. Diehl, W. Hermsen, G.G. Lichti, J. Ryan, and V. Sch önfelder. "The cosmic diffuse gamma-ray background measured with COMPTEL". In *Proceedings of the Fifth Compton Symposium*, 2000.

[74] M.J. Westmore. "Sensitivity of BATSE analysis of a sub-sample of the Piccinotti sample". In *Private Communication*, 2000.

[75] R.C. Whited and M.M. Schieber. "Cadmium telluride and mercuric iodide gamma radiation detectors". *NIM*, 162:113, 1979.

[76] M. V. Zombeck. *"Handbook of Space Astronomy and Astrophysics"*. Cambridge University Press, 1990.